UC Berkeley
UC Berkeley Electronic Theses and Dissertations

Title
High-Redshift Type Ia Supernova Rates in Galaxy Cluster and Field Environments

Permalink
https://escholarship.org/uc/item/4d75m2cr

Author
Barbary, Kyle Harris

Publication Date
2011

Peer reviewed|Thesis/dissertation

High-Redshift Type Ia Supernova Rates in Galaxy Cluster and Field Environments

by

Kyle Harris Barbary

A dissertation submitted in partial satisfaction of the

requirements for the degree of

Doctor of Philosophy

in

Physics

in the

Graduate Division

of the

University of California, Berkeley

Committee in charge:

Professor Saul Perlmutter, Chair
Professor William Holzapfel
Professor Joshua Bloom

Spring 2011

High-Redshift Type Ia Supernova Rates in Galaxy Cluster and Field Environments

Abstract

High-Redshift Type Ia Supernova Rates in Galaxy Cluster and Field Environments

by

Kyle Harris Barbary

Doctor of Philosophy in Physics

University of California, Berkeley

Professor Saul Perlmutter, Chair

This thesis presents Type Ia supernova (SN Ia) rates from the *Hubble Space Telescope (HST)* Cluster Supernova Survey, a program designed to efficiently detect and observe high-redshift supernovae by targeting massive galaxy clusters at redshifts $0.9 < z < 1.46$. Among other uses, measurements of the rate at which SNe Ia occur can be used to help constrain the SN Ia "progenitor scenario." The progenitor scenario, the process that leads to a SN Ia, is a particularly poorly understood aspect of these events. Fortunately, the progenitor is directly linked to the delay time between star formation and supernova explosion. Supernova rates can be used to measure the distribution of these delay times and thus yield information about the elusive progenitors.

Galaxy clusters, with their simpler star formation histories, offer an ideal environment for measuring the delay time distribution. In this thesis the SN Ia rate in clusters is calculated based on 8 ± 1 cluster SNe Ia discovered in the *HST* Cluster Supernova Survey. This is the first cluster SN Ia rate measurement with detected $z > 0.9$ SNe. The SN Ia rate is found to be $0.50^{+0.23}_{-0.19}$ (stat) $^{+0.10}_{-0.09}$ (sys) h^2_{70} SNuB (SNuB $\equiv 10^{-12}$ SNe $L^{-1}_{\odot,B}$ yr^{-1}), or in units of stellar mass, $0.36^{+0.16}_{-0.13}$ (stat) $^{+0.07}_{-0.06}$ (sys) h^2_{70} SNuM (SNuM $\equiv 10^{-12}$ SNe $M^{-1}_\odot$ yr^{-1}). This represents a factor of $\approx 5 \pm 2$ increase over measurements of the cluster rate at $z < 0.2$ and is the first significant detection of a changing cluster SN Ia rate with redshift. Parameterizing the late-time SN Ia delay time distribution with a power law ($\Psi(t) \propto t^s$), this measurement in combination with lower-redshift cluster SN Ia rates constrains $s = -1.41^{+0.47}_{-0.40}$, under the approximation of a single-burst cluster formation redshift of $z_f = 3$. This is generally consistent with expectations for the "double degenerate" progenitor scenario and inconsistent with some models for the "single degenerate" progenitor scenario predicting a steeper delay time distribution at large delay times. To check for environmental dependence and the influence of younger stellar populations the rate is also calculated specifically in cluster red-sequence galaxies and in morphologically early-type galaxies, with results similar to the full cluster rate. Finally, the upper limit of one host-less cluster SN Ia detected in the survey implies that the fraction of stars in the intra-cluster medium is less than 0.47 (95% confidence), consistent with measurements at lower redshifts.

The volumetric SN Ia rate can also be used to constrain the SN Ia delay time distribution. However, there have been discrepancies in recent analyses of both the high-redshift

rate and its implications for the delay time distribution. Here, the volumetric SN Ia rate out to $z \sim 1.6$ is measured, based on ~ 12 SNe Ia in the foregrounds and backgrounds of the clusters targeted in the survey. The rate is measured in four broad redshift bins. The results are consistent with previous measurements at $z \gtrsim 1$ and strengthen the case for a SN Ia rate that is $\gtrsim 0.6 \times 10^{-4} h_{70}^3$ yr^{-1} Mpc^{-3} at $z \sim 1$ and flattening out at higher redshift. Assumptions about host-galaxy dust extinction used in different high-redshift rate measurements are examined. Different assumptions may account for some of the difference in published results for the $z \sim 1$ rate.

To,

Mom and Dad,

for always supporting me
in whatever I wanted to do,
even if it was going to grad school.

Acknowledgments

When I think back to starting with the Supernova Cosmology Project nearly six years ago, it was partially the project that convinced me to join the group but mostly it was the enthusiasm of **Saul Perlmutter**. Throughout this work his unflagging determination has been a source of inspiration. I have been thankful for the opportunity and freedom to work on the areas of analysis I found most interesting while still having Saul's guidance whenever I needed it. In writing and presenting, Saul's comments have been particularly insightful and (hopefully) have shaped the way I communicate scientifically. I won't soon forget the long nights on the phone working on *HST* proposals!

I have **Kyle Dawson** to thank for recruiting me to join the group and for being a second advisor throughout my time here. It was also Kyle who urged me to write up the peculiar transient SN SCP06F6 which ended up not only being an important result from our survey but also gave me the opportunity to gain experience talking to the media.

Of course this work has been done as part of a larger project and would have been impossible without the work and expertise of many fellow group members. I can't list everything that people have done, but I am indebted to **David Rubin** for being with me from the beginning of the supernova search, to **Natalia Connolly** for all her help on software when I was starting out, to **Nao Suzuki** for his late nights reducing ACS images, to **Joshua Meyers** for all his host galaxy analysis and for introducing me to Python for astronomy, to **Xiaosheng Huang** for his expertise in lensing, and to **Hannah Fakhouri** for careful feedback on all my work. Among other things, I am grateful to **Rahman Amanullah** for his computing expertise, "life advice" and, most of all, for how he brought the LBL SCP group together during his time in Berkeley. I don't know exactly how he does it, but **Chris Lidman**'s tireless work on many aspects of the survey bears special mention, as does **Greg Aldering**'s observing expertise and detailed input on the analyses presented here. Special thanks go to **Tony Spadafora** for so many little things and for always being there to provide a perspective.

Finally, **Lauren Tompkins** has been by my side throughout my graduate career, even when she was in a different country. Though I sometimes like to pretend otherwise, her passion for physics has always been inspiring. And of course, the biggest thanks go to my family for their constant support throughout my 24 years of schooling.

Preface

Cosmology has come a long way in the last two decades. At the beginning of the 1990s there were large uncertainties regarding the age of the universe, whether it is flat or curved, and even the nature of its major components. Today, we have overwhelming confidence that we live in a flat, accelerating universe dominated by dark energy and we have moved on to measuring its parameters with percent-level accuracy.

Much of this advance has been thanks to Type Ia supernovae (SNe Ia), a type of stellar explosion that always has (more or less) the same intrinsic brightness. A painstakingly acquired handful of these supernovae was used to determine that the universe is accelerating. Cosmologists have now become experts at finding them and using them as distance indicators at the largest scales. The current world sample of well observed supernovae has surpassed one thousand, spanning from those in the local universe out to supernovae that exploded over 9 billion years ago.

In spite of these advances, there is still much we don't know about how these explosions occur. As the field pushes forward, a more complete understanding of supernovae is becoming more and more important for measuring cosmological parameters with the accuracy needed to distinguish between models for dark energy. The work in this thesis is a small step towards a better understanding of Type Ia supernovae, via a measurement of the rate at which they occur.

This work is based on a survey carried out by the Supernova Cosmology Project (SCP) using the *Hubble Space Telescope (HST)* during 2005 and 2006, called the *HST* Cluster Supernova Survey. The main aim of the survey was to improve both the efficiency and usefulness of high-redshift SN observations with *HST* by specifically targeting high-redshift galaxy clusters. Final results from the survey are now coming to fruition, with a total of ten publications related to the supernova work and ten more (as of this writing) related to the cluster studies. This thesis represents my analyses of the data from the survey. These analyses have also been presented in Barbary et al. (2009, 2011), and will also be the subject of a third article, in preparation.

This thesis begins in Chapter 1 with a review of SN Ia progenitor models and work that has been done to differentiate between them using SN Ia rates. Chapter 2 describes the *HST* Cluster Supernova Survey, placing particular emphasis on the aspects relevant to the rate calculation. During the survey we discovered a very unusual transient. This was the subject of **Barbary et al. (2009)** and is discussed here in Chapter 3. Chapter 4 lays

out the systematic selection of supernova candidates used in the rate calculations and the determination of supernova type for these candidates (**first part of Barbary et al. 2011**). In Chapter 5 the cluster SN Ia rate is calculated based on the candidates in the clusters and, using this rate, the SN Ia delay time distribution is calculated (**second part of Barbary et al. 2011**). This is followed by a calculation of the volumetric field rate based on the non-cluster-member candidates in Chapter 6 (**Barbary et al., in preparation**). Finally, the thesis work is summarized in Chapter 7.

Contents

List of Figures

List of Tables

CHAPTER 1

Introduction: Type Ia Supernovae and Their Progenitors

1.1   Type Ia Supernovae as Standard Candles

Supernovae (SNe) are the explosion of stars at the end of their lives that can be as bright as ten billion Suns for a period of a few weeks. They are divided into subtypes empirically, based on the properties of their optical spectra. The first division, into Types I and II, was firmly established by Minkowski (1941). Supernovae whose spectra clearly exhibit hydrogen are Type II; those that do not are Type I. These two main classes have since been subdivided. Specifically for Type I, it was recognized that there are spectroscopically distinguishable subsets in the mid-1980s (Elias et al. 1985; Panagia 1985; Wheeler & Levreault 1985; Uomoto & Kirshner 1985). Type I SNe are now divided into Ia, Ib and Ic. Type Ia SNe (SNe Ia) are defined by the presence of a strong Si II $\lambda6355$ absorption trough blueshifted to ~ 6100Å while Types Ib and Ic do not have this feature and are divided by the presence (Ib) or absence (Ic) of clear helium I lines (see Filippenko 1997, for a review).

Since the original division into Types I and II a more physical dichotomy has become apparent: SNe Ia are now widely accepted to be thermonuclear disruptions of mass-accreting carbon-oxygen (C-O) white dwarfs (WDs), while all other types are thought to result from the core collapse of massive stars ($> 8M_\odot$) at the end of their lives. For SNe Ia, the explosion is believed to occur as the white dwarf nears the Chandrasekhar (1931) mass limit. That all SNe Ia occur at nearly the same mass gives a natural explanation for the overwhelming homogeneity exhibited by this (but not any other) type.

This homogeneity is what makes SNe Ia the best available "standard candles" that are visible at cosmological distances. Their peak absolute B-band magnitudes have a dispersion of $\sigma(M_B) \sim 0.3$ (e.g., Hamuy et al. 1996), excluding spectroscopically peculiar SNe Ia. Empirical correlations between absolute magnitude and other SN properties can be used to effectively decrease this dispersion, increasing their utility for cosmological measurements. The first and most widely used such correlation is between the absolute magnitude and the width of the SN light curve (or rate of decline): brighter SNe have light

curves that are wider, or slower evolving. Characterizing the light curve width with the Δm_{15} (Phillips 1993) or "stretch" (s; Perlmutter et al. 1997) parameter, the dispersion of "corrected" peak magnitudes can be reduced to $\sigma(M_B^{\text{corr}}) \sim 0.17$.

Today there are various methods used to parameterize SN Ia light curves and determine corrected magnitudes (e.g., Guy et al. 2005, 2007; Jha et al. 2007; Conley et al. 2008). In addition to light curve shape, a second parameter corresponding to the SN color is used. For example, the SALT light curve fitter (Guy et al. 2005) defines the corrected magnitudes as

$$M_B^{\text{corr}} = M_B + \alpha(s - 1) - \beta c \qquad (1.1)$$

where c is the SN color, approximately equivalent to $E(B - V)$. With two parameters the dispersion can be reduced to $\lesssim 0.15$ mag and there is evidence that it can be reduced to 0.13 mag or lower with other correlations, such as with spectral line ratios (Bailey et al. 2009).

In contrast to the handful of SNe Ia used in the discovery of dark energy over a decade ago (Perlmutter et al. 1997; Riess et al. 1998; Perlmutter et al. 1999), over 500 SNe Ia are now used in the latest analyses (e.g. Hicken et al. 2009; Amanullah et al. 2010), with at least as many more observed and still "in the pipeline." Combined with constraints from baryon acoustic oscillations and the cosmic microwave background, SNe Ia constrain $\Omega_M = 0.277 \pm 0.014$ (stat) $^{+0.017}_{-0.016}$ (stat+sys) and $w = -1.009^{+0.050}_{-0.054}$(stat) $^{+0.077}_{-0.082}$ (stat+sys), assuming a flat universe (Amanullah et al. 2010).

1.2 The Progenitors of SNe Ia

Despite their very successful use as standard candles and the vast numbers of them now observed, *significant* uncertainties remain about many aspects of SNe Ia. As noted above, we are quite certain about the basic model of SNe Ia: they are the thermonuclear explosion of mass-accreting C-O WDs, and that furthermore the accreted mass is donated by a binary companion star. However, the nature of the companion star, how the system evolves to trigger a SN Ia, and how the explosion starts and progresses are still unknown (see Livio 2001, for a review).

The nature of the companion and the evolution of the system prior to explosion are collectively referred to as the progenitor scenario. In addition to the intrinsic interest in the SNe themselves, a better understanding of the progenitor scenario is demanded from both a cosmological and an astrophysical perspective. Cosmologically, the corrections that improve the standardization of SNe Ia are entirely based on *empirical* relations, and not a deep understanding of the events themselves. While the unknown nature of the SN progenitor system is unlikely to bias measurements at the current level of uncertainty (Yungelson & Livio 2000; Sarkar et al. 2008), it could become a significant source of uncertainty in the future as statistical uncertainty continues to decrease. Essentially, it leaves open the question of whether high-redshift SNe are different than low-redshift SNe in a way that affects

the inferred distance. Astrophysically, SNe Ia dominate the production of iron (e.g., Matteucci & Greggio 1986; Tsujimoto et al. 1995; Thielemann et al. 1996) and provide energy feedback (Scannapieco et al. 2006) in galaxies. To properly include these effects in galaxy evolution models requires an accurate prediction of the SN Ia rate in galaxies of varying ages, masses and star formation histories, which in turn requires a good understanding of the progenitor. This is particularly true for higher redshifts where direct SN rate constraints are unavailable.

1.2.1 Models

The leading models fall into two classes: the *single degenerate* scenario (SD; Whelan & Iben 1973; Nomoto 1982), and the *double degenerate* scenario (DD; Iben & Tutukov 1984; Webbink 1984). In the SD scenario the companion is a red giant or main sequence star that overflows its Roche lobe. In the DD scenario, the companion is a second C-O WD which merges with the primary after orbital decay due to the emission of gravitational radiation. Within the SD class of models there are various refinements: The companion could be a red giant donating hydrogen or a subgiant donating helium rich material, or even a main sequence star in close orbit. The explosion could occur very near the Chandrasekhar mass or significantly below it. Among DD models there is less room for refinement as both stars are necessarily WDs. However, their total mass and their mass ratios are open questions. For example, van Kerkwijk et al. (2010) have recently suggested sub-Chandrasekhar mass systems with WDs of roughly equal mass as a promising progenitor candidate.

It is possible to probe the progenitor scenario via direct observations, such as imaging of SN remnants (e.g., Ruiz-Lapuente et al. 2004; Ihara et al. 2007; Maoz & Mannucci 2008; González Hernández et al. 2009), the observation of hydrogen in SN spectra (e.g., Livio & Riess 2003), X-ray detection before explosion (e.g., Nelemans et al. 2008; Roelofs et al. 2008; Gilfanov & Bogdán 2010), or searches for likely progenitor systems (e.g., Geier et al. 2007; Parthasarathy et al. 2007). Drawing definitive conclusions based on such observations is typically quite difficult, due in part to the rarity of very nearby SNe Ia, and in part to the fact that even the direct detection of one type of progenitor scenario cannot rule out a contribution from the other scenario.

Along these lines, note that recently the observation of SNe Ia with super-Chandrasekhar mass progenitors (Howell et al. 2006; Scalzo et al. 2010) has been taken as evidence in favor of the DD scenario. However, there is some confusion about how this can be achieved in the DD scenario, as the lighter WD is expected to dissipate into a disk in the merger process. Even if these SNe are found to originate from DD progenitors, they represent only a small subset of all SNe Ia; the bulk of SNe may be explained by a different mechanism.

1.3   SN Ia Rates and the Delay Time Distribution

An alternative to direct detection is to probe the progenitor scenario statistically by measuring the rate at which SNe Ia occur (e.g., Ruiz-Lapuente et al. 1995; Ruiz-Lapuente & Canal 1998; Yungelson & Livio 2000). SN Ia rates constrain the progenitor scenario via the delay time distribution (DTD), $\Psi(t)$, where "delay time" refers to the time between star formation and SN Ia explosion. The DTD is the distribution of these times for a population of stars, and is equivalent to the SN Ia rate as a function of time after a burst of star formation. Crucially, the delay time is governed by different physical mechanisms in the different progenitor scenarios. For example, in the DD scenario, the delay time is dominated by the time the orbit takes to decay due to gravitational radiation. In the SD scenario, when the donor is a red giant star the delay time is set by the time the companion takes to evolve off the main sequence.

To see how these dependencies translate to different DTDs for a population of stars, we consider a simplified model for each scenario. For the DD scenario, we make the approximation that the time to form a double WD binary is negligible compared to the gravitational radiation merger time. That time depends on the the initial WD separation (a) as

$$t \propto a^4. \tag{1.2}$$

Assuming the initial separations are distributed as a power law,

$$\frac{dN}{da} \propto a^\epsilon, \tag{1.3}$$

the SN rate as a function of time (DTD) is given by

$$\Psi(t) = \frac{dN}{dt} = \frac{dN}{da}\frac{da}{dt} \propto t^{(\epsilon-3)/4} \quad \text{(DD scenario)}. \tag{1.4}$$

For the SD scenario with a red giant companion star, we similarly neglect the time to form the WD and assume that the delay time is equal to the main-sequence lifetime of the secondary (lower mass) star. If that lifetime depends on the mass as a power law,

$$t \propto m^\delta, \tag{1.5}$$

and if we assume the initial mass function (IMF) follows a power law as well,

$$\frac{dN}{dm} \propto m^\lambda, \tag{1.6}$$

then the DTD is given by

$$\Psi(t) = \frac{dN}{dm}\frac{dm}{dt} \propto t^{(1+\lambda-\delta)/\delta} \quad \text{(SD scenario)}. \tag{1.7}$$

Plugging in nominal values of $\epsilon = -1$ for the DD scenario (the approximate separation distribution observed in binary systems) and the commonly used value $\delta = -2.5$ and the

Salpeter (1955) slope $\lambda = -2.35$ for the SD scenario, we arrive at $\Psi(t) \propto t^{-1}$ for the DD scenario and $\Psi(t) \propto t^{-0.46}$ for the SD scenario.

These models serve to illustrate how the shape of the DTD can be affected by the progenitor, but in both cases these are oversimplifications. In the DD model, although the distribution of initial binary separations is observed to be approximately $\propto a^{-1}$, the distribution of separations after the system has passed through two common envelope (CE; see, e.g., Yungelson 2005) phases is not known. It is could be radically different, resulting in a power law much different than $\Psi(t) \propto t^{-1}$. Furthermore, at small delay times, the DTD will not follow a power law at all, as WDs do not form instantaneously, but take from $40 - 400$ Myr after star formation. In the SD scenario, the slope of the DTD can actually be much steeper than $\sim t^{-0.5}$ at later times. This is because in an older population, fewer and fewer secondary stars will have the required envelope mass to to donate to the primary so that it can reach $1.4 M_\odot$. In addition, factors such as the IMF, the distribution of initial separation and mass ratio in binary systems, are not perfectly known and will affect the derived DTD.

Detailed delay time distributions attempting to take these and other effects into account were computed analytically following the proposal of both the SD (Greggio & Renzini 1983) and DD (Tornambe & Matteucci 1986; Tornambe 1989) scenarios. Later, theoretical DTDs were extended to include various subclasses of each model and a wider range of parameters (Tutukov & Yungelson 1994; Yungelson & Livio 2000; Matteucci & Recchi 2001; Belczynski et al. 2005; Greggio 2005). More recently, binary population synthesis codes have been used to compute the DTD numerically, following a population of binaries with chosen initial conditions through the stages of stellar and binary evolution. In recent such studies, different plausible prescriptions for the initial conditions and for the binary evolution have lead to widely ranging DTDs, even within one scenario (Hachisu et al. 2008; Kobayashi & Nomoto 2009; Ruiter et al. 2009; Mennekens et al. 2010). Figure 1.1 shows an example of various DTDs from Mennekens et al. (2010). A measurement of the DTD then must constrain not only the relative contribution of various progenitor scenarios, but also the initial conditions and CE phase, which is particularly poorly constrained. Still, most simulations show a difference in the DTD shape between the SD and DD scenarios: the SD scenario typically shows a strong drop-off in the SN rate at large delay times, whereas this is not seen in the DD scenario (but see Hachisu et al. 2008).

1.4   Constraints from SN Ia Rates

As the DTD is simply the SN Ia rate as a function of time after star formation, it can be measured empirically by measuring the SN rate in stellar populations of many different ages. In practice, this is difficult because the typical galaxy is made up of many stars of different ages. When a SN Ia explodes, it is usually impossible to tell which particular population the SN came from.

Five years ago, we had very little information about the shape of the DTD from an
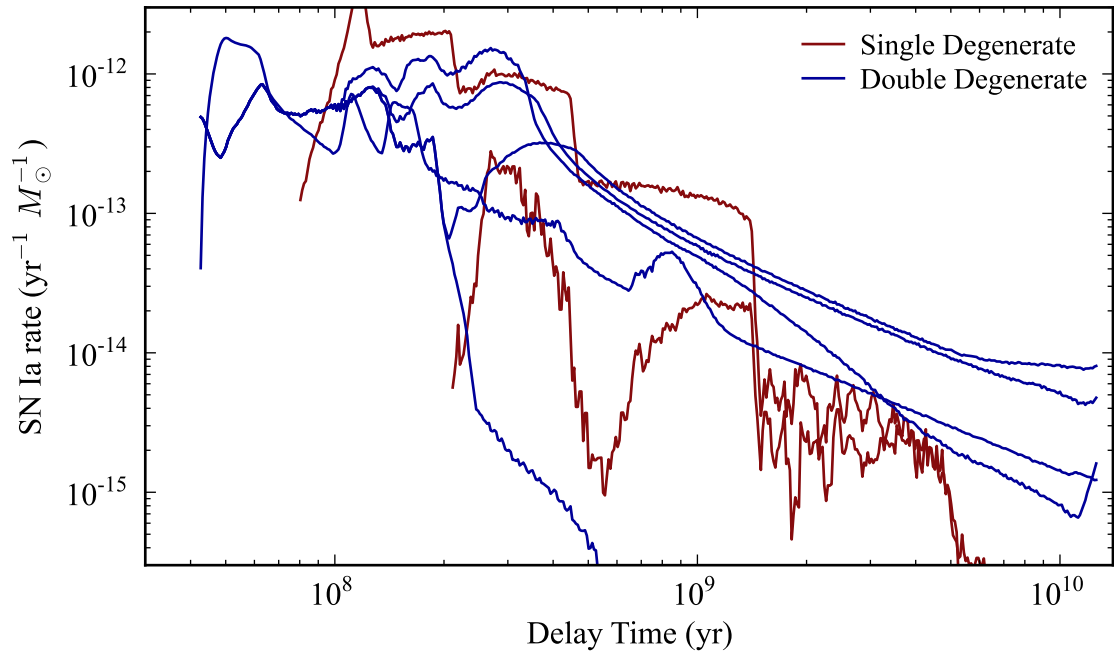
Figure 1.1. An example of delay time distributions calculated using stellar population synthesis models from Mennekens et al. (2010). The various single degenerate and double degenerate DTDs use different assumptions and prescriptions for common envelope evolution.

observational standpoint. It had been recognized much earlier that the SN Ia rate is higher in star-forming galaxies (van den Bergh 1990), implying that the DTD is largest at small delay times. [In fact, even earlier this trend was suggested as a motivation for two distinct subsets of SNe I by Dallaporta (1973).] However, little detail was gained over the next 15 years. Some recent measurements have confirmed the same trend with larger samples (Mannucci et al. 2005). This has lead to a parameterization of the DTD with a "two component" model (Scannapieco & Bildsten 2005) in which one component is proportional to the instantaneous star formation rate and the other component is proportional to stellar mass:

$$\mathcal{R}_{\text{SN Ia}}(t) = AM_\star(t) + B\dot{M}_\star(t). \tag{1.8}$$

Also known as the "$A + B$" model, this form is convenient for predicting the SN rate in environments with varying amounts of recent star formation, and its parameters can be measured with relative ease (e.g., Sullivan et al. 2006). However, it suffers from being unphysical (the B component implies a delay time of zero) and lacking theoretical motivation. Unfortunately, this simplified model was often interpreted as evidence for two distinct populations of progenitors (e.g., Mannucci et al. 2006), even though a single progenitor channel could easily reproduce the observed data. Complicating the entire situation at the time, some measurements produced results in contradiction with the existence of short delay-time SNe Ia. For example, Dahlen et al. (2004) found the volumetric SN Ia rate

(discussed in greater detail below) to decrease at $z \gtrsim 1$, implying a narrow DTD centered at $t \sim 3$ Gyr, with no contribution from short-delay SNe (Strolger et al. 2004).

Recently, more detailed measurements of the DTD have become possible using a variety of methods. Several measurements have confirmed that the delay time spans a wide range, from less than 100 Myr (e.g., Aubourg et al. 2008) to many Gyr (e.g., Schawinski 2009). Detailed spectroscopic host galaxy information for a large SN sample has allowed better constraints on stellar population ages (Brandt et al. 2010). The DTD at intermediate delay times has been accessed using early-type galaxies (Totani et al. 2008). The common wisdom arising from these measurements is that the SN rate generally declines with time, and that SNe with progenitor ages $\lesssim$ a few hundred Myr comprise perhaps $\sim$50% of all SNe Ia.

We now discuss two particular approaches to DTD measurements that are the main subject of this thesis: volumetric rates and rates specifically in galaxy clusters.

1.4.1   The Volumetric Field Rate

One particular method for measuring the DTD is to correlate the cosmic star formation history (SFH) with the the cosmic SN Ia rate as a function of redshift (Yungelson & Livio 2000): the rate as a function of cosmic time is simply the cosmic SFH convolved with the DTD. Knowing the SFH to good accuracy and measuring the SN Ia rate, one can work out the DTD.

A decade ago, before this method had ever been implemented, it was not always looked upon as having great promise. Mario Livio, for one, took this view in his review of SN Ia progenitors:

> The progenitors can be identified from the observed frequency of SNe Ia as a function of redshift, since different progenitor models produce different redshift distributions. Personally, I think it would be quite pathetic to have to resort to this possibility.

> – Mario Livio (2001)

However, in the intervening ten years, this method has gained appeal. In part, this has been because direct detection methods (such as spectroscopic detection of hydrogen in SNe Ia) have still not provided definitive answers as hoped. At the same time advances in SN rate measurements and new methods for backing out the DTD have started yielding constraints that are informing progenitor models (e.g. van Kerkwijk et al. 2010).

A measurement of the volumetric SN Ia rate is often a "free" byproduct of conducting a survey for SNe for cosmology measurements. As a result, the rate has now been measured in many different SN surveys at redshifts $0 < z < 1$ (Pain et al. 2002; Neill et al. 2007, e.g.). For some time, a number of measurements were in disagreement. However, with new precise results at low redshift (Dilday et al. 2010b; Li et al. 2011) and the recently revised

rates from the IfA Deep survey (Rodney & Tonry 2010), most measurements at $z < 1$ have now come into agreement, and paint a consistent picture of a SN rate increasing with redshift. These measurements are reaching the precision necessary for a DTD measurement: the slope of the increase at low redshift ($z \lesssim 0.3$) alone has recently been used to constrain the DTD (Horiuchi & Beacom 2010). However, due to the difficulty of detecting $z \gtrsim 1$ SNe from the ground, measurements at these higher redshifts have been limited to SN searches in the GOODS[1] fields (Dahlen et al. 2004; Kuznetsova et al. 2008; Dahlen et al. 2008) using *HST* and ultra-deep single-epoch searches in the Subaru Deep Field (SDF) from the ground (Poznanski et al. 2007b; Graur et al. 2011). These studies have yielded discrepant results for both the SN rate and the implications for the DTD. The first $z > 1$ measurements by Dahlen et al. (2004) (and later Dahlen et al. 2008, with an expanded dataset) showed a rate that peaked at $z \sim 1$ and decreased in the highest redshift bin at $z > 1.4$. However, an independent analysis of much of the same dataset by Kuznetsova et al. (2008) resulted in a substantially lower rate at $z \sim 1$ and an inability to distinguish a falling rate at high redshift. The recent results of Graur et al. (2011) from the SDF also show a substantially lower rate at $z \sim 1$, at the level of $\sim 2\sigma$ (statistical-only) in each of two bins compared to Dahlen et al. (2004). Their results are consistent with a flat SN rate at $z \gtrsim 1$, and were used to infer a DTD proportional to a power law in time with index of approximately -1.

Relative to the *HST* measurements, the SDF measurements have the advantage of better statistics in the highest-redshift bin, but *HST* measurements hold advantages in systematics. A rolling search with *HST* offers multiple observations of each SN and much higher resolution than possible from the ground, useful for resolving separation between SNe and their hosts. These factors lead to a more robust identification of SNe Ia relative to the SDF searches where a single observation is used for both detection and photometric typing. In addition, the Dahlen et al. (2008) analysis used spectroscopic typing in addition to photometric typing, whereas Graur et al. (2011) uses only photometric typing. In general, the very different strategies employed make *HST* measurements a good cross-check for the SDF measurements and vice versa. Increasing the statistics in *HST* rate measurements can help in resolving the source of the discrepancies between the two measurements. At the same time, it is important to carefully consider the assumptions about SN properties that have gone into each measurement. Illustrating this importance is the significant difference between the results of Kuznetsova et al. (2008) and Dahlen et al. (2008) despite a largely overlapping dataset.

In chapter 6 of this thesis, we address these issues by (1) supplementing current determinations of the *HST*-based $z \gtrsim 1$ SN Ia rate and (2) comparing the effect on results of different dust distributions assumed in previous analyses.

---

[1]Great Observatories Origins Deep Survey (Giavalisco et al. 2004)

1.4.2 Cluster Rates

As an alternative to volumetric SN Ia rates where stellar populations with a wide range of ages contribute at all redshifts, it is more straightforward to extract the DTD in stellar populations with a narrow range of ages (with a single burst of star formation being the ideal). Galaxy clusters, which are dominated by early-type galaxies, provide an ideal environment for constraining the shape of the DTD at large delay times. Early-type galaxies are generally expected to have formed early ($z \gtrsim 2$) with little star formation since (Stanford et al. 1998; van Dokkum et al. 2001). Cluster early-type galaxies in particular form even earlier than those in the field, with most star formation occurring at $z \gtrsim 3$ (Thomas et al. 2005; Sánchez-Blázquez et al. 2006; Gobat et al. 2008). Measuring the cluster SN Ia rate over a range of redshifts from $z = 0$ to $z > 1$ provides a measurement of the SN Ia rate at delay times from ~ 2 to 11 Gyr. Obtaining an accurate rate at the highest-possible redshift is crucial for constraining the shape of the late-time DTD: a larger redshift range corresponds to a larger lever arm in delay time.

In addition to DTD constraints, there are also strong motivations for measuring the cluster SN Ia rate from a perspective of cluster studies. SNe Ia are an important source of iron in the intracluster medium (e.g., Loewenstein 2006). Cluster SN rates constrain the iron contribution from SNe and, paired with measured iron abundances, can also constrain possible enrichment mechanisms (Maoz & Gal-Yam 2004). The high-redshift cluster rate is particularly important: measurements show that most of the intracluster iron was produced at high redshift (Calura et al. 2007). The poorly-constrained high-redshift cluster rate is one of the largest sources of uncertainty in constraining the metal-loss fraction from galaxies (Sivanandam et al. 2009).

Cluster SNe Ia can also be used to trace the diffuse *intracluster* stellar component. Intracluster stars, bound to the cluster potential rather than individual galaxies, have been found to account for anywhere from 5% to 50% of the stellar mass in clusters (e.g., Ferguson et al. 1998; Feldmeier et al. 1998; Gonzalez et al. 2000; Feldmeier et al. 2004; Lin & Mohr 2004; Zibetti et al. 2005; Gonzalez et al. 2005; Krick et al. 2006; Mihos et al. 2005). The use of SNe Ia as tracers of this component was first demonstrated by Gal-Yam et al. (2003) who found two likely host-less SNe Ia out of a total of seven cluster SNe Ia in $0.06 < z < 0.19$ Abell clusters. After correcting for the greater detection efficiency of host-less SNe, they determined that on average, the intracluster medium contained $20^{+20}_{-12}\%$ of the total cluster stellar mass. The intrinsic faintness of the light from intracluster stars, combined with $(1 + z)^4$ surface brightness dimming, makes surface brightness measurements impossible at redshifts much higher than $z = 0.3$. Type Ia supernovae, which are detectable up to and beyond $z = 1$, provide a way to measure the intracluster stellar component and its possible evolution with redshift.

The cluster SN Ia rate has recently been measured at lower redshifts ($z > 0.3$) in several studies (Sharon et al. 2007; Mannucci et al. 2008; Dilday et al. 2010a), and at intermediate redshift ($z \sim 0.6$) by Sharon et al. (2010). However, at higher redshifts ($z \gtrsim 0.8$), only weak constraints on the high-redshift cluster Ia rate exist, based on 1–2

SNe Ia at $z = 0.83$ (Gal-Yam et al. 2002). In Chapter 5 of this thesis, we calculate the SN Ia rate in $0.9 < z < 1.46$ clusters. We address the host-less SN Ia fraction, and use our result to place constraints on the late-time DTD in clusters.

1.5 Conventions Used in this Work

Throughout this thesis a cosmology with $H_0 = 70\,\mathrm{km\,s^{-1}\,Mpc^{-1}}$, $\Omega_M = 0.3$, $\Omega_\Lambda = 0.7$ is assumed. Unless otherwise noted, magnitudes are in the Vega system.

CHAPTER 2

The *HST* Cluster Supernova Survey

In a collaboration with members of the IRAC Shallow Cluster Survey (Eisenhardt et al. 2008), the Red-Sequence Cluster Survey (RCS) and RCS-2 (Gladders & Yee 2005; Yee et al. 2007), the XMM Cluster Survey (Sahlén et al. 2009), the Palomar Distant Cluster Survey (Postman et al. 1996), the XMM-Newton Distant Cluster Project (Bohringer et al. 2005), and the ROSAT Deep Cluster Survey (RDCS; Rosati et al. 1999), the SCP developed and carried out a novel supernova survey approach. We aimed to improve both the efficiency and usefulness of high-redshift SN observations with *HST* by specifically targeting high-redshift galaxy clusters. Clusters provide a significant enhancement in the density of potential SN hosts in *HST*'s relatively small field of view. Furthermore, the centers of rich clusters are dominated by relatively dust-free early-type galaxies. SNe discovered in such galaxies offer an opportunity to reduce the systematic uncertainty associated with extinction corrections. Here we summarize the survey, named the *HST* Cluster Supernova Survey (PI Perlmutter; *HST* program GO-10496) and discuss aspects most relevant to the SN rate calculation.

2.1   Cluster Targets and Survey Strategy

We used the Advanced Camera for Surveys (ACS) to search for and observe SNe in 25 of the most massive galaxy clusters available at the time of the survey. The survey was carried out during *HST* Cycle 14 with observations spanning from July 2005 to December 2006. Clusters were selected from X-ray, optical and IR surveys and cover the redshift range $0.9 < z < 1.46$. Twenty-four of the clusters have spectroscopically confirmed redshifts and the remaining cluster has a photometric redshift estimate. Cluster positions, redshifts and discovery methods are listed in Table 2.1.

During the survey, each cluster was observed once every 20 to 26 days during its *HST* visibility window (typically four to seven months). Figure 2.1 shows the dates of visits to each cluster. Each visit consisted of four exposures in the F850LP filter (hereafter z_{850}). Most visits also included a fifth exposure in the F775W filter (hereafter i_{775}). We revisited clusters D, N, P, Q, R and Z towards the end of the survey when they became visible again.

Table 2.1. Clusters targeted in survey

ID	Cluster	Redshift	R.A. (J2000)	Decl. (J2000)	Discovery
A	XMMXCS J2215.9-1738	1.45	$22^h\,15^m\,59^s.0$	$-17°\,37'\,59''$	X-ray
B	XMMU J2205.8-0159	1.12	$22^h\,05^m\,50^s.6$	$-01°\,59'\,30''$	X-ray
C	XMMU J1229.4+0151	0.98	$12^h\,29^m\,29^s.2$	$+01°\,51'\,21''$	X-ray
D	RCS J0221.6-0347	1.02	$02^h\,21^m\,42^s.2$	$-03°\,21'\,52''$	Optical
E	WARP J1415.1+3612	1.03	$14^h\,15^m\,11^s.1$	$+36°\,12'\,03''$	X-ray
F	ISCS J1432.4+3332	1.11	$14^h\,32^m\,28^s.1$	$+33°\,33'\,00''$	IR-Spitzer
G	ISCS J1429.3+3437	1.26	$14^h\,29^m\,17^s.7$	$+34°\,37'\,18''$	IR-Spitzer
H	ISCS J1434.4+3426	1.24	$14^h\,34^m\,28^s.6$	$+34°\,26'\,22''$	IR-Spitzer
I	ISCS J1432.6+3436	1.34	$14^h\,32^m\,38^s.8$	$+34°\,36'\,36''$	IR-Spitzer
J	ISCS J1434.7+3519	1.37	$14^h\,34^m\,46^s.0$	$+35°\,19'\,36''$	IR-Spitzer
K	ISCS J1438.1+3414	1.41	$14^h\,38^m\,08^s.2$	$+34°\,14'\,13''$	IR-Spitzer
L	ISCS J1433.8+3325	1.37	$14^h\,33^m\,51^s.1$	$+33°\,25'\,50''$	IR-Spitzer
M	Cl J1604+4304	0.92	$16^h\,04^m\,23^s.8$	$+43°\,04'\,37''$	Optical
N	RCS J0220.9-0333	1.03	$02^h\,20^m\,55^s.5$	$-03°\,33'\,10''$	Optical
P	RCS J0337.8-2844	1.1[a]	$03^h\,37^m\,51^s.2$	$-28°\,44'\,58''$	Optical
Q	RCS J0439.6-2904	0.95	$04^h\,39^m\,37^s.6$	$-29°\,05'\,01''$	Optical
R	XLSS J0223.0-0436	1.22	$02^h\,23^m\,03^s.4$	$-04°\,36'\,14''$	X-ray
S	RCS J2156.7-0448	1.07	$21^h\,56^m\,42^s.2$	$-04°\,48'\,04''$	Optical
T	RCS J1511.0+0903	0.97	$15^h\,11^m\,03^s.5$	$+09°\,03'\,09''$	Optical
U	RCS J2345.4-3632	1.04	$23^h\,45^m\,27^s.2$	$-36°\,32'\,49''$	Optical
V	RCS J2319.8+0038	0.91	$23^h\,19^m\,53^s.4$	$+00°\,38'\,13''$	Optical
W	RX J0848.9+4452	1.26	$08^h\,48^m\,56^s.4$	$+44°\,52'\,00''$	X-ray
X	RDCS J0910+5422	1.11	$09^h\,10^m\,45^s.1$	$+54°\,22'\,07''$	X-ray
Y	RDCS J1252.9-2927	1.23	$12^h\,52^m\,54^s.4$	$-29°\,27'\,17''$	X-ray
Z	XMMU J2235.3-2557	1.39	$22^h\,35^m\,20^s.8$	$-25°\,57'\,39''$	X-ray

[a] photometric redshift

References. — A (Stanford et al. 2006; Hilton et al. 2007); B,C (Bohringer et al. 2005; Santos et al. 2009); D (also known as RzCS 052; Andreon et al. 2008a,b); D, N, U (Gilbank et al. in prep); E (Perlman et al. 2002); F (Elston et al. 2006); G, I, J, L (Eisenhardt et al. 2008); L (Brodwin et al. in prep; Stanford et al. in prep); H (Brodwin et al. 2006); K (Stanford et al. 2005); M (Postman et al. 2001); Q (Cain et al. 2008); R (Andreon et al. 2005; Bremer et al. 2006); S (Hicks et al. 2008); V (Gilbank et al. 2008); W (Rosati et al. 1999); X (Stanford et al. 2002); Y (Rosati et al. 2004); Z (Mullis et al. 2005; Rosati et al. 2009).

Note. — Cluster positions differ slightly from those originally reported in Dawson et al. (2009) due to the use of an updated algorithm for determining cluster centers. See §5.4 for a description of this algorithm.
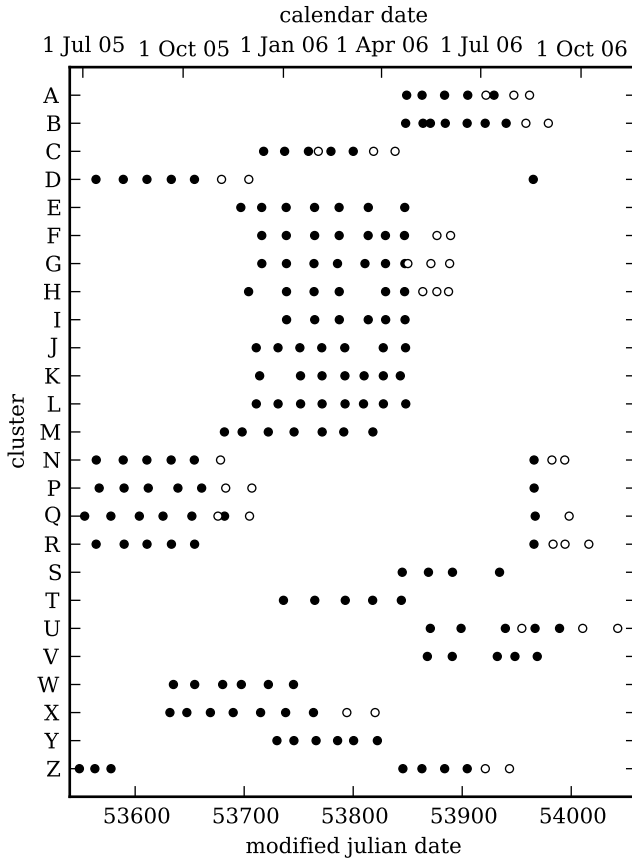
Figure 2.1. Dates of visits to each cluster. All visits included z_{850} exposures (usually four). Most visits also included one i_{775} exposure. Filled circles indicate "search" visits (used for finding SNe). Open circles indicate "follow-up" visits (contingent on the existence of an active SN candidate). Clusters D, N, P, Q and R were revisited once towards the end of the survey, with additional follow-up visits devoted to clusters in which promising SN candidates were found (N, Q, R).

Immediately following each visit, the four z_{850} exposures were cosmic ray-rejected and combined using MULTIDRIZZLE (Fruchter & Hook 2002; Koekemoer et al. 2002) and searched for supernovae. Following the technique employed in the earliest Supernova Cosmology Project searches (Perlmutter et al. 1995, 1997), we used the initial visit as a reference image, flagged candidates with software and then considered them by eye. Likely supernovae were followed up spectroscopically using pre-scheduled time on the Keck and Subaru telescopes and target-of-opportunity observations on VLT. For nearly all SN candidates, either a live SN spectrum or host galaxy spectrum was obtained. In many cases, spectroscopy of cluster galaxies was obtained contemporaneously using slit masks. Candidates deemed likely to be at higher redshift ($z > 1$) were also observed with the NICMOS camera on *HST*, but these data are not used in this work.

For the purpose of a rate calculation it is important to note that a number of visits were contingent on the existence of an active SN. At the end of a cluster's visibility window, the last two scheduled visits were cancelled if there was no live SN previously discovered. This is because a SN discovered on the rise in either of the last two visits could not be followed long enough to obtain a cosmologically useful light curve. In addition, supplementary visits between pre-scheduled visits were occasionally added to provide more complete light curve information for SNe (in the case of clusters A, C, Q, and U). We call all visits contingent

on the existence of an active SN "follow-up" visits (designated by open circles in Fig. 2.1). Search and follow-up visits are considered differently when calculating an SN rate.

2.2 Data Processing

Following the conclusion of the survey, all ACS images were reprocessed (see details in Suzuki et al. 2011). This reprocessing included an updated flat field, gain adjustment, custom sky subtraction, and updated distortion correction and zeropoints. The images for each cluster were aligned and output to a single common reference frame for the cluster using the MULTIDRIZZLE software. That is, the combined images for each epoch are all on the same image and physical reference frame for a given cluster. This makes it possible to stack and subtract images without resampling the data. The four individual exposures (not cosmic ray-rejected) are also transformed onto this output reference frame. The output pixel scale is equal to the physical pixel scale: $0''.05$.

A single sky noise for each image is calculated, for use in the rate calculation. To do this accurately, we first cut pixels with effective exposure time less than 50% of the total exposure time. We calculate a rough sky noise level, then cut pixels belonging to objects. The requirement to be an object is 1 pixel above 4σ and 5 contiguous pixels above 2.5σ. This is done iteratively until σ has converged to within 25%.

2.3 Survey Publications

The supernova-related results from the survey are reported in the following publications: Paper I (Dawson et al. 2009) describes the survey strategy and discoveries. Paper II (Barbary et al. 2011) reports on the SN Ia rate in clusters. Paper III (Meyers et al. 2011) addresses the properties of the galaxies that host SNe Ia. Paper IV (Ripoche et al. 2011) introduces a new technique to calibrate the zeropoint of the NICMOS camera at low counts rates, critical for placing NICMOS-observed SNe Ia on the Hubble diagram. Paper V (Suzuki et al. 2011) reports the SNe Ia light curves and cosmology from the program. Paper VI (Barbary et al., in preparation) reports on the volumetric field SN Ia rate. Melbourne et al. (2007), one of several unnumbered papers in the series, present a Keck adaptive optics observation of a $z = 1.31$ SN Ia in H-band. Barbary et al. (2009) report the discovery of the extraordinary luminous supernova, SN SCP06F6. Morokuma et al. (2010) presents the spectroscopic follow-up observations for SN candidates. Finally, Hsiao et al. (in preparation) develop techniques to remove problematic artifacts remaining after the standard STScI pipeline. A separate series of papers, ten to date, reports on cluster studies from the survey: Hilton et al. (2007); Eisenhardt et al. (2008); Jee et al. (2009); Hilton et al. (2009); Huang et al. (2009); Rosati et al. (2009); Santos et al. (2009); Strazzullo et al. (2010); Brodwin et al. (2011); Jee et al. (in preparation).

CHAPTER 3

The Unusual Supernova SN SCP06F6

Before we progress with the study of Type Ia SNe found in the survey, we take a detour to discuss an very interesting transient that turned out not to be a SN Ia. The transient, designated either SN SCP06F6 or SCP 06F6, was first detected in February 2006. It was originally reported in a June 2006 IAU circular (Dawson et al. 2006) while detailed data and a discussion were presented later in Barbary et al. (2009). Its light curve rise-time of ∼100 days is inconsistent with all known SN types, and its spectroscopic attributes are not readily matched to any known variable. It is surprising to discover such a rare object in a survey with *HST*, given its extremely small field of view relative to ground-based SN surveys. However, current indication are that this is indeed what happened, as a few candidates bearing some similarities have since been identified in vastly wider-area surveys.

We present photometry in §3.1 and spectroscopy in §3.2. In §3.3, we discuss constraints on possible identities.

3.1 Photometry

The transient was discovered on 21 February 2006 (UT) in a field centered on cluster CL 1432.5+3332.8 (F; $z = 1.112$). This field was imaged over nine epochs with a period of roughly three weeks. The discovery occurred in the fourth epoch at a position $\alpha = 14^{\rm h}32^{\rm m}27^{\rm s}.40$, $\delta = +33°32'24''.8$ (J2000.0). The angular separation from the cluster center is $35''$, corresponding to a projected physical separation at the cluster redshift of 290 kpc. Table 3.1 gives a summary of photometric observations.

There is no prior detection of a source at the transient's location in the NRAO VLA Sky Survey (Condon et al. 1998) at 1.4 GHz to the survey 5σ detection limit of 2.5 mJy beam^{-1}. There is no X-ray detection at this location in a 5 ks exposure in the Chandra Telescope XBootes survey (Kenter et al. 2005) to the detection limit of 7.8×10^{-15} erg cm^{-2} s^{-1} in the full 0.5-7 keV band.

The transient is consistent with a point source in each of the six ACS detection epochs to the extent we can determine. We performed aperture photometry on the MULTIDRIZZLE-processed ACS images using 3.0 pixel ($0''.15$) radius apertures for i_{775} and 5.0 pixel ($0''.25$)
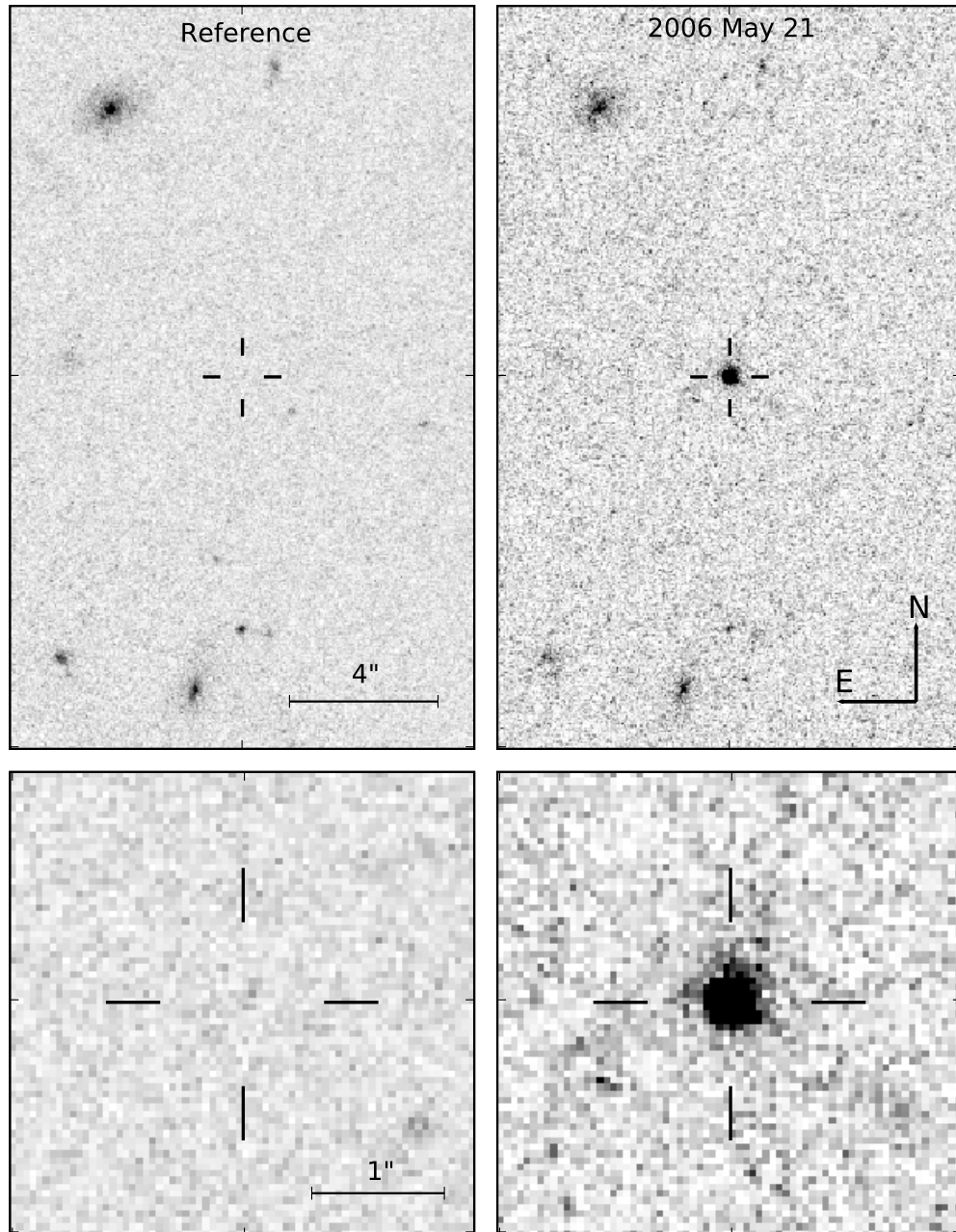
Figure 3.1. Deep stack of the first three epochs in z_{850} totaling 4400 s where the transient is undetected (*top left* and zoomed in, *bottom left*), and the highest-flux epoch eight z_{850} exposure of 1400 s (*top right* and zoomed in, *bottom right*). All images have the same greyscale. The hash marks indicate the transient position and have the same physical scale in all images.
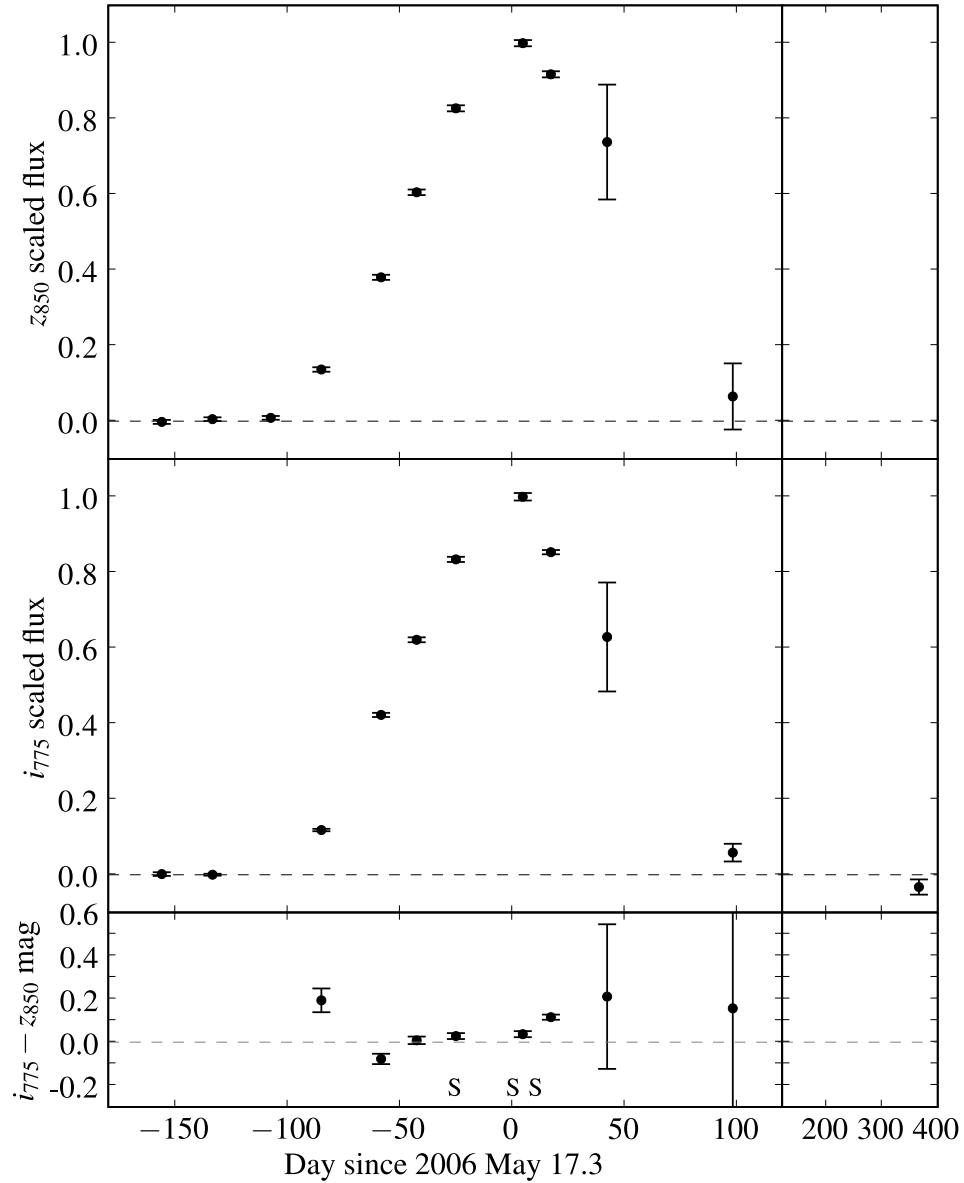
Figure 3.2. Flux light curve for z_{850} (*top panel*) and i_{775} (*middle panel*) scaled to maximum flux. The last three epochs (starting at +42 days) are Subaru FOCAS observations. *bottom panel*: $i_{775} - z_{850}$ color for epochs with significant detection in both bands. Though the color only varies ~ 0.2 magnitudes between the five best measured epochs, there is evidence for evolution. The spectral epochs are marked along the abscissa with an "S."

Table 3.1. Photometric observations of SN SCP06F6

Num.	Date	MJD	Tele-scope	Filter	Exp. (s)	Scaled Flux	Magnitude
1	11/28/05	53716.1	*HST*	i_{775}	175	0.0018 ± 0.0049	> 26.515
				z_{850}	1400	-0.0019 ± 0.0053	> 27.222
2	01/03/06	53738.7	*HST*	i_{775}	375	0.0002 ± 0.0025	> 27.509
				z_{850}	1500	0.0053 ± 0.0049	26.733 ± 0.857
3	01/29/06	53764.6	*HST*	z_{850}	1500	0.0087 ± 0.0050	26.185 ± 0.524
4	02/21/06	53787.2	*HST*	i_{775}	515	0.1183 ± 0.0032	23.395 ± 0.025
				z_{850}	1360	0.1367 ± 0.0059	23.201 ± 0.040
5	03/19/06	53813.7	*HST*	i_{775}	440	0.4229 ± 0.0055	22.012 ± 0.012
				z_{850}	1360	0.3805 ± 0.0067	22.089 ± 0.016
6	04/04/06	53829.6	*HST*	i_{775}	515	0.6216 ± 0.0065	21.593 ± 0.010
				z_{850}	1360	0.6055 ± 0.0074	21.585 ± 0.011
7	04/22/06	53847.0	*HST*	i_{775}	515	0.8343 ± 0.0068	21.274 ± 0.008
				z_{850}	1360	0.8276 ± 0.0080	21.246 ± 0.009
8	05/21/06	53876.8	*HST*	i_{775}	295	1.0000 ± 0.0099	21.077 ± 0.009
				z_{850}	1400	1.0000 ± 0.0082	21.040 ± 0.008
9	06/03/06	53889.3	*HST*	i_{775}	800	0.8534 ± 0.0056	21.249 ± 0.006
				z_{850}	1200	0.9176 ± 0.0081	21.134 ± 0.008
10	06/28/06	53914.4	Subaru	i_{775}	960	0.6290 ± 0.1441	21.581 ± 0.211
				z_{850}	480	0.7384 ± 0.1520	21.370 ± 0.189
11	08/23/06	53970.3	Subaru	i_{775}	600	0.0586 ± 0.0234	24.158 ± 0.368
				z_{850}	600	0.0654 ± 0.0875	> 23.080
12	05/18/07	54238.5	Subaru	i_{775}	2280	-0.0324 ± 0.0201	$\ldots$

Note. — Flux measurements scaled relative to highest flux epoch; effective zeropoints are 21.077 for i_{775} and 21.040 for z_{850}.

radius apertures for z_{850}. Aperture corrections were taken from Table 3 of Sirianni et al. (2005). The systematic error due to the known color dependence of z_{850} aperture correction (see Sirianni et al. 2005) is estimated to be less than 0.015 mag.

After the transient had left the visibility window of *HST* it remained visible from Mauna Kea for several months. Three additional photometry points were obtained with the Faint Object Camera and Spectrograph (FOCAS; Kashikawa et al. 2002) on the Subaru telescope on 2006 June 28, 2006 August 23, and the next year on 2007 May 18. The June observations suffered from poor weather conditions (seeing $\gtrsim 2''$). All observations were cosmic ray-rejected using 120 s exposures. We performed aperture photometry using a $1''.04$ radius aperture and estimated photometric errors as described by Morokuma et al. (2008). In order to express magnitudes in the ACS filter system, we determined Subaru image zeropoints by cross-correlating the photometry of nine surrounding stars in the ACS and Subaru images. The Subaru FOCAS i' and z' filters are similar enough to ACS i_{775} and z_{850} that there is no significant trend with stellar color.

A deep stack of the first three epochs in z_{850} totaling 4400 s (Fig. 3.1) and first two epochs in i_{775} totaling 550 s provide limits on the magnitude of a possible progenitor star

(if galactic) or host galaxy (if extragalactic). No progenitor star is detected in a 3.0 pixel radius aperture centered at the position of the transient (known to < 0.2 pixels) to a 3σ upper limit of $i_{775} > 26.4$ and $z_{850} > 26.1$ (Vega magnitudes are used throughout this Letter). There is no sign of a host galaxy in the 1 arcsec^2 surrounding the transient to a surface brightness 3σ limit of 25.0 mag arcsec^{-2} and 25.1 mag arcsec^{-2} in z_{850} and i_{775}, respectively. However, there is a 6σ detection in a 3.0 pixel radius aperture of a $\sim$25.8 mag object $1''.5$ southwest of the transient position in z_{850} (Fig. 3.1, *lower left*). If the transient is extragalactic, this might represent a faint host galaxy.

The transient increased in brightness in each of epochs four through eight before finally declining in the ninth epoch, resulting in a rise time of approximately 100 days (Fig. 3.2). A fit to the brightest five ACS z_{850} photometry points gives a date of max of 2006 May 17.3 (MJD 53872.3). The declining part of the light curve, although sparsely measured, is consistent with symmetry about the maximum. The final photometry point approximately one year after maximum light shows no detection. The $i_{775} - z_{850}$ color is approximately constant over the 50 days preceding maximum light, but does show significant signs of evolution at early times and after maximum light.

3.2   Spectroscopy

Spectroscopy was acquired on three dates (Fig. 3.3): 2006 April 22 (-25 days) using Subaru FOCAS, 2006 May 18 (+1 day) using VLT FORS2 (Appenzeller et al. 1998), and 2006 May 28 (+11 days) with Keck LRIS (Oke et al. 1995). The Subaru spectrum covers wavelengths longward of 5900 Å, while the VLT and Keck spectra cover bluer wavelengths. The VLT spectrum (observed at airmass > 2) is corrected for differential slit loss by applying a linear correction with a slope of 0.25 per 1000 Å, derived from a comparison to the Keck spectrum, which covers the entire wavelength range of the VLT spectrum. The Keck observation was made at the parallactic angle, while Subaru FOCAS is equipped with an atmospheric dispersion corrector, making these observations more reliable measures of relative flux.

The spectra show a red continuum and several broad absorption features: a possible absorption feature at 4320 Å (FWHM $\sim$ 180 Å), three strong features at 4870 Å (FWHM $\sim$ 200 Å), 5360 Å (FWHM $\sim$ 230 Å) and 5890 Å (FWHM $\sim$ 280 Å), and a weaker absorption feature at 6330 Å (FWHM $\sim$ 270 Å). Including uncertainty in continuum shape, errors are estimated to be 25 Å.

We compared the spectra to all supernova types using the χ^2 fitting program described in Howell et al. (2005) as well as the program SNID (Blondin & Tonry 2007). No match was found with either program.

If the transient is galactic ($z = 0$), the absorption features at 4320 Å and 4870 Å are consistent with Hγ (4341 Å) and Hβ (4861 Å) respectively. However, there is no significant Hα (6563 Å) emission or absorption, which would be expected for the presence of strong Hγ and Hβ features. (Although there is slight evidence for emission at 6563 Å in the
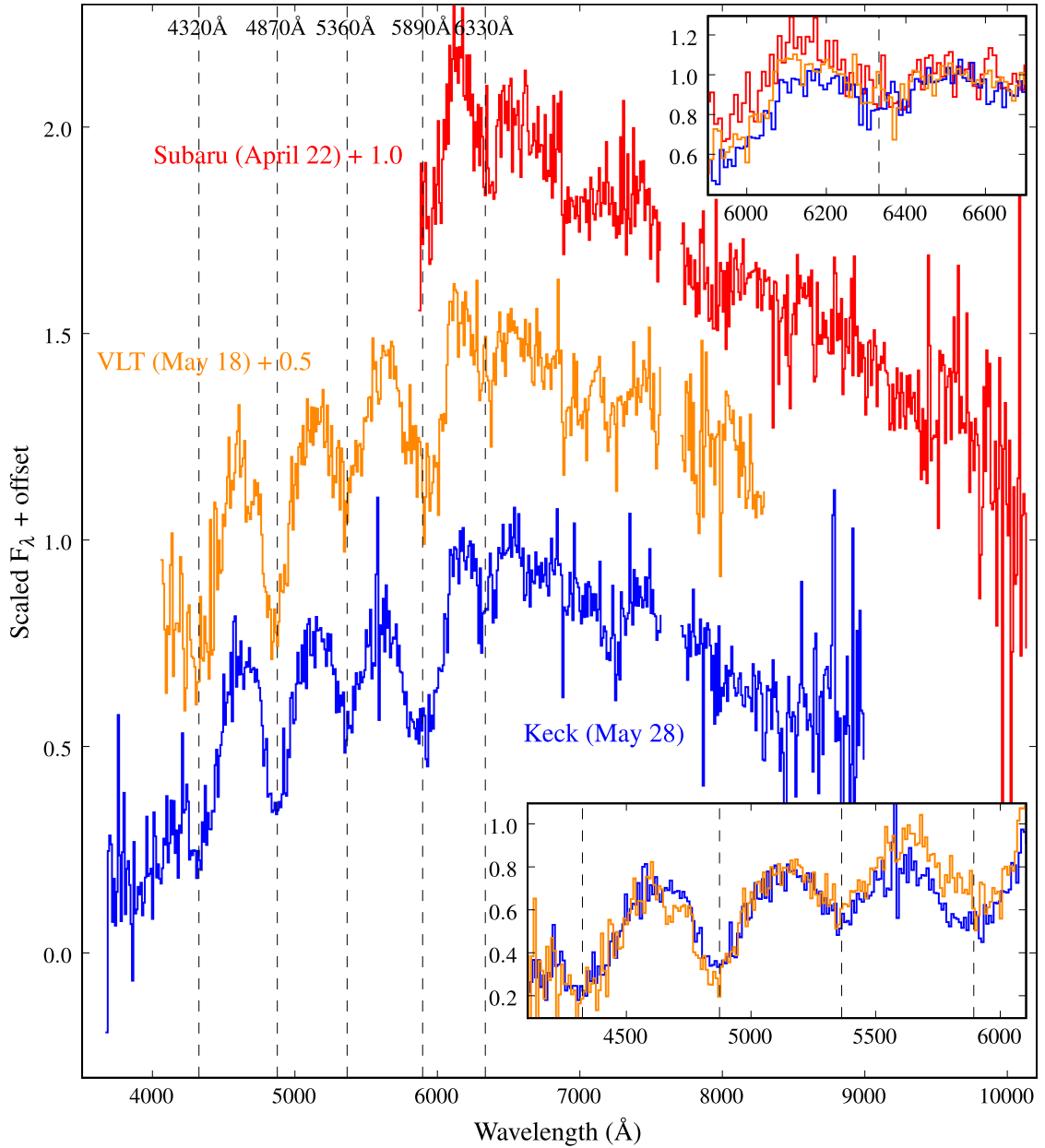
Figure 3.3. Spectra averaged in 10 Å bins. Vertical dotted lines indicate the approximate absorption band centroids. Spectra are normalized to match in the red continuum. Inset figures show regions where spectra differ. *Top Inset*: Overplot of all three spectra in the range 5900 Å - 6700 Å, demonstrating apparent evolution of the flux at ∼6150 Å relative to the red continuum. *Bottom Inset*: Overplot of VLT and Keck spectra (no offset) demonstrating apparent evolution at 4670 Å and of the absorption feature at 5890 Å.

Keck spectrum, this is not seen in the VLT or Subaru spectra.) It is therefore unlikely that the 4320 Å and 4870 Å features are due to hydrogen. No other narrowband emission or absorption lines are detected. From the slope of the red continuum we derive a lower limit blackbody temperature of 6500 K. The shape of the continuum is inconsistent with $F_\lambda \propto \lambda^{-5/3}$ synchrotron radiation.

If the transient is extragalactic, the absence of Lyman α absorption features shortward of 4500 Å places a hard upper limit of $z \lesssim 2.7$ on its redshift. Among redshifts $0 < z < 2.7$, the cluster redshift of $z = 1.112$ is of specific interest; the transient is located a small projected distance from the center of the cluster. At this redshift, the absorption feature at 5890 Å is consistent with Mg II $\lambda\lambda2796, 2803$. However, the remaining features are not identified at this redshift. At $z = 1.112$, a peak apparent magnitude of $i_{775} = 21.0$ implies a peak bolometric magnitude of approximately -22.1.

A comparison of the three spectra shows evidence for spectral evolution. The flux at ~6150 Å consistently decreases relative to the red continuum over time (Fig. 3.3, *upper inset*). Over the 10 day period from the VLT to the Keck spectrum, the absorption feature at 5890 Å appears to move toward shorter wavelengths, while a small absorption feature at 4670 Å in the VLT spectrum seems to disappear in the Keck spectrum (Fig. 3.3, *lower inset*).

3.3 Discussion

The key features of SN SCP06F6 are as follows: a rise time of ~100 days with a roughly symmetric light curve; small but statistically significant color variations across the light curve; no detected host galaxy or progenitor; broad spectral features in the blue, with a red continuum, and some evidence for spectral evolution. Below, we first discuss constraints on the distance to the source. Next we consider the possibility that the transient is the result of microlensing, finding this to be unlikely. Lastly, we search for objects in the SDSS spectral database, finding no convincing matches.

3.3.1 Distance from Parallax

Any detection of proper motion or parallax would be strong evidence of a galactic source. We tested for this by fitting the position of the transient in each of the six ACS detection epochs using a two-dimensional Gaussian (Fig. 3.4). The fit uncertainty is dominated by residual distortion and alignment errors in most epochs. These errors are on the order of 0.1 to 0.2 pixels. The most discrepant positions differ by approximately 0.25 pixels ($0''.0125$). As a whole, the positions are consistent with no proper motion or parallax and give little indication of either. The upper limit on parallax is 0.3 pixels ($0''.015$), which gives a lower limit on distance of ~70 pc.
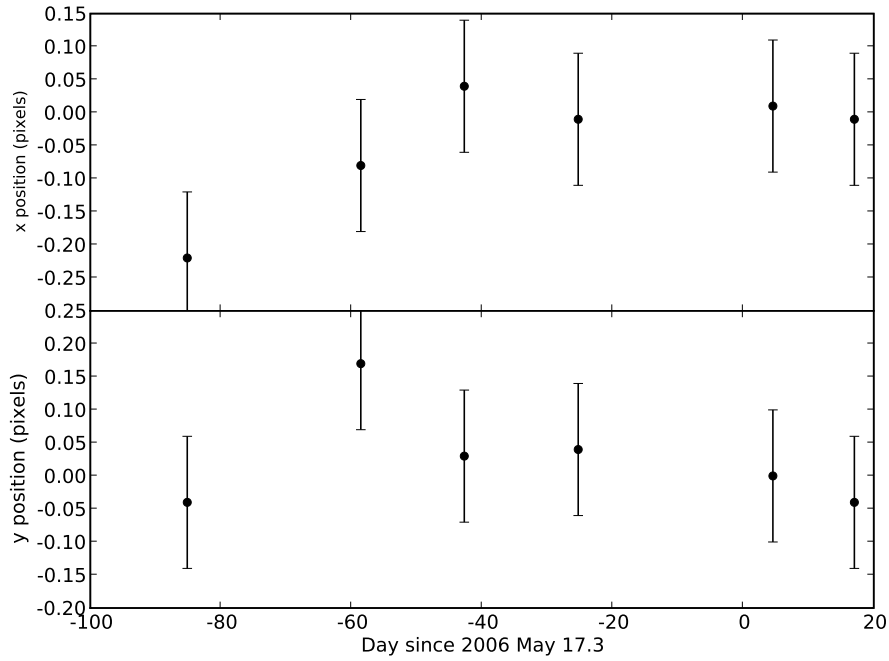
Figure 3.4. Position of the transient in each of the 6 ACS detection epochs. 1 pixel is $0''.05$. The upper limit on parallax is 0.3 pixels.

3.3.2 Distance from Reference Limits

We can derive a more significant constraint on distance from reference image magnitude limits, assuming that the transient is an explosion and a progenitor star exists. The dimmest stars (aside from neutron stars) known to undergo explosions are white dwarfs (WDs). WDs range in absolute magnitude from approximately 10 mag ($T_{\rm eff} \sim 25000$ K) to approximately 16 mag ($T_{\rm eff} \sim 3000$ K). If we assume the progenitor is a WD with absolute magnitude $i_{775} = 13$, the reference image 3σ upper limit of $i_{775} > 26.4$ gives a distance 3σ lower limit of 4.8 kpc. Because the source is at high galactic latitude ($b = 67.3°$), we are looking nearly directly out of the plane of the galaxy. Given a Milky Way scale height for WDs of (275 ± 50) pc (**Boyle 1989**), this places the source firmly outside of the plane of the Galaxy. However, a galactic WD progenitor is still possible, if it is a relatively cool white dwarf residing in the galactic halo. If the progenitor is a source dimmer than $i_{775} = 13$ mag (e.g., a cooler WD or neutron star), the constraints on distance are weaker.

3.3.3 A Microlensing Event?

Although the symmetry of the light curve (Fig. 3.2) suggests that the transient is a microlensing event, this interpretation is unlikely. The light curve is dramatically broader than

the theoretical light curve for microlensing of a point source by a single lens (Paczynski 1986). The typical light curve FWHM of high-magnification (peak magnification $\gtrsim 300$) microlensing events is on the order of a few hours (e.g., Abe et al. 2004; Dong et al. 2006) whereas the transient's light curve FWHM is $\sim$100 days with a peak magnification 3σ lower limit of $\sim$120. Also, the color evolves a small but significant amount over the light curve, particularly between epochs eight and nine. Some of these difficulties can be overcome if we assume the source is resolved; this can both change the shape of the light curve and allow for color variation as different source regions are differentially magnified. However, this typically results in a lower peak magnification. Finally, microlensing would still not explain the mysterious spectrum.

3.3.4   Search for Similar Objects in SDSS

In an effort to identify objects with similar spectra, we cross-correlated the broad features of the spectrum with the SDSS spectral database. Each SDSS spectrum was warped with a polynomial function to best fit the Keck spectrum, based on a least squares fit. The value of the root mean square of the difference between the spectra was used to determine the correlation. An allowance for relative redshift was made, with the requirement that the spectra overlapped in the range of the strongest features (3500 Å to 6200 Å). No convincing matches were found. Changing the warping function between linear and quadratic and varying the wavelength range used in the fit altered which SDSS objects had the highest correlation, but did not result in a more convincing match. The SDSS objects with the highest correlation were broad absorption line quasars (BAL QSOs) at various redshifts and carbon (DQ) WDs. Although BAL QSOs do have similarly broad features, they don't exhibit the spacing or rounded profiles of those of the transient. Also, BAL QSOs typically include emission features. The DQ WDs most similar to the transient are known as DQp WDs. Like the transient, DQp WDs have broad, rounded absorption features between 4000 Å and 6000 Å with a red continuum (see, e.g., Hall & Maxwell 2008). However, the positions and spacing of the absorption features shortward of 5000 Å differ greatly from those of the transient spectrum. In addition, DQp WDs show increased emission toward the UV, which is not seen in the transient.

The absence of similar spectra in the SDSS database implies that if the transient is due to a galactic variable, it is either always below the SDSS detection threshold in quiescence or extremely rare, or both. If the transient is extragalactic, the apparent absence of similar transients in other deep variable surveys (e.g., other high-redshift supernova surveys) might be understood if similar transients are rare at peak apparent magnitudes of 21 but more common at much fainter magnitudes.

3.4 Summary

Since the initial publication of this data, many possible scenarios have been suggested to explain the observations. Various explanations have been considered by, e.g., Gänsicke et al. (2009), Soker et al. (2010) and Chatzopoulos et al. (2009). It appears that the transient may be a rare type of supernova, with redshift $z = 1.189$ (Quimby et al. 2009; Pastorello et al. 2010). However, its precise explanation is still uncertain.

CHAPTER 4

Supernova Candidate Selection and Typing

During the survey, our aim was to find as many supernovae as possible and find them as early as possible in order to trigger spectroscopic and NICMOS follow-up. Thus, software thresholds for flagging candidates for consideration were set very low, and all possible supernovae were carefully considered by a human screener. Over the course of the survey, thresholds were changed and the roster of people scanning the subtractions changed. As a result, the initial candidate selection process was inclusive but heterogeneous, and depended heavily on human selection. This made it difficult to calculate a selection efficiency for the SN candidates selected during the survey (listed in Tables 3 and 4 of Dawson et al. 2009). This is a difficulty for a rate calculation since knowing the survey selection efficiency is fundamental to calculating an accurate rate.

Therefore, in this chapter, we select an independent SN candidate sample (without regard for the sample selected during the survey) using automated selection wherever possible. Candidates are selected without regard for cluster membership (which is only known from follow-up spectroscopy once the candidate has already been found). We determine SN types for both cluster and non-cluster SNe. The cluster SNe are then considered further in Chapter 5 in calculating the cluster rate. The non-cluster SNe are considered further in Chapter 6 in calculating the volumetric field rate. The SN type determination here is also used to classify candidates for use in the cosmological analysis from the survey (Suzuki et al. 2011).

The automated selection consists of initial detection in pairs of subtracted images (§4.1.1; 86 candidates selected), and subsequent requirements based on the light curve of each candidate (§4.1.2; 60 candidates remaining). The selection efficiency for these two steps is later calculated via a Monte Carlo simulation. In §4.2 we assign a type (SN Ia, core-collapse SN, or other) to each of the remaining 60 candidates based on all data available (including triggered follow-up observations). For this last step we do not calculate an efficiency or completeness. Instead we estimate the classification uncertainty of the assigned type for each candidate individually. For most candidates the uncertainty in the type is negligible

thanks to ample photometric and spectroscopic data.

4.1 Automated Selection

4.1.1 Initial Detection

For the purpose of initially detecting candidates, we use only "search" visits (filled circles in Fig. 2.1) and disregard the "follow-up" visits (open circles in Fig. 2.1). (In the following section we will use any available "follow-up" visits to construct more complete light curves for the candidates discovered in this section.) We use the MULTIDRIZZLE-combined, cosmic ray-rejected, z_{850} image from each "search" visit. We consider only regions in this image that are covered by three or more z_{850} exposures. With less than three exposures, the combined images are too heavily contaminated by cosmic rays to be practically searchable for SNe. Although there are typically four z_{850} exposures, the dither pattern used in the survey means that not all regions of the combined image have four exposures. The ACS camera is a mosaic of two 2048×4096 pixel CCD chips (1 pixel = $0.05''$) separated by $2.5''$. The z_{850} exposures were dithered to cover this gap, meaning that a $5''$ wide region in the center of the image and $2.5''$ wide regions on either side of the image are only covered by two exposures and thus are not searchable. Due to orbital constraints, the position angle of *HST* changes between each visit. This means that the unsearchable "gap" region rotates over the field between visits, and that the outer parts of the field are observed in some visits, but not others (Fig. 4.1, second row). The regions around bright stars are also considered "not searchable" and are similarly masked.

For each "search" visit to each cluster, we follow these four steps:

1. **A reference image is made** by combining images from other visits to the cluster. All visits that are either 50 or more days before the search epoch or 80 or more days after the search epoch are included. If there are no epochs outside this 130 day range, the range is narrowed symmetrically until one epoch qualifies. Masked pixels in each visit's image do not contribute to the stacked reference image (Fig. 4.1, third row).

2. **A subtracted image is made** by subtracting the stacked reference image from the search epoch image. A map of the sky noise level in the subtraction is made by considering the noise level of the search epoch image and the noise level of each reference image contributing to a given region. Any area masked in either the search epoch or stacked reference image is masked in the subtracted image (Fig. 4.1, fourth row).

3. **Candidates in the subtraction are identified by software.** To be flagged, a candidate must have three contiguous pixels with a flux 3.4 times the local sky noise level in the subtraction (as determined by the sky noise map above). Once flagged, it must fulfill the following four requirements:
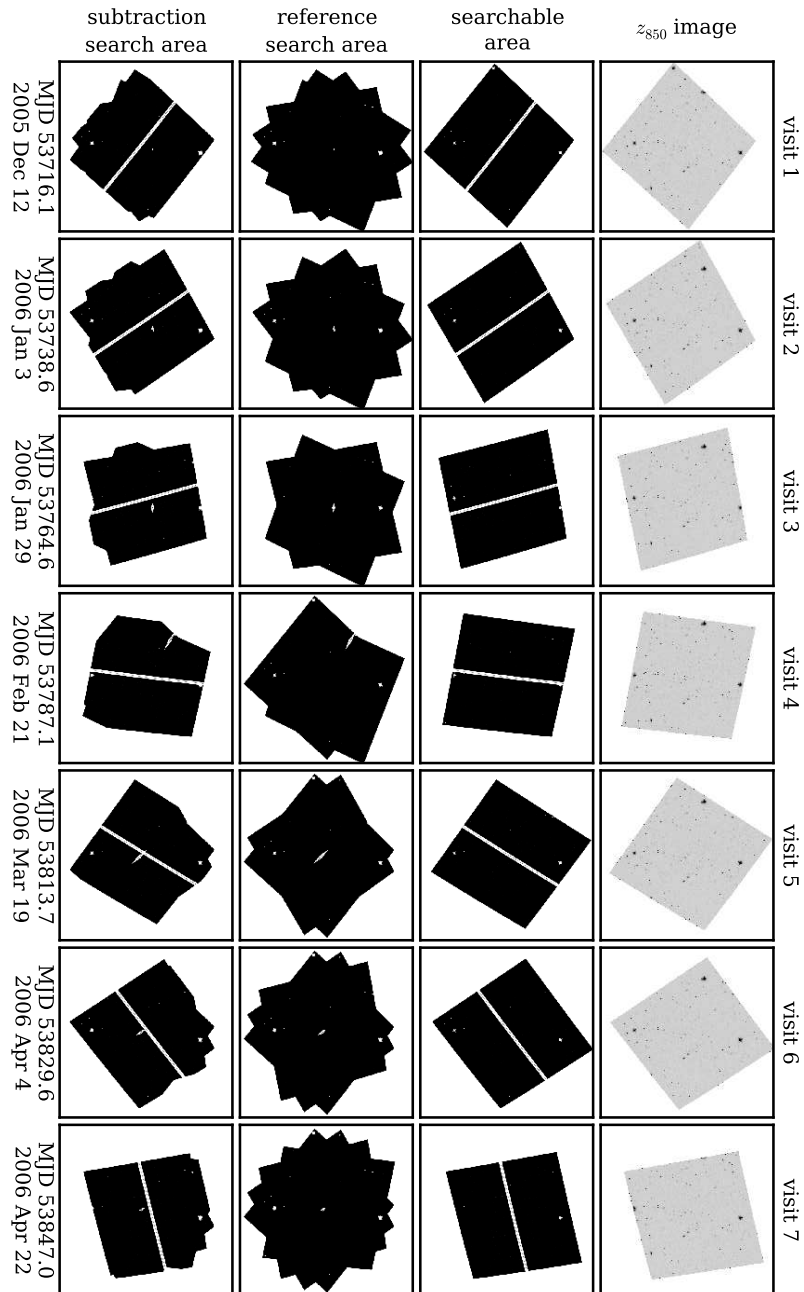
Figure 4.1. An example of image orientation and searchable regions for cluster ISCS J1432.4+3332. Each column represents an observation of the cluster. The first row is the z_{850} image for that visit. The second row is the part of that image that is searchable. The third row shows the searchable area of the stacked reference image used in the subtraction for this visit. The fourth row is the searchable area in the subtraction (the intersection of the second and third rows).

- MULTIDRIZZLE-combined image: A total signal-to-noise ratio (including sky and Poisson noise) of 5 or more in a 3 pixel radius aperture.

- MULTIDRIZZLE-combined image: A total signal-to-noise ratio of 1.5 or more in a 10 pixel radius aperture.

- Individual exposures: A signal-to-noise ratio of 1 or greater in a 3 pixel radius aperture in three or more individual exposures.

- Individual exposures: A candidate cannot have an individual exposure with a flux more than 20σ greater than the flux in the lowest flux exposure *and* a second individual exposure with flux more than 10σ greater than the flux in the lowest flux exposure.

The first requirement is designed to eliminate low significance detections on bright galaxies. The second requirement helps eliminate dipoles on bright galaxy cores caused by slight image misalignment. The third and fourth requirements are aimed at false detections due to cosmic ray coincidence. They require the candidate to be detected in most of the exposures and allow no more than one exposure to be greatly affected by a cosmic ray. On the order of five to ten candidates per subtraction pass all the requirements, resulting in approximately 1000 candidates automatically flagged across the 155 search visits.

4. **Each candidate is evaluated by eye in the subtraction.** Because the position angle changes between each epoch, the orientation of stellar diffraction spikes changes, causing the majority of the false detections. These are easy to detect and eliminate by eye. Occasionally there are mis-subtractions on the cores of bright galaxies that pass the above requirements. Only completely unambiguous false detections are eliminated in this step. If there is any possibility the candidate is a real SN, it is left in the sample for further consideration.

After carrying out the above four steps for all 155 search visit, 86 candidates remain. At this point, candidates have been selected based only on information from a single z_{850} subtraction.

4.1.2   Lightcurve Requirements

The 86 remaining candidates still include a considerable number of non-SNe. We wish to trim the sample down as much as possible in an automated way, so that we can easily calculate the efficiency of our selection. For each candidate, we now make three further automated requirements based on i_{775} data (if available) and the shape of the z_{850} light curve. The requirements and number of candidates remaining after each requirement are summarized in Table 4.1.

First, we require that if i_{775} data exists for the epoch in which the candidate was detected, there be positive flux in a 2 pixel radius aperture at the candidate location in the

Table 4.1. Light curve requirements for candidates

Requirement	Candidates Remaining
Before light curve requirements	86
Positive i_{775} flux (if observed in i_{775})	81
2σ Detection in surrounding epochs	73
If declining, Require two 5σ detections	60

i_{775} image. From our SN light curve simulations, we find that virtually all SNe should pass (near maximum light there is typically enough SN flux in the i_{775} filter to result in a positive total flux, even with large negative sky fluctuations). Meanwhile, about half of the cosmic rays located far from galaxies will fail this test (due to negative sky fluctuations). If there is no i_{775} data for the detection epoch, this requirement is not applied. Even though nearly all SNe are expected to pass, we account for any real SNe that would be removed in our Monte Carlo simulation.

Second, we require that the light curve does not rise and fall too quickly: if there is a "search" visit less than 60 days before the detection visit and also one less than 60 days after the detection visit, the candidate must be detected at a 2σ level in at least one of these two visits. SNe Ia have light curves wide enough to be detected at this level in two epochs spaced apart by 60 days. However, cosmic rays in one z_{850} image are unlikely to be repeated in the same spot in two epochs and thus will be removed. This requirement is also included in our Monte Carlo simulation.

The third and final requirement aims to eliminate candidates that were significantly detected in only the first epoch and that then faded from view. Such candidates would not have been followed up spectroscopically and it would typically be impossible to tell if such candidates were SNe (and if so, Type Ia or core collapse) on the basis of a single detection. We chose to eliminate any such candidates and account for this elimination in our Monte Carlo simulation, rather than dealing with an "untypeable" candidate. Specifically, if a candidate is found on the decline (in the first search epoch), we require two epochs with 5σ detections. For high-redshift ($z \sim 1$) SNe Ia, this requirement means that the first epoch will be at approximately maximum light, and most of the SN decline is captured, making it possible to confirm a SN and estimate a type. For candidates that are only significantly detected in the last search epoch, typing is not a problem because additional ACS orbits were typically scheduled in order to follow such candidates.

After these requirements 60 candidates remain. The automatic selection means that we can easily calculate the completeness of the selection so far; any real SNe Ia removed will be accounted for in the "effective visibility time" which is calculated using a Monte Carlo simulation.

4.2 Type Determination

We now use all available information about each candidate (spectroscopic confirmation, host galaxy redshift, all light curve information, as well as host galaxy luminosity and color) to classify each of the 60 remaining candidates as image artifact, active galactic nucleus (AGN), core-collapse SN (SN CC), or SN Ia.

4.2.1 Image Artifacts

Although the automated selections were designed to eliminate image artifacts such as subtraction residuals and cosmic rays, they were made to be somewhat tolerant so that real SNe were not eliminated. The result is that some artifacts slip through. Candidates located
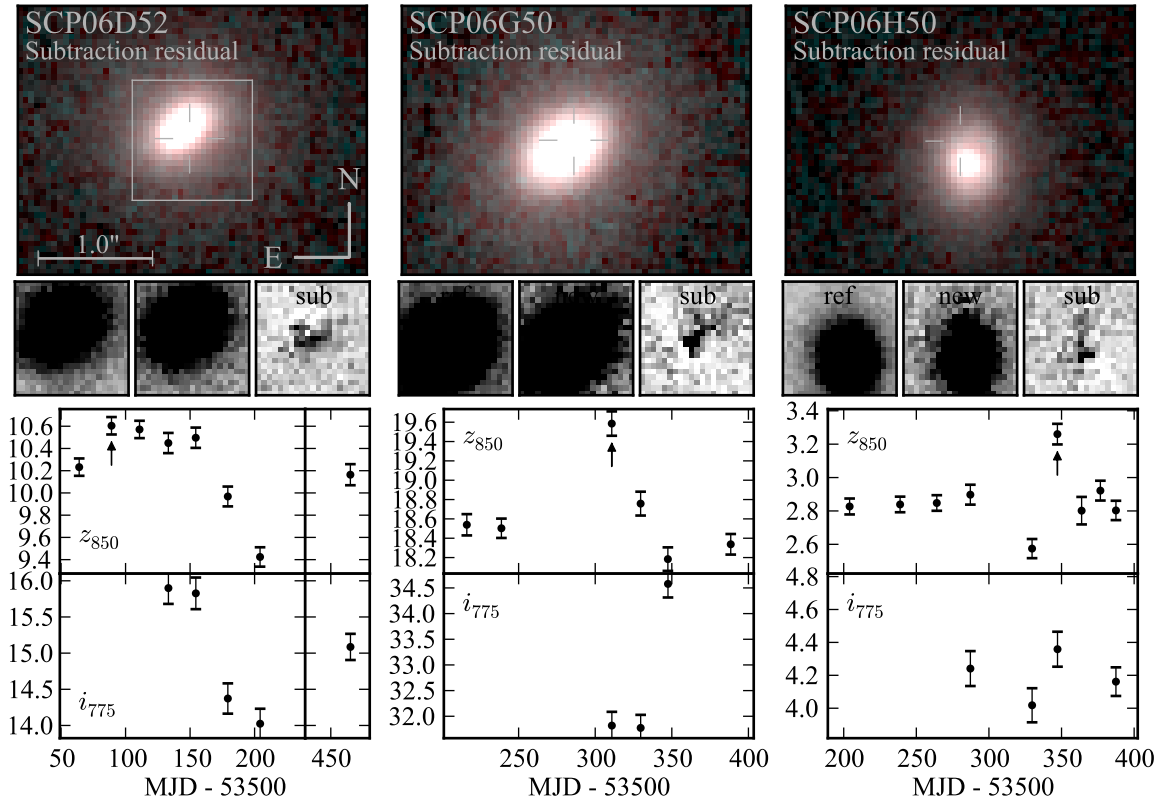
Figure 4.2. Images and light curves of the candidates classified as image artifacts (cosmic ray hits and/or subtraction residuals). For each candidate, the *top panel* shows the two-color stacked image (i_{775} and z_{850}) of the host galaxy, with the position of the transient indicated. The *three smaller panels* below the stacked image show the reference, new, and subtracted images for the discovery visit. The *bottom panel* shows the light curve at the transient position (including host galaxy light) in the z_{850} (*top*) and i_{775} (*bottom*) bands. The y axes have units of counts per second in a 3 pixel radius aperture. The effective zeropoints are 23.94 and 25.02 for z_{850} and i_{775}, respectively. The discovery visit is indicated with an arrow in the z_{850} plot. [*Continued on next three pages.*]

SCP06T53
Subtraction residual
N
E
1.0"
ref new sub
z_{850}
i_{775}
MJD - 53500

SCP06T51
Subtraction residual
ref new sub
z_{850}
i_{775}
MJD - 53500

SCP06W51
Subtraction residual
sub
z_{850}
i_{775}
MJD - 53500

SCP06W52
Subtraction residual
sub
z_{850}
i_{775}
MJD - 53500

SCP06W53
Subtraction residual
sub
z_{850}
i_{775}
MJD - 53500

SCP06D50
Cosmic ray hit
ref new sub
z_{850}
i_{775}
MJD - 53500
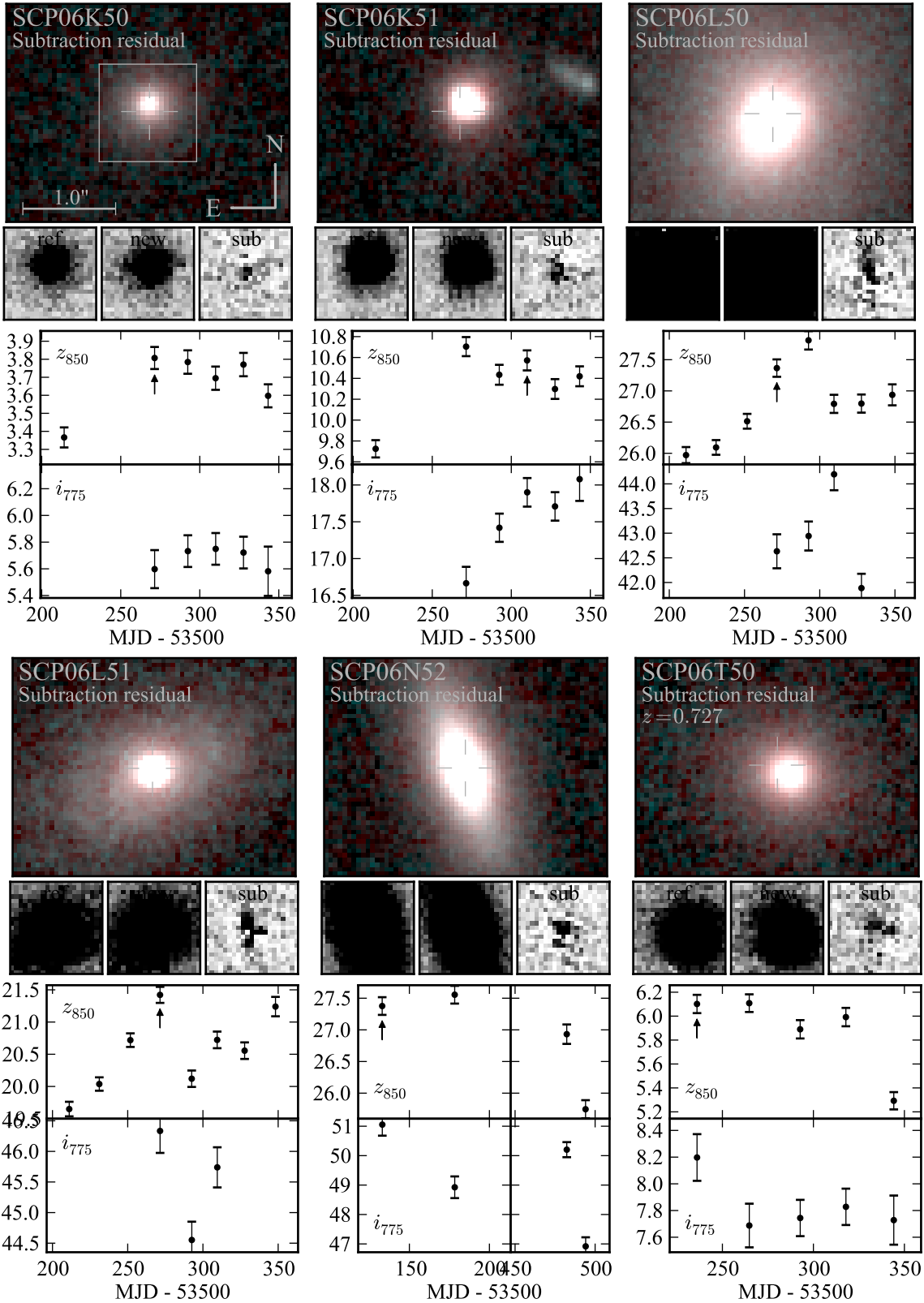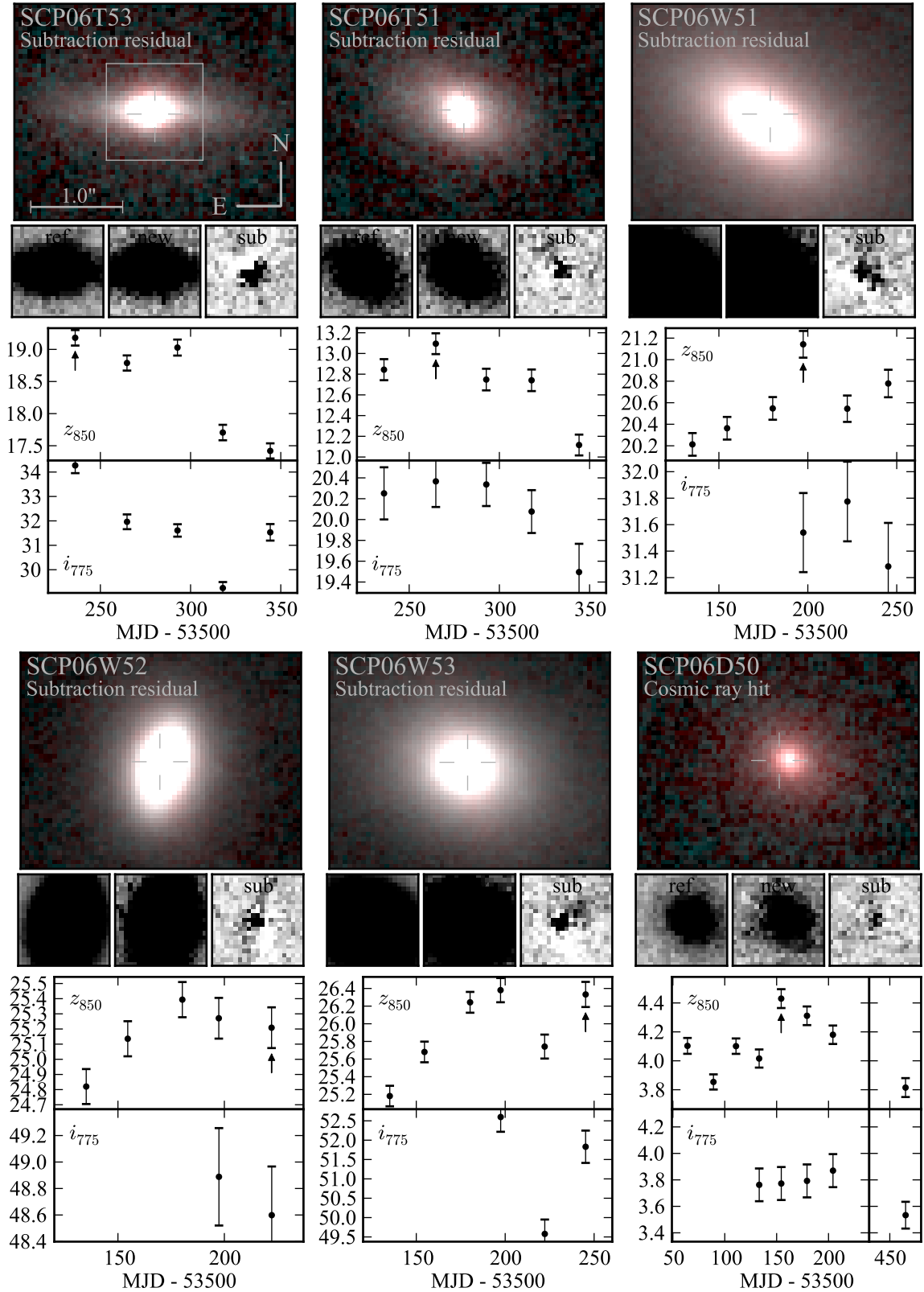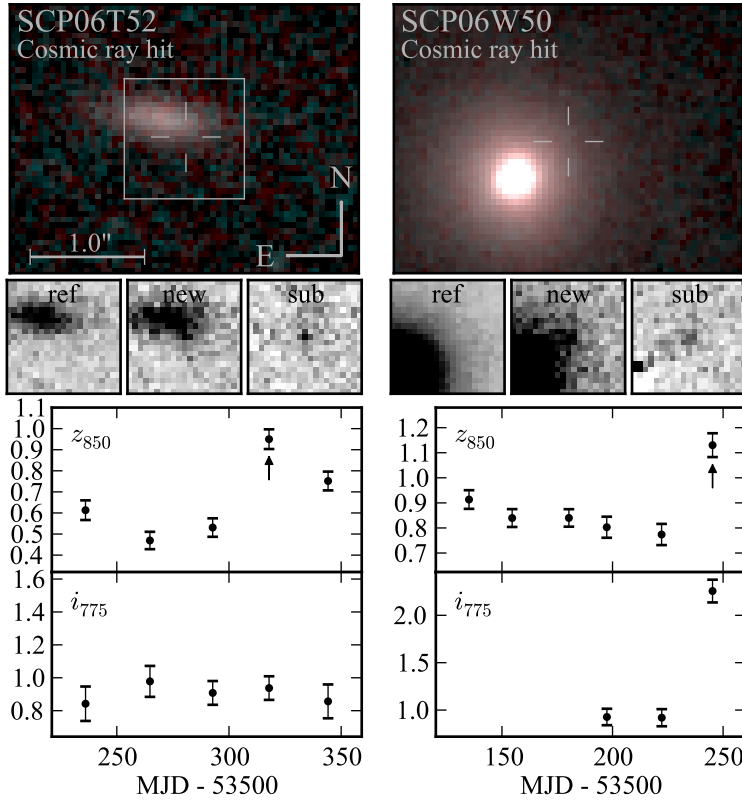
close to the cores of relatively bright galaxies that show adjoining negative and positive areas in subtractions are likely to be caused by mis-alignment between the reference and search image. For such candidates, we inspected the full light curve for consistency with the general shape of a SN Ia light curve. For fourteen of these, the light curve is completely inconsistent with that of a SN Ia. Their light curves have either multiple peaks, long flat portions followed by one or two lower points, and/or i_{775} data that shows no change. We classify these fourteen candidates as subtraction residuals with negligible classification uncertainty (very unlikely that any are SNe Ia). These candidates are shown in Figure 4.2.

Candidates where one or two of the four z_{850} exposures was clearly affected by a cosmic ray or hot pixel may be false detections. These can pass the automated cosmic ray rejection when they occur on a galaxy. For two such candidates, we used the lack of any change in the i_{775} light curve to rule out a SN Ia: fitting SN templates with a range of redshifts and extinctions resulted in observed i_{775} fluxes too low by 4σ or more, given the z_{850} increase. One other candidate, SCP06W50, is less certain. It was discovered in the last visit to the cluster, making it difficult to constrain a template light curve. There is clearly a hot pixel or cosmic ray in one z_{850} exposure, but there appears to be some excess flux in the other three exposures as well. Also, there is a point-source like detection in i_{775}, but offset $\sim$1.2 pixels from the z_{850} detection. While the i_{775} detection may also be a cosmic ray, it is possible that this candidate is a SN caught very early. The elliptical "host" galaxy was not observed

spectroscopically, but we estimate its redshift to be $0.60 < z < 0.85$ based on the color of $i_{775} - z_{850} = 0.55$ and stellar population models of **Bruzual & Charlot** (2003, hereafter BC03).

Of the 17 total candidates classified as image artifacts, SCP06W50 is the only one with significant uncertainty. However, this uncertainty does not affect the cluster SN Ia rate as the host galaxy is clearly in the cluster foreground.

4.2.2 AGN

Candidates positioned directly on the cores of their host galaxies may be AGN. Four such candidates were spectroscopically confirmed as AGN: SCP06L22 ($z = 1.369$), SCP06V6 ($z = 0.903$) and SCP05X13 ($z = 1.642$) and SCP06U3 ($z = 1.534$). A fifth candidate,
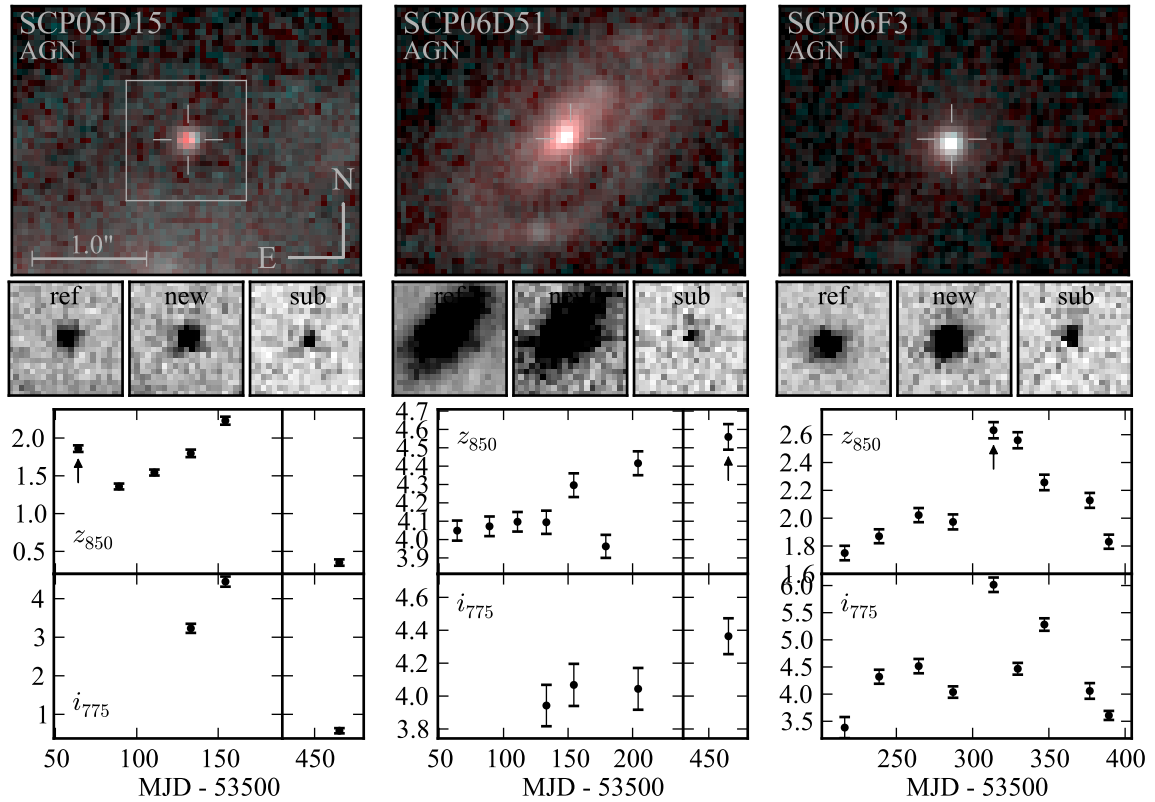
Figure 4.3. Images and light curves of the candidates classified as AGN. For each candidate, the *top panel* shows the two-color stacked image (i_{775} and z_{850}) of the host galaxy, with the position of the transient indicated. The *three smaller panels* below the stacked image show the reference, new, and subtracted images for the discovery visit. The *bottom panel* shows the light curve at the transient position (including host galaxy light) in the z_{850} (*top*) and i_{775} (*bottom*) bands. The y axes have units of counts per second in a 3 pixel radius aperture. The effective zeropoints are 23.94 and 25.02 for z_{850} and i_{775}, respectively. The discovery visit is indicated with an arrow in the z_{850} plot. [*Continued on next two pages.*]
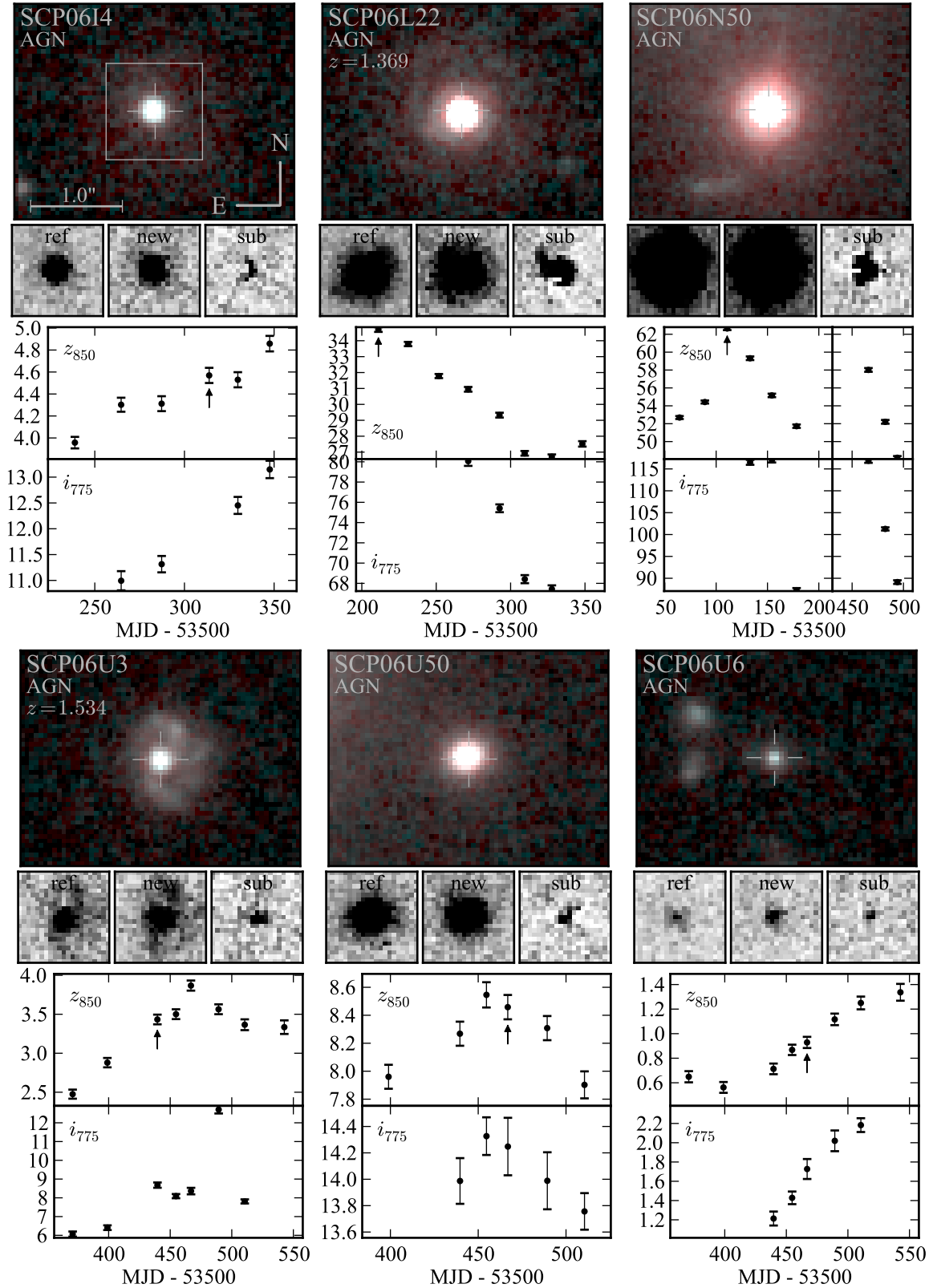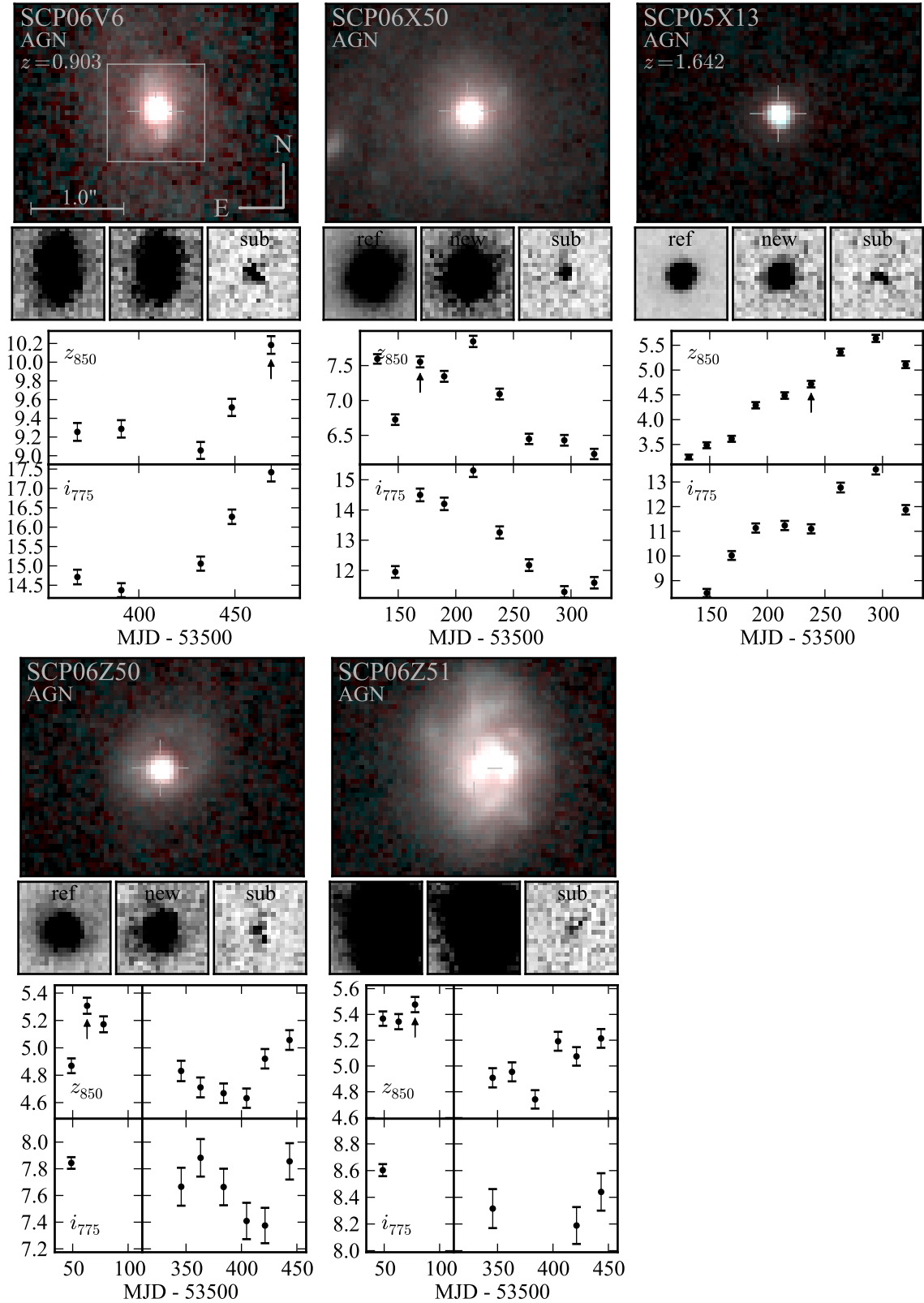
SCP06F3, is spectroscopically consistent with an AGN at $z = 1.21$, but is less certain (see spectroscopy reported in Morokuma et al. 2010). SCP06L22, SCP05X13, SCP06U3 and SCP06F3 also have light curves that are clearly inconsistent with SNe Ia (observer frame rise times of 100 days or more, or declining phases preceding rising phases; see Fig. 4.3). Of the "on core" candidates that were not observed spectroscopically, five exhibit light curves that decline before rising or have rise times of 100 days or more. A sixth candidate, SCP06Z51 exhibited slightly varying fluxes that could be due to either subtraction residuals or an AGN. However, its light curve is clearly inconsistent with a SN Ia, especially considering the apparent size, magnitude and color of the host galaxy. Summarizing, there are 11 "on-core" candidates certain not to be SNe Ia.

Three other "on-core" candidates are also considered likely AGN on the basis of their light curves: SCP06Z50, SCP06U50 and SCP06D51. SCP06Z50 has a rise-fall behavior in the first three z_{850} observations of its light curve that *could* be consistent with a SN Ia light curve. However, given that the host galaxy is likely at $z \lesssim 1$ based on its magnitude and color, the SN would be fainter than a normal SN Ia by 1 magnitude or more. Considering the proximity to the galaxy core and the additional variability seen in the last two observations, SCP06Z50 is most likely an AGN. The light curve of candidate SCP06U50 also exhibits a rise-fall that could be consistent with a supernova light curve. However, its host is morphologically elliptical and likely at $z \lesssim 0.7$ based on its color. At $z \lesssim 0.7$, a SN Ia would have to be very reddened ($E(B - V) \gtrsim 1$) to match the color and magnitude of the SCP06U50 light curve. As this is very unlikely (considering that the elliptical host likely contains little dust), we conclude that SCP06U50 is also most likely an AGN. Finally, SCP06D51 was discovered in the last visit, on the core of a spiral galaxy. We classify it as an AGN based on the earlier variability in the light curve. As these galaxies are all most likely in the cluster foregrounds, even the small uncertainty in these classifications is not a concern for the cluster rate calculation here.

Note that one of the candidates classified here as a clear AGN, SCP06U6, was reported as a SN with unknown redshift by Dawson et al. (2009), due to the fact that spectroscopy revealed no evidence of an AGN. However, it is on the core of a compact galaxy, and has a clear $\gtrsim 100$ day rise in both z_{850} and i_{775}. While it could possibly be a very peculiar SN with a long rise time, what is important for this analysis is that it is clearly not a SN Ia.

4.2.3 Supernovae

After removing 17 image artifacts and 14 AGN, 29 candidates remain (listed in Table 4.2). One of these is the peculiar transient SN SCP06F6 which, as noted above, is clearly not a SN Ia. Note that Table 4.2 contains 10 fewer candidates than the list presented by Dawson et al. (2009). This is unsurprising; here we have intentionally used a stricter selection than in the original search, the source for the Dawson et al. (2009) sample. Still, after finalizing our selection method we checked that there were no unexpected discrepancies. Five of the Dawson et al. (2009) candidates (SCP06B4, SCP06U2, SCP06X18, SCP06Q31, SCP06T1) fell just below either the detection or signal-to-noise thresholds in

Table 4.2. Candidates classified as supernovae

ID	Nickname	R.A. (J2000)	Decl. (J2000)	z	Type	Conf.	How?
Cluster Members							
SCP06C1	Midge	$12^h\,29^m\,33^s.012$	$+01°\,51'\,36''.67$	0.98	Ia	secure	a,c
SCP05D0	Frida	$02^h\,21^m\,42^s.066$	$-03°\,21'\,53''.12$	1.014	Ia	secure	a,b,c
SCP06F12	Caleb	$14^h\,32^m\,28^s.748$	$+33°\,32'\,10''.05$	1.11	Ia	probable	c
SCP06H5	Emma	$14^h\,34^m\,30^s.139$	$+34°\,26'\,57''.29$	1.231	Ia	secure	b,c
SCP06K18	Alexander	$14^h\,38^m\,10^s.663$	$+34°\,12'\,47''.19$	1.412	Ia	probable	b
SCP06K0	Tomo	$14^h\,38^m\,08^s.366$	$+34°\,14'\,18''.08$	1.416	Ia	secure	b,c
SCP06R12	Jennie	$02^h\,23^m\,00^s.082$	$-04°\,36'\,03''.04$	1.212	Ia	secure	b,c
SCP06U4	Julia	$23^h\,45^m\,29^s.429$	$-36°\,32'\,45''.73$	1.05	Ia	secure	a,c
Cluster Membership Uncertain							
SCP06E12	Ashley	$14^h\,15^m\,08^s.141$	$+36°\,12'\,42''.94$	...	Ia	plausible	c
SCP06N32	...	$02^h\,20^m\,52^s.368$	$-03°\,34'\,13''.32$	...	CC	plausible	c
Not Cluster Members							
SCP06A4	Aki	$22^h\,16^m\,01^s.077$	$-17°\,37'\,22''.09$	1.193	Ia	probable	c
SCP06B3	Isabella	$22^h\,05^m\,50^s.402$	$-01°\,59'\,13''.34$	0.743	CC	probable	c
SCP06C0	Noa	$12^h\,29^m\,25^s.654$	$+01°\,50'\,56''.58$	1.092	Ia	secure	b,c
SCP06C7	...	$12^h\,29^m\,36^s.517$	$+01°\,52'\,31''.47$	0.61	CC	probable	c
SCP05D6	Maggie	$02^h\,21^m\,46^s.484$	$-03°\,22'\,56''.18$	1.314	Ia	secure	b,c
SCP06F6	...	$14^h\,32^m\,27^s.394$	$+33°\,32'\,24''.83$	1.189	non-Ia	secure	a
SCP06F8	Ayako	$14^h\,32^m\,24^s.525$	$+33°\,33'\,50''.75$	0.789	CC	probable	c
SCP06G3	Brian	$14^h\,29^m\,28^s.430$	$+34°\,37'\,23''.13$	0.962	Ia	plausible	c
SCP06G4	Shaya	$14^h\,29^m\,18^s.743$	$+34°\,38'\,37''.38$	1.35	Ia	secure	a,b,c
SCP06H3	Elizabeth	$14^h\,34^m\,28^s.879$	$+34°\,27'\,26''.61$	0.85	Ia	secure	a,c
SCP06L21	...	$14^h\,33^m\,58^s.990$	$+33°\,25'\,04''.21$	...	CC	plausible	c
SCP06M50	...	$16^h\,04^m\,25^s.300$	$+43°\,04'\,51''.85$	...	...	...	...
SCP05N10	Tobias	$02^h\,20^m\,52^s.878$	$-03°\,33'\,40''.20$	0.203	CC	plausible	c
SCP06N33	Naima	$02^h\,20^m\,57^s.699$	$-03°\,33'\,23''.97$	1.188	Ia	probable	c
SCP05P1	Gabe	$03^h\,37^m\,50^s.352$	$-28°\,43'\,02''.66$	0.926	Ia	probable	c
SCP05P9	Lauren	$03^h\,37^m\,44^s.512$	$-28°\,43'\,54''.58$	0.821	Ia	secure	a,c
SCP06U7	Ingvar	$23^h\,45^m\,33^s.867$	$-36°\,32'\,43''.48$	0.892	CC	probable	c
SCP06X26	Joe	$09^h\,10^m\,37^s.889$	$+54°\,22'\,29''.07$	1.44	Ia	plausible	c
SCP06Z5	Adrian	$22^h\,35^m\,24^s.966$	$-25°\,57'\,09''.61$	0.623	Ia	secure	a,c

Note. — "How?" indicates how the type is determined. (a) Spectroscopic confirmation. (b) Host is morphologically early-type, with no signs of recent star formation. (c) Light curve shape, color, magnitude consistent with type. We do not assign a type for SCP06M50 because there is significant uncertainty that the candidate is a SN at all.

our selection. These were found in the original search because detection thresholds were set slightly lower, and because the images were sometimes searched in several different ways. For example, in the original search SCP06B4 was only found by searching an i_{775} subtraction. Two Dawson et al. (2009) candidates (SCP05D55, SCP06Z52) were found too far on the decline and failed the light curve requirements (§4.1.2). Three Dawson et al. (2009) candidates (SCP06X27, SCP06Z13, SCP06Z53) were found while searching in "follow-up" visits, which were not searched here. SCP06U6 passed all requirements, but is classified here as an AGN, as noted above. With the exception of SCP06U6, all of these candidates are likely to be supernovae (mostly core collapse). However, the types of candidates that did not pass our requirements are not of concern for this analysis. Finally, SCP06M50 was not reported in Dawson et al. (2009), but is classified here as a SN, although with great uncertainty (discussed in detail in §4.2.4).

Thanks to the extensive ground-based spectroscopic follow-up campaign, we were able to obtain spectroscopic redshifts for 25 of the 29 SNe. The redshift reported in Table 4.2 is derived from the SN host galaxy for all but one candidate (SCP06C1) where the redshift is from the SN spectrum itself. Of the 25 candidates with redshifts, eight are in clusters and 17 are in the field. Note that this high spectroscopic completeness is particularly important for determining the cluster or non-cluster status of each SN, which directly affects the determination of the cluster SN Ia rate. The possible cluster memberships of the four candidates lacking redshifts are discussed below.

We determine the type of each of the 29 supernovae using a combination of methods in order to take into account all available information for each supernova. This includes (a) spectroscopic confirmation, (b) the host galaxy environment, and (c) the SN light curve. To qualify the confidence of each supernova's type, we rank the type as "secure," "probable," or "plausible":

Secure SN Ia Has spectroscopic confirmation or *both* of the following: (1) an early-type host galaxy with no recent star formation and (2) a light curve with shape, color and magnitude consistent with SNe Ia and inconsistent with other types.

Probable SN Ia Fulfills either the host galaxy requirement or the light curve requirement, but not both.

Plausible SN Ia The light curve is indicative of a SN Ia, but there is not enough data to rule out other types.

Secure SN CC Has spectroscopic confirmation (note that there are no such candidates in this sample).

Probable SN CC The light curve is consistent with a core-collapse SN and inconsistent with a SN Ia.

Plausible SN CC Has a light curve indicative of a core-collapse SN, but not inconsistent with a SN Ia.

This ranking system is largely comparable to the "gold," "silver," "bronze" ranking system of Strolger et al. (2004), except that we do not use their "UV deficit" criterion. This is because our data do not include the bluer F606W filter, and because SNe Ia and CC are only distinct in UV flux for a relatively small window early in the light curve. Below, we discuss in detail the three typing methods used.

(a) **Spectroscopic confirmation:** During the survey, seven candidates were spectroscopically confirmed as SNe Ia (Dawson et al. 2009; Morokuma et al. 2010). These seven (three of which are in clusters) are designated with an "a" in the "typing" column of Table 4.2. All seven candidates have a light curve shape, absolute magnitude and color consistent with a SN Ia. Although the spectroscopic typing by itself has some degree of uncertainty, the corroborating evidence from the light curve makes these "secure" SNe Ia.

(b) **Early-type host galaxy:** The progenitors of core-collapse SNe are massive stars ($> 8M_\odot$) with main sequence lifetimes of < 40 Myr. Thus, core-collapse SNe only occur in galaxies with recent star formation. Early-type galaxies, having typically long ceased star formation, overwhelmingly host Type Ia SNe (e.g., Cappellaro et al. 1999; Hamuy et al. 2000). In fact, in an extensive literature survey of core-collapse SNe reported in early-type hosts, Hakobyan et al. (2008) found that only three core-collapse SNe have been recorded in early-type hosts, and that the three host galaxies in question had either undergone a recent merger or were actively interacting. In all three cases there are independent indicators of recent star formation. Therefore, in the cases where the host galaxy morphology, photometric color, and spectrum all indicate an early-type galaxy with no signs of recent star formation or interaction, we can be extremely confident that the SN type is Ia. These cases are designated by a "b" in the "typing" column of Table 4.2. We emphasize that in all of these cases, spectroscopy reveals no signs of recent star formation and there are no visual or morphological signs of interaction. (See Meyers et al. 2011, for detailed studies of these SN host galaxy properties.)

(c) **Light curve:** SNe Ia can be distinguished from most common types of SNe CC by some combination of light curve shape, color, and absolute magnitude. We compare the light curve of each candidate to template light curves for SN Ia and various SN CC subtypes to test if the candidate could be a SN Ia or a SN CC. For candidates lacking both spectroscopic confirmation and an elliptical host galaxy, if there is sufficient light curve data to rule out all SN CC subtypes, the candidate is considered a "probable" SN Ia. If SN Ia can be ruled out, it is considered a "probable" SN CC. If neither SN Ia nor SN CC can be ruled out, the candidate is considered a "plausible" SN Ia or SN CC based on how typical the candidate's absolute magnitude and/or color would be of each type. This approach can be viewed as a qualitative version of the pseudo-Bayesian light curve typing approaches of, e.g., Kuznetsova & Connolly (2007); Kuznetsova et al. (2008); Poznanski et al. (2007a,b). SNe classified as "probable" here would likely have a Bayesian posterior probability approaching 1, while "plausible" SNe would have an intermediate probability (likely between 0.5 and 1.0). We consciously avoid the full Bayesian typing approach because it can obscure large uncertainties in the priors such as luminosity distributions, relative rates, light curve shapes, and SN subtype fractions. Also, the majority of our candidates have more

available light curve information than those of **Kuznetsova et al.** (2008) and **Poznanski et al.** (2007b), making a calculation of precise classification uncertainty less necessary. In general, classification uncertainty from light curve fitting is not a concern for the cluster rate calculation as most cluster-member candidates are securely typed using methods (a) and/or (b), above.

For each candidate we fit template light curves for SN Ia, Ibc, II-P, II-L, and IIn. We use absolute magnitude and color as a discriminant by limiting the allowed fit ranges according to the known distributions for each subtype. For SN Ia we start with the spectral time series template of **Hsiao et al.** (2007), while for the core-collapse types we use templates of **Nugent et al.** (2002)[1]. Each spectral time series is redshifted to the candidate redshift and warped according to the desired color. Observer-frame template light curves are then generated by synthetic photometry in the i_{775} and z_{850} filters. The magnitude, color, date of maximum light, and galaxy flux in i_{775} and z_{850} are allowed to vary to fit the light curve data. For the SN Ia template, the linear timescale or "stretch" (e.g., **Perlmutter et al.** 1997; **Guy et al.** 2005) is also allowed to vary within the range $0.6 < s < 1.3$. We constrain the absolute magnitude for each subtype to the range observed by **Li et al.** (2011); Our allowed range fully encompasses their observed luminosity functions (uncorrected for extinction) for a magnitude-limited survey for each subtype. We correct from their assumed value of $H_0 = 73$ km s^{-1} Mpc^{-1} to our assumed value of $H_0 = 70$ km s^{-1} Mpc^{-1} and K-correct from R to B band. To avoid placing too strict of an upper limit on SN CC brightness, we use the bluest maximum-light spectrum available when K-correcting (e.g., for SN Ibc we use a bluer spectrum than that of **Nugent et al.** (2002), as bluer SNe Ibc have been observed). The resulting allowed M_B range for each subtype is shown in Table 4.3. Note that the range for Ibc does not include ultra-luminous SNe Ic (such as those in the luminosity functions of **Richardson et al.** (2002)) as none were discovered by **Li et al.** (2011). While such SNe can mimic a SN Ia photometrically, the **Li et al.** (2011) results indicate that they are intrinsically rare, and even **Richardson et al.** (2002) show that they make up at most ∼20% of all SNe Ibc. Still, we keep in mind that even candidates compatible only with our SN Ia template and incompatible with SN CC templates may in fact be ultra-luminous SNe Ic, though the probability is low. This is why any candidate typed based on light curve alone has a confidence of at most "probable," rather than "secure." The allowed ranges of "extinction," $E(B-V)$, are also shown in Table 4.3. For SN Ia, $E(B-V)$ is the difference in $B - V$ color from the **Hsiao et al.** (2007) template. As the observed distribution of SNe includes SNe bluer than this template, SNe Ia as blue as $E(B-V) = -0.2$ are allowed. Given an $E(B-V)$, the spectral template is warped according to the SALT color law (**Guy et al.** 2005), with an effective $R_B = 2.28$ (**Kowalski et al.** 2008). For SN CC templates, extinction as low as $E(B-V) = -0.1$ is allowed to reflect the possibility of SNe that are intrinsically bluer than the **Nugent et al.** (2002) templates. Templates are then warped using a **Cardelli et al.** (1989) law with $R_B = 4.1$. Extinctions are limited to $E(B-V) < 0.5$ (implying an extinction of $A_B \sim 2$ magnitudes for SNe CC).

---

[1] See http://supernova.lbl.gov/~nugent/nugent_templates.html.

Table 4.3. SN light curve template parameter ranges for typing

SN type	Template	Observed M_B	$E(B-V)$	s
Ia	Hsiao	$-17.5 - -20.1$	$-0.2 - 0.6$	$0.6 - 1.3$
Ibc	Nugent	$-15.5 - -18.5$	$-0.1 - 0.5$	1.0
II-L	Nugent	$-16.0 - -19.0$	$-0.1 - 0.5$	1.0
II-P	Nugent	$-15.5 - -18.0$	$-0.1 - 0.5$	1.0
IIn	Nugent	$-15.5 - -19.1$	$-0.1 - 0.5$	1.0

The light curve template with the largest χ^2 P-value is generally taken as the type. We also evaluate each fit by eye to check that the best-fit template adequately describes the light curve. Figure 4.4 shows the best-fit template for each candidate. For candidates typed on the basis of spectroscopic confirmation or an elliptical host galaxy only the SN Ia template is shown. For candidates typed on the basis of the light curve alone, we show both the best-fit SN Ia and best-fit SN CC templates for comparison. The confidence in the best-fit template is either "probable" or "plausible" depending on how well other templates fit: If the next-best fit has a P-value that is smaller than $10^{-3} \times P_{\text{best}}$, the best-fit template is considered the only acceptable fit and the confidence is "probable." If the next-best fit has a P-value larger than $10^{-3} \times P_{\text{best}}$ the confidence is "plausible." Note that the photometry used here is simple aperture photometry with fixed aperture corrections. For SN Ia cosmology we use color-dependent aperture corrections, as described in Suzuki et al. (2011). Finally, Figure 4.5 shows the distribution of the fitted absolute magnitude and redshift of SN candidates, along with the expected distributions based on our efficiency simulations (presented later). This demonstrates that the candidates' magnitudes are consistent with what we expect to find based on the survey efficiencies. However, this should not be seen as additional evidence that the SN typing is correct, as absolute magnitude information has already been used in determining the type.

4.2.4 Comments on Individual SN Light Curves

Here we comment in greater detail on a selection of individual candidates, particularly those with the greatest uncertainty in typing. For each candidate, see the corresponding panel of Figure 4.4 for an illustration of the candidate host galaxy and light curve.

SN SCP06E12. We were unable to obtain a host galaxy redshift due to the faintness of the host. The color of the host galaxy is consistent with the cluster red sequence. The candidate light curve is consistent with a SN Ia at the cluster redshift of $z = 1.03$, but is also consistent with SN II-L at $z = 1.03$. Different SN types provide an acceptable fit over a fairly wide range of redshifts. As the SN Ia template provides a good fit with typical parameters, we classify the candidate as a "plausible" SN Ia. However, there is considerable uncertainty due to the uncertain redshift.

SN SCP06N32 also lacks a host galaxy redshift. If the cluster redshift of $z = 1.03$ is assumed, the candidate light curve is best fit by a SN Ibc template. A SN Ia template also yields an acceptable fit, but requires an unusually red color of $E(B - V) \sim 0.6$. Given the best-fit s and M_B values, the candidate would have an unusually large Hubble diagram residual of approximately -0.8 magnitudes. If the redshift is allowed to float, a SN Ia template with more typical parameters provides an acceptable fit at $z = 1.3$. A SN Ibc template still provides a better fit, with the best fit redshift being $z \sim 0.9$. As SN Ibc
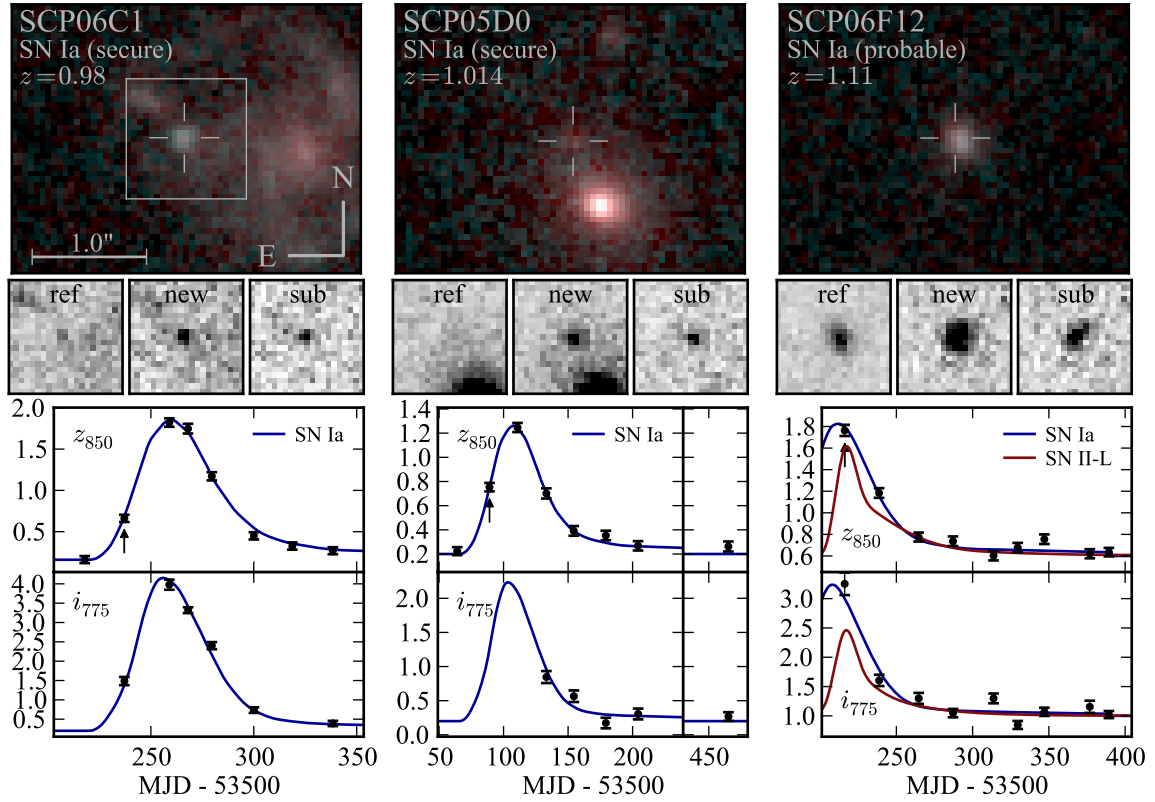
Figure 4.4. Images and light curves of the 29 candidates classified as supernovae. For each candidate, the *top panel* shows the two-color stacked image (i_{775} and z_{850}) of the supernova host galaxy, with the SN position indicated. The *three smaller panels* below the stacked image show the reference, new, and subtracted images for the discovery visit. The *bottom panel* shows the light curve at the SN position (including host galaxy light) in the z_{850} (*top*) and i_{775} (*bottom*) bands. The y axes have units of counts per second in a 3 pixel radius aperture. The effective zeropoints are 23.94 and 25.02 for z_{850} and i_{775}, respectively. The discovery visit is indicated with an arrow in the z_{850} plot. The best-fit SN Ia template is shown in blue. For cases where the type is SN Ia based on spectroscopic confirmation or host galaxy environment, only the best-fit SN Ia template is shown, to demonstrate the consistency of the light curve with the designation. For cases where the type is based only on the light curve fit, the best-fit core collapse SN template is shown in red. Note that the photometry used here is simple aperture photometry with fixed aperture corrections. For SN Ia cosmology we use color-dependent aperture corrections, as described in **Suzuki et al. (2011)**. [*continued on next 5 pages.*]

SCP06N32
SN CC (plausible)

SCP06A4
SN Ia (probable)
z=1.193

SCP06B3
SN CC (probable)
z=0.743

SCP06C0
SN Ia (secure)
z=1.092

SCP06C7
SN CC (probable)
z=0.61

SCP05D6
SN Ia (secure)
z=1.314
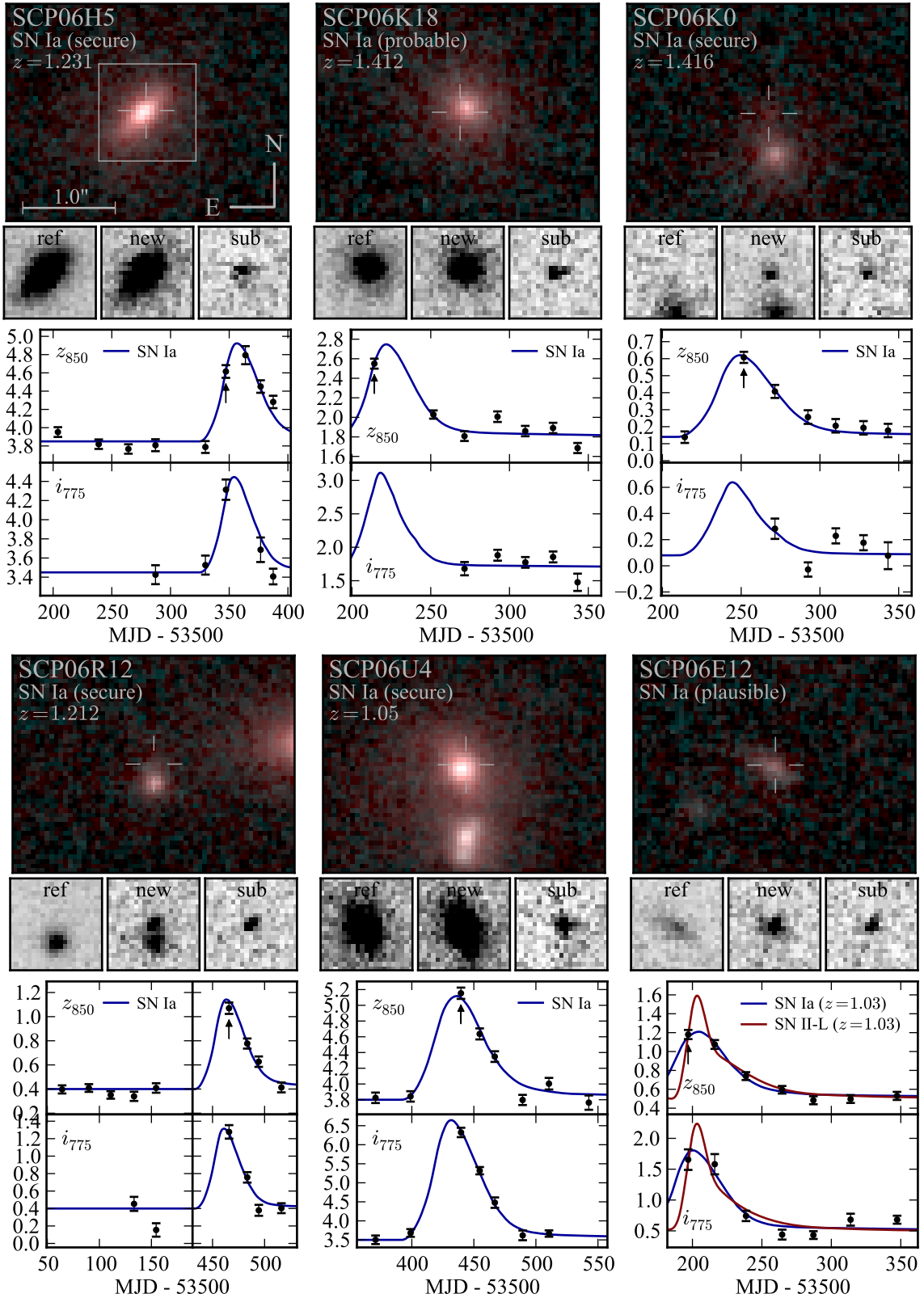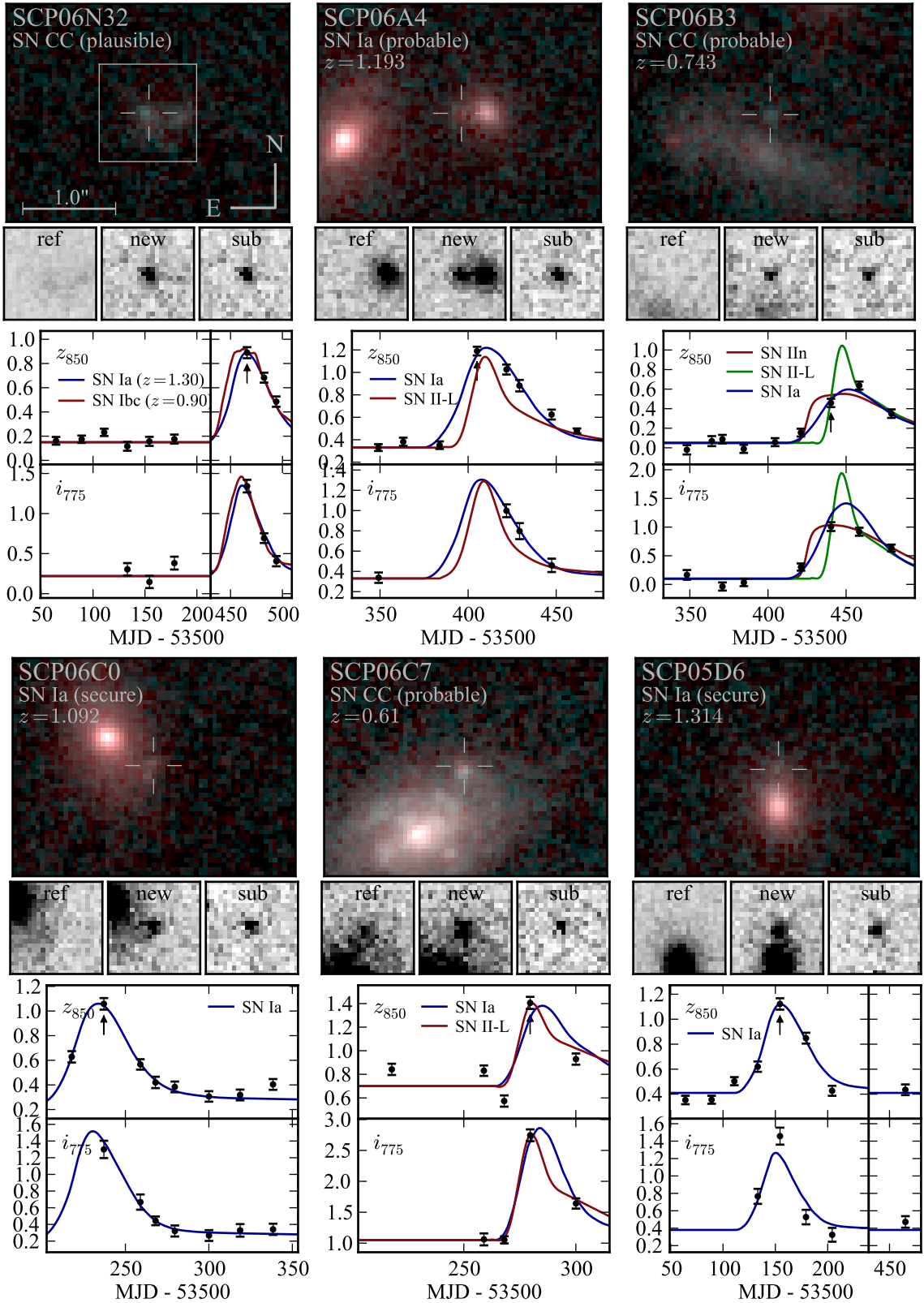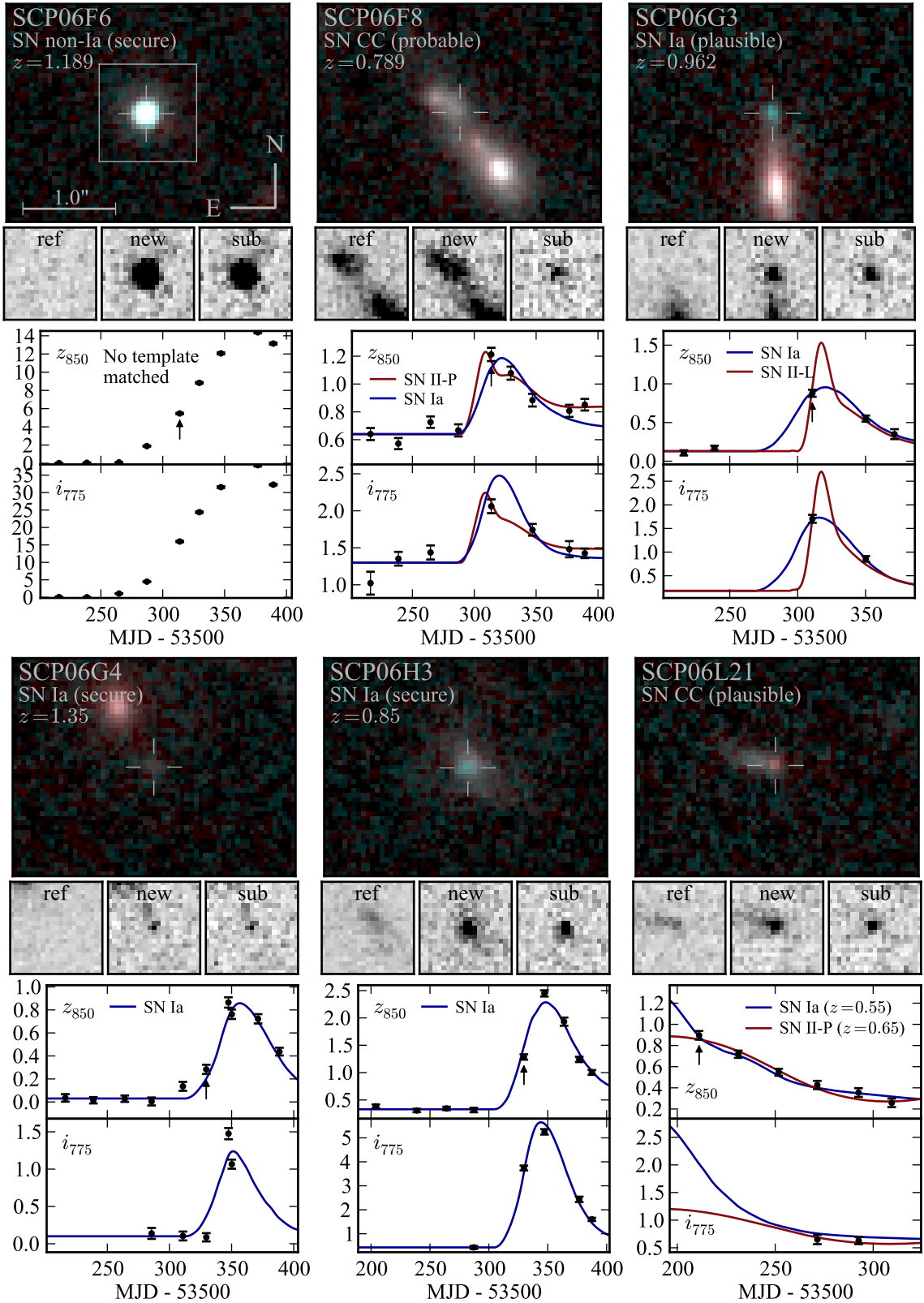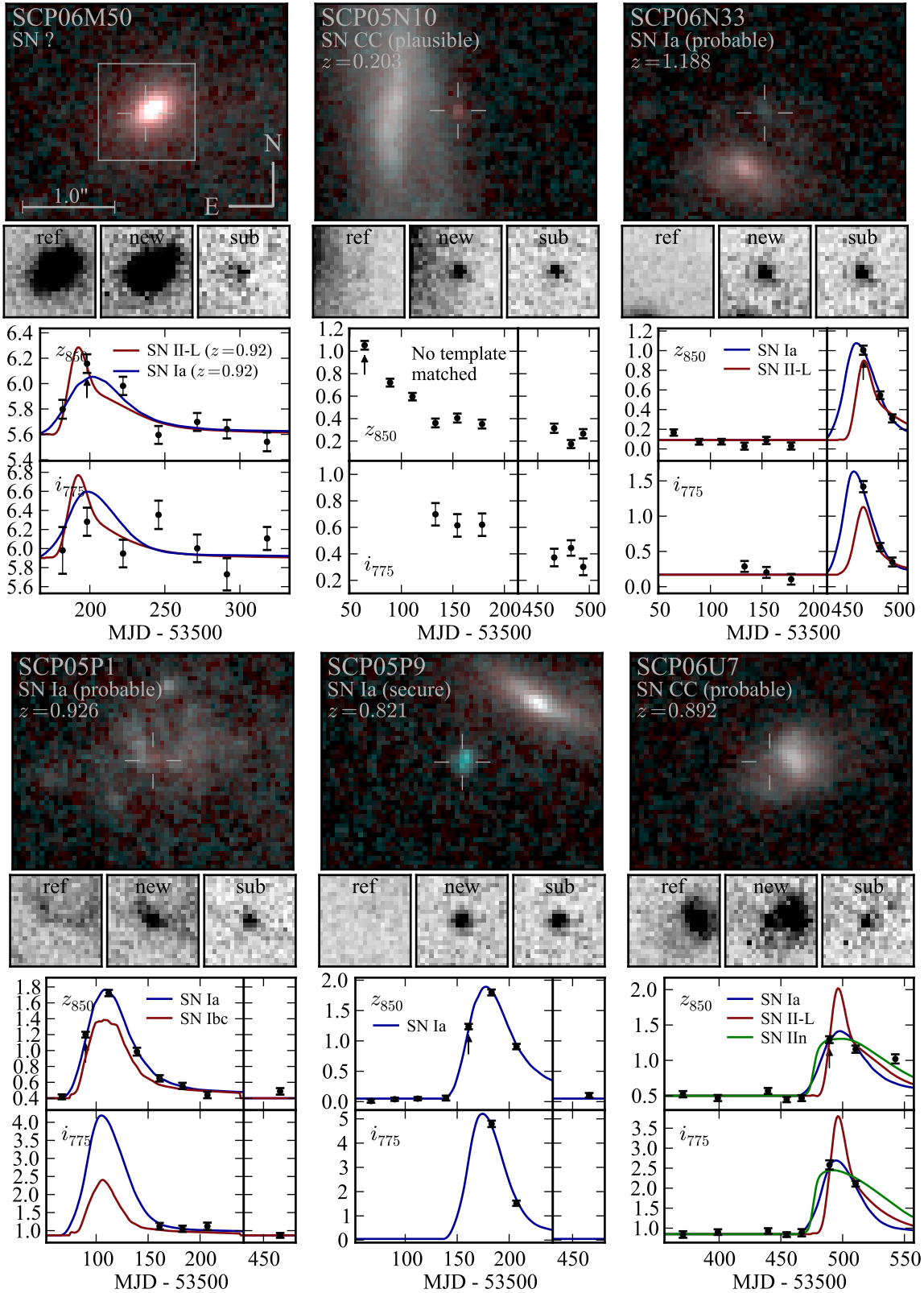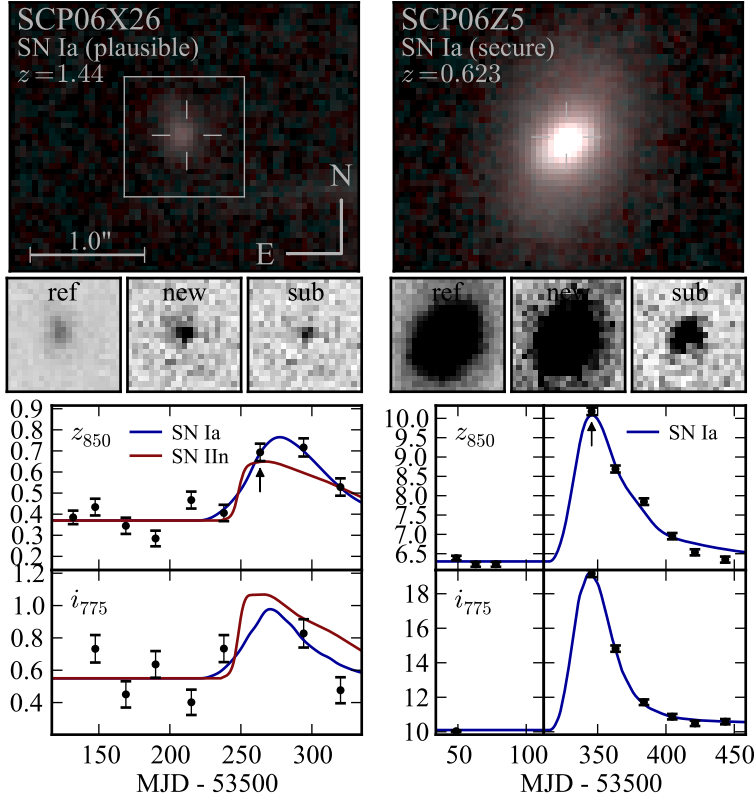
provides a better fit in both cases, we classify this as a "plausible" SN CC. However, there is considerable uncertainty in both the type and cluster membership of this candidate.

SN SCP06A4. We note that this candidate was observed spectroscopically, as reported in Dawson09. While the spectrum was consistent with a SN Ia, there was not enough evidence to conclusively assign a type. The host galaxy is morphologically and photometrically consistent with an early-type galaxy, but there is detected [OII], a possible indication of star formation. We therefore rely on light curve typing for this candidate, assigning a confidence of "probable" rather than "secure."

SN SCP06G3 has only sparse light curve coverage. The best fit template is a SN Ia with $s = 1.3$, $E(B - V) = 0.3$ and $M_B = -18.5$, although these parameters are poorly constrained. A large stretch and red color would not be surprising given the spiral nature of the host galaxy. It is also consistent with a II-L template, although the best fit color is unusually blue: $E(B - V) = -0.1$. Given that SN Ia yields more "typical" fit parameters and that, at $z \sim 1$ a detected SN is more likely to be Type Ia than II, we classify this as a "plausible" Type Ia, with considerable uncertainty in the type.

SN SCP06L21 lacks a spectroscopic redshift, but has a distinct slowly-declining light curve that rules out a $z > 0.6$ SN Ia light curve. Even the best-fit Ia template at $z = 0.55$, shown in Fig. 4.4), is unusually dim ($M_B \approx -17.5$), making it unlikely that the candidate is a lower-redshift SN Ia. The light curve is better fit by a SN II-P template (with the best-fit
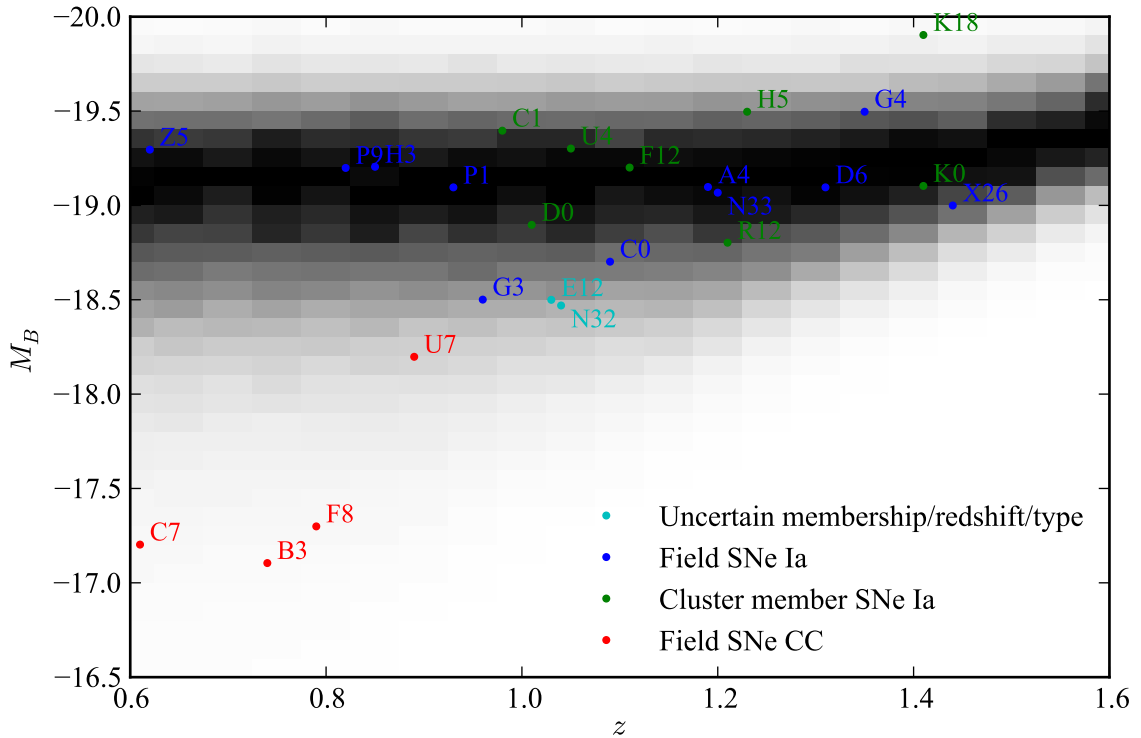
Figure 4.5. Distribution of SNe in absolute magnitude and redshift, based on rough light curve fits. The shading represents the expected magnitude distribution of field SNe Ia (similar for cluster SNe Ia) in the survey in each redshift bin of $\Delta z = 0.05$, based on the simulations in §6.3. The candidates designated as core-collapse are all significantly dimmer than expected for SNe Ia, while the distribution of SN Ia candidates follows the expected distribution closely. Note that the light curve of SN SCP06K18 is very poorly constrained: $M_B \gtrsim -19.5$ is also consistent with the light curve data.

redshift being $z = 0.65$). We therefore classify the candidate as a "probable" SN CC.

    SN SCP06M50 is the most questionable "SN" candidate, having no obvious i_{775} counterpart to the increase seen in z_{850}. It may in fact be an image artifact or AGN. However, it appears to be off the core of the galaxy by ~2 pixels (making AGN a less likely explanation), and shows an increase in z_{850} flux in two consecutive visits, with no obvious cosmic rays or hot pixels (making an image artifact less likely as well). The galaxy is likely to be a cluster member: its color and magnitude put it on the cluster red sequence, it is morphologically early-type, and it is only $19''$ from the cluster center. Under the assumption that the candidate is a supernova and at the cluster redshift of $z = 0.92$, no template provides a good fit due to the lack of an i_{775} detection and the constraints on $E(B - V)$. In particular, a SN Ia template would require $E(B - V) > 0.6$. (The best-fit template shown in Fig. 4.4 is with $E(B - V) = 0.6$.) If the redshift is allowed to float, it is possible to obtain a good fit at higher redshift ($z \sim 1.3$), but still with $E(B - V) \gtrsim 0.4$, regardless of the template type. Given the color and early-type morphology of the host galaxy, it is unlikely to con-

tain much dust. There is thus no consistent picture of this candidate as a SN, and we do not assign a type. However, note that the candidate is unlikely to be a cluster SN Ia.

SN SCP05N10 is the lowest-redshift SN candidate in our sample at $z = 0.203$. Its light curve shape is inconsistent with a SN Ia occurring well before the first observation, and its luminosity is too low for a SN Ia with maximum only slightly before the first observation. Therefore, we call this a "probable" SN CC. For all SN types, the best fit requires maximum light to occur well before the first observation, making all fits poorly constrained.

SN SCP06X26 has a tentative redshift of $z = 1.44$, derived from a possible [OII] emission line in its host galaxy. Given this redshift, a Ia template provides an acceptable fit, consistent with a typical SN Ia luminosity and color. However, we consider this a "plausible," rather than "probable," SN Ia, given the uncertain redshift and low signal-to-noise of the light curve data.

CHAPTER 5

Cluster Rate

5.1 Overview of Calculation

With the systematically selected SN sample from the previous chapter, we are now in a position to calculate SN rates. The cluster SN Ia rate is given by

$$\mathcal{R} = \frac{N_{\text{SN Ia}}}{\sum_j T_j L_j},$$ (5.1)

where $N_{\text{SN Ia}}$ is the total number of SNe Ia observed in clusters in the survey, and the denominator is the total effective time-luminosity for which the survey is sensitive to SNe Ia in clusters. L_j is the luminosity of cluster j visible to the survey in a given band. T_j is the "effective visibility time" (also known as the "control time") for cluster j. This is the effective time for which the survey is sensitive to detecting a SN Ia, calculated by integrating the probability of detecting a SN Ia as a function of time over the span of the survey. It depends on the redshift of the SN Ia to be detected and the dates and depths of the survey observations. As each cluster has a different redshift and different observations, the control time is determined separately for each cluster. To calculate a rate per stellar mass, L_j is replaced by M_j.

Equation (5.1) is for the case where the entire observed area for each cluster is observed uniformly, yielding a control time T that applies to the entire area. In practice, different areas of each cluster may have different observation dates and/or depths, resulting in a control time that varies with position. This is particularly true for this survey, due to the rotation of the observed field between visits and the gap between ACS chips. Therefore, we calculate the control time as a function of position in each observed field, $T_j(x, y)$. As the cluster luminosity is also a function of position, we weight the control time at each position by the luminosity at that position. In other words, we make the substitution

$$T_j L_j \Rightarrow \int_{x,y} T_j(x, y) L_j(x, y).$$ (5.2)

In §5.2 we summarize the findings of the previous chapter for $N_{\text{SN Ia}}$. In §5.3 we calculate $T_j(x, y)$, and in §5.4 we calculate $L_j(x, y)$.

5.2 Summary of Cluster SN Candidates

In the previous chapter we addressed the type of all 29 candidates thought to be SNe. However only the cluster-member SNe Ia are of interest for this chapter. There are six "secure" cluster-member SNe Ia, and two "probable" SNe Ia, for a total of eight. In addition, SCP06E12 is a "plausible" SN Ia and may be a cluster member. Two other candidates, SCP06N32 and SCP06M50, cannot be definitively ruled out as cluster-member SNe Ia, but are quite unlikely for reasons outlined above. We take eight cluster SNe Ia as the most likely total. It is unlikely that *both* of the "probable" SNe Ia are in fact SNe CC. We therefore assign a classification error of $^{+0.0}_{-0.5}$ for each of these, resulting in a lower limit of seven cluster-member SNe Ia. There is a good chance that SCP06E12 is a cluster-member SN Ia, while there is only a small chance that SCP06N32 and SCP06M50 are either cluster SNe Ia. For these three candidates together, we assign a classification error of $^{+1}_{-0}$, for an upper limit of nine. Thus, 8 ± 1 is the total number of observed cluster SNe Ia, including classification uncertainty.

5.3 Effective Visibility Time

The effective visibility time T at a position (x, y) on the sky is given by

$$T(x, y) = \int_{t=-\infty}^{t=\infty} \eta^*(x, y, t)\epsilon(x, y, t)dt. \tag{5.3}$$

The integrand here is simply the probability for the survey and our selection method to detect (and keep) a SN Ia at the cluster redshift that explodes at time t, and position (x, y). This probability is split into the probability η^* of detecting the supernova and the probability ϵ that the supernova passes all "light curve" cuts. As each SN has multiple chances for detection, the total probability of detection η^* is a combination of the probabilities of detection in each observation. For example, if we have two search visits at position (x, y), $\eta^*(t)$ is given by

$$\eta^*(t) = \eta_1(t) + (1 - \eta_1(t))\eta_2(t), \tag{5.4}$$

where $\eta_i(t)$ is the probability of detecting a SN Ia exploding at time t in visit i. In other words, the total probability of finding the SN Ia exploding at time t is the probability of finding it in visit 1 plus the probability that it was *not* found in visit 1 times the probability of finding it in visit 2. This can be generalized to many search visits: The contribution of each additional visit to the total probability is the probability of not finding the SN in any previous visit times the probability of finding the SN in that visit.

In practice, we calculate $T(x, y)$ in two steps: First, we determine the probability η of detecting a new point source in a single image as a function of the point source magnitude. This is discussed in §5.3.1. Second, for each (x, y) position in the observed area we simulate a variety of SN Ia light curves at the cluster redshift occurring at various times

during the survey. By considering the dates of the observations made during the survey at that specific position, we calculate the brightness and significance each simulated SN Ia would have in each z_{850} and i_{775} image. We then use our calculation of η as a function of magnitude to convert the observed brightness into a probability of detecting the simulated SN in each observation. The light curve simulation is discussed in §5.3.2.

5.3.1 Detection Efficiency

Here we calculate the probability of detecting a new point source as a function of magnitude. We use a Monte Carlo simulation in which artificial point sources of various magnitudes are added to survey images. The images are then run through the same reduction and SN detection pipeline used in the search.

Because our search procedure uses information from individual exposures to reject cosmic rays, it is necessary to place the artificial point sources on these individual exposure images rather than on the combined image from each visit. This allows us to test both the efficiency of the MULTIDRIZZLE process and our CR rejection. We add the artificial point sources to the raw CCD images after bias subtraction and flat fielding. As these "_flt" images have not been re-sampled, they accurately represent the light on each CCD pixel.

As a model of the point spread function (PSF) on these images, we use the PSF library of Anderson & King (2006). For each of six ACS filters, this library represents the position-dependent PSF by a 9×10 array of fiducial PSFs across the two CCDs. Each fiducial PSF model is oversampled by a linear factor of 4, giving the model a pixel scale of $0''.0125$. As this library was derived on _flt images, it is directly applicable to these images.

The artificial point sources are placed on galaxies according to the distribution of light in each galaxy. Galaxies with $z_{850} < 20$ are not used, as these are only found at redshifts below the range of interest. Only one point source is placed on each galaxy to avoid detection complications from overlapping sources. Once a position on a galaxy is chosen, it is converted to a corresponding CCD chip position on each of the (typically four) individual exposure images taken for the visit. The oversampled fiducial PSF model for this position on the CCD is chosen from the PSF library and is re-sampled onto the CCD pixels. A random point source flux is drawn from the range of interest. The PSF model is adjusted to match this flux. It is normalized so that the encircled energy in a 3 pixel radius aperture in the combined image matches the value derived by Sirianni et al. (2005). A further adjustment to the flux is made to compensate for the variation in effective pixel area across the detector. (This variation is due to the ACS distortion and is on the order of 10 to 20%.) Poisson noise is added to each pixel in the PSF and the PSF is then added to the image. Images are passed through the same reduction and detection pipeline used in the search. Finally, the flagged candidates are compared to the input artificial point sources.

We parameterize the detection efficiency by the ratio of point source flux to sky noise. This is a good choice because, in most cases, the detection efficiency will depend only on the contrast between the point source and the sky noise. However, there is an additional dependence on the surface brightness at the location of the point source: point sources near
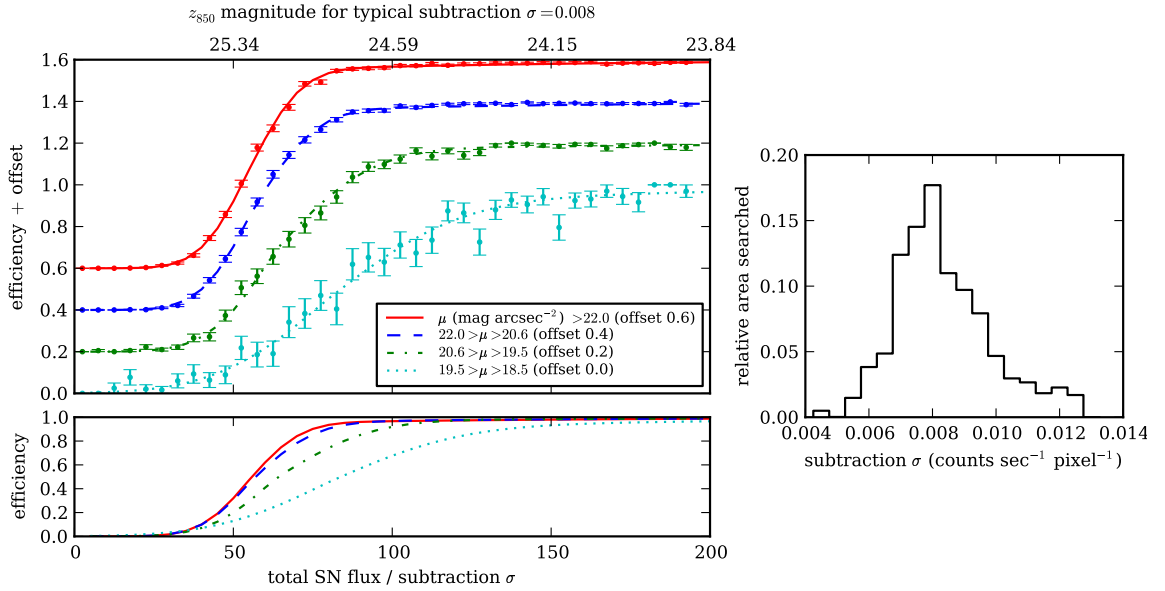
Figure 5.1. Point source detection efficiency in a single subtraction, as a function of the ratio of total point source flux to subtraction noise σ (counts sec^{-1} pixel^{-1}). The artificial point sources are split into four bins depending on the underlying galaxy surface brightness μ (mag arcsec^{-2}) at the point source position. The efficiency curve is calculated separately for each bin. In the *upper left panel*, the four bins are shown, offset for clarity. In the *lower left panel*, the fitted curves are reproduced without offset for comparison. Approximately 72,000 artificial point sources were used in total. The *right panel* shows the distribution of the noise level in the subtractions. The noise level differs by a factor of about two from the deepest to shallowest subtractions searched.

the core of galaxies will have a lower detection efficiency due to additional Poisson noise from the galaxy. For $0.6 < z < 1.5$ galaxies, we estimate that only $\sim 10\%$ of SNe will fall on regions where galaxy Poisson noise is greater than the sky noise (assuming SNe follow the galaxy light distribution). Still, we take this effect into account by splitting our sample of artificial point sources into four bins in underlying surface brightness. The detection efficiency is calculated separately in each bin (Fig. 5.1, top left panel). The first two bins, $\mu > 22.0$ and $22.0 > \mu > 20.6$ mag arcsec^{-2}, correspond to lower surface brightnesses where sky noise is dominant. As expected, their efficiency curves are very similar. In the third and fourth bins, corresponding to higher surface brightness, the Poisson noise from the galaxy dominates the sky noise, and the efficiency drops as a result.

For reference, the distribution of sky noise in the subtractions is shown in Figure 5.1 (right panel). Nearly all the searched area has a sky noise level between 0.006 and 0.012 counts sec^{-1} pixel^{-1}. For a typical value of 0.008, we show the corresponding point source z_{850} magnitude on the top axis of the left panel.

We find that the efficiency curve in each bin is well-described by the function

$$\eta(x) = \begin{cases} \frac{1}{2}(1 + ae^{-bx})[\mathrm{erf}((x - c)/d_1) + 1], & x < c \\ \frac{1}{2}(1 + ae^{-bx})[\mathrm{erf}((x - c)/d_2) + 1], & x \geq c \end{cases}, \tag{5.5}$$

where x is the ratio of point source flux to sky noise, and a, b, c, d_1 and d_2 are free parameters. An error function is the curve one would expect with a constant cut and Gaussian noise, but we find that two different scales (d_1 and d_2) in the error function, as well as an additional exponential term, are necessary to describe the slow rise to $\eta = 1$ at large x. This slow rise is due to rarer occurrences, such as cosmic rays coinciding with new point sources. The fitted functions for the four bins are plotted in the top left of Figure 5.1 and reproduced in the bottom left of the figure for comparison. We use these fitted functions to calculate the effective visibility time in the following section.

5.3.2 Simulated Lightcurves

We simulate SN Ia light curves with a distribution of shapes, colors and absolute magnitudes. We use the (original) SALT (Guy et al. 2005) prescription in which the diversity of SN Ia light curves is characterized as a two-parameter family with an additional intrinsic dispersion in luminosity. The two parameters are the linear timescale of the light curve ("stretch", s) and the $B - V$ color excess, c. For each simulated SN, s and c are randomly drawn from the distributions shown in Figure 5.2 (solid lines). The stretch distribution is based on the observed distribution in passive hosts (Fig. 5.2, left panel, grey histogram) in the first-year Supernova Legacy Survey (SNLS) sample (Sullivan et al. 2006). Similarly, the color distribution is based on the observed color distribution (Fig. 5.2, right panel, grey histogram) in the first-year SNLS sample (Astier et al. 2006). The absolute magnitude of each simulated SN is set to

$$M_B = -19.31 - \alpha(s - 1) + \beta c + I \tag{5.6}$$

where -19.31 is the magnitude of an $s = 1$, $c = 0$ SN Ia in our assumed cosmology (Astier et al. 2006), $\alpha = 1.24$, $\beta = 2.28$ (Kowalski et al. 2008), and I is an added "intrinsic dispersion", randomly drawn from a Gaussian distribution centered at zero with $\sigma = 0.15$ mag.

We have chosen distributions that represent as accurately as possible the full distribution of SNe Ia occurring in reality. However, note that the control time is not actually very sensitive to the assumed distributions. This is because, for the majority of cluster redshifts in the survey, the detection efficiency is close to 100% during the time of the survey. Supernovae would thus have to be significantly less luminous in order to change the detection efficiency significantly. In the following section §5.3.3 we quantify the effect on the control time arising from varying the assumed SN Ia properties and show that they are sub-dominant compared to the Poisson error in the number of SNe observed. All sources of systematic errors are also summarized in §5.5.2.

To generate the simulated light curves in the observed bands, we use the Hsiao et al. (2007) SN Ia spectral time series template. For each simulated SN, the spectral time series is warped to match the selected color c and redshifted to the cluster rest-frame. Light curves are generated in the observed i_{775} and z_{850} filters using synthetic photometry, and the time axis is scaled according to the chosen value of s.
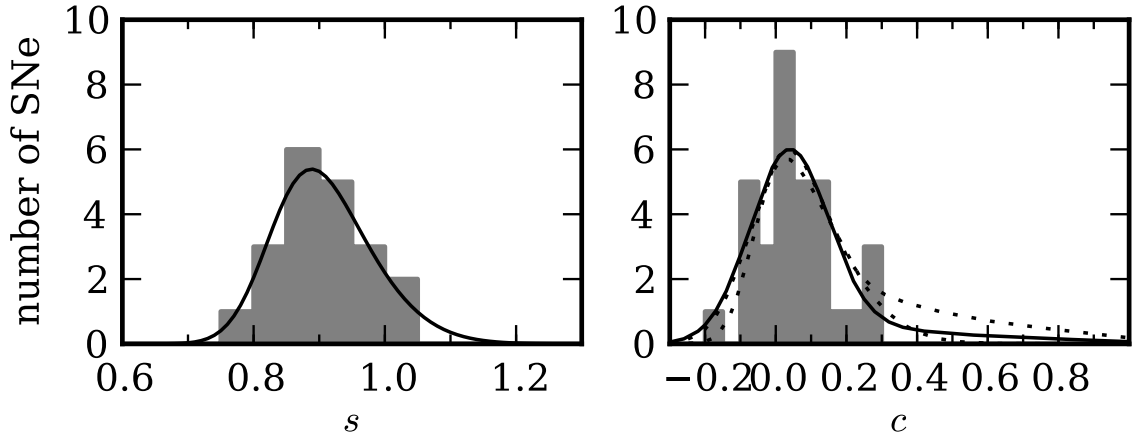
Figure 5.2. *Left panel:* stretch distribution used for simulated SNe (solid line) and the stretch distribution of first-year SNLS $z < 0.75$ SNe in passive hosts (Sullivan et al. 2006) (grey histogram). Note that the distribution is not changed significantly by cutting the sample at $z < 0.6$. Therefore we do not expect the sample to be significantly Malmquist biased. *Right panel:* color distribution of the first-year SNLS $z < 0.6$ SNe (Astier et al. 2006) (grey histogram) and the color distribution used for simulated SNe (solid line). The dotted lines show alternative color distributions used to assess the possible systematic error due to varying amounts of SNe being affected by dust.

For each cluster, we calculate $T(x, y)$ in bins of 50×50 pixels ($2''.5 \times 2''.5$). In each bin, we simulate 100 SN light curves at random positions within the bin. For each simulated SN light curve, we shift the light curve in time across the entire range of observations, starting with maximum light occurring 50 days before the first observation and ending with maximum light occurring 50 days after the last observation. For each step in time we get the z_{850} and i_{775} magnitude of the SN at every date of observation. From the sky noise maps, we know the noise at the position of the simulated SN in every image. Using the curves in Figure 5.1, we convert the SN flux-to-noise ratio to the probability of the SN being detected in each z_{850} exposure. (Each simulated SN is also assigned a host galaxy surface brightness chosen from a distribution, in addition to the randomly selected s, c and I parameters; we use the Fig. 5.1 curve that corresponds to this surface brightness.) At the same time, we calculate the probability that the SN passes our light curve cuts (using both z_{850} and i_{775} simulated magnitudes). Multiplying these two probabilities gives the total probability of the simulated SN being included in the sample if it peaks at the given date. Integrating the probability over time (the entire range of dates) gives the control time for each simulated SN. We take the average control time of the 100 SNe as the value for the given bin. The resulting control time map, $T(x, y)$, therefore has a resolution of $2''.5 \times 2''.5$. $T(x, y)$ is shown for two example clusters in Figure 5.3.
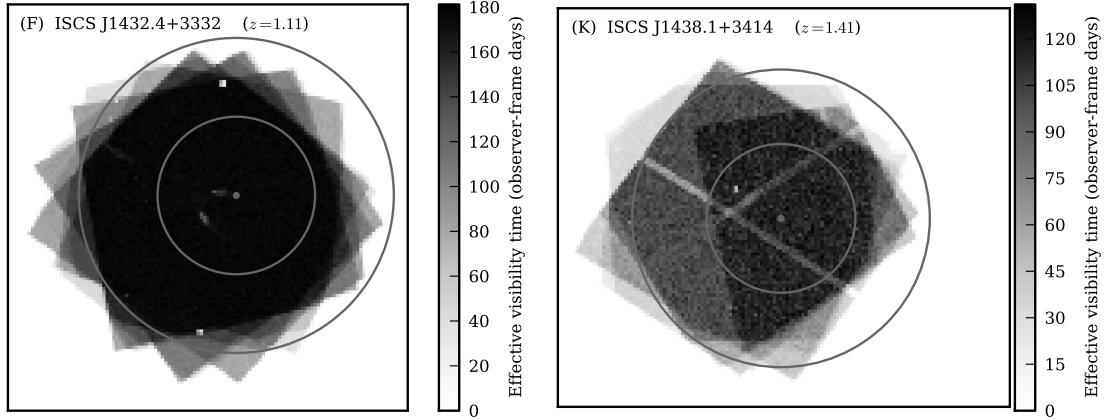
Figure 5.3. Example maps of effective visibility time for clusters ISCS J1432.4+3332 (F) and ISCS J1438.1+3414 (K). The dot denotes the cluster center and the inner and outer circles represent 0.5 Mpc and 1.0 Mpc radius, respectively. The "noise" in these maps is due to the finite number (100) of SNe simulated at each position. At lower redshift nearly all simulated SNe are recovered at each position, whereas at higher redshift a sizable fraction of simulated SNe are missed, resulting in a higher "noise" level.

5.3.3 Effect of Varying SN Properties

If the real distributions of SN Ia properties differs significantly from those assumed in our simulation, the $T(x,y)$ maps we have derived could misrepresent the true efficiency of the survey. Above we argued that the effect is likely to be small because the detection efficiency is close to 100% for most of the survey. Here we quantify the size of the possible effect on the control time by varying the assumed distributions.

To first order, changing the assumed distributions of s or c or changing the assumed spectral time series will affect the detection efficiency by increasing or decreasing the luminosity of the simulated SN. To jointly capture these effects, we shift the absolute magnitude of the simulated SNe Ia by $^{+0.2}_{-0.2}$ mag and recalculate the control times. To first order, this is equivalent to shifting the s distribution by $\Delta s = 0.2/\alpha \sim 0.16$ or shifting the c distribution by $\Delta c = 0.2/\beta \sim 0.09$. A -0.2 mag shift in absolute magnitude increases the control time, decreasing the inferred SN Ia rate by 6%. A $+0.2$ mag shift decreases the control time, increasing the SN Ia rate by 8%. These effects are sub-dominant compared to the Poisson error of $\gtrsim 30\%$ in the number of SNe observed. (Sources of error are summarized in §5.5.2 and Table 5.5.)

For the color distribution, in addition to a simple shift, we also quantify the effect of including a smaller or larger fraction of SNe significantly reddened by dust. In fact, we have good reasons to believe that most cluster SNe Ia will be in dust-free environments. A large fraction of the stellar mass in the clusters ($\sim 80\%$) is contained in red-sequence galaxies expected to have little or no dust. Our spectroscopic and photometric analysis (Meyers et al. 2011) of the red-sequence galaxies confirms this expectation. Therefore, for our default c distribution (Fig. 5.2, right panel, solid line), we assumed that 20% of SNe (those occurring in galaxies not on the red sequence) could be affected by dust, and that

the extinction of these SNe would be distributed according to $P(A_V) \propto \exp(-A_V/0.33)$. This distribution is based on the inferred underlying A_V distribution of the SDSS-II sample (Kessler et al. 2009, hereafter K09). All SNe are assumed to have an intrinsic dispersion in color to match the observed SNLS distribution at $c < 0.3$. It might be the case that even fewer SNe are affected by dust, or (unlikely) more SNe are affected by dust. As extreme examples, we tested two alternative distributions (dotted lines in Fig. 5.2). In the first, we assumed that the SNLS sample was complete and characterized the full c distribution, with a negligible number of $c > 0.4$ SNe. This increases the control time by only 2%. In the second, we increase the fraction of dust-affected SNe from 20% to 50%. Even though this alternative distribution includes an additional $\sim 30\%$ more reddened SNe (unlikely to be true in reality), the average control time is only lower by 9% (increasing the rate by 10%). We use these values as the systematic error in the assumed dust distribution.

5.4 Cluster Luminosities and Masses

In this section, we calculate the total luminosity of each cluster and use the luminosity to infer a stellar mass. Only a small subset of galaxies in each field have known redshifts, making it impossible to cleanly separate cluster galaxies from field galaxies. Therefore, we use a "background subtraction" method to estimate cluster luminosities statistically: we sum the luminosity of all detected galaxies in the field and subtract the average "background luminosity" in a non-cluster field. This approach follows that of Sharon et al. (2007). For the blank field, we use the GOODS[1] (Giavalisco et al. 2004) fields as they have similarly deep or deeper observations in both ACS i_{775} and z_{850}.

In §5.4.1 we describe the estimation of image backgrounds, which must be subtracted to avoid biasing photometry measurements. §5.4.2 describes the galaxy detection and photometry method. Simply summing the photometry from the detected galaxies would include most of the total cluster light. However, for an unbiased estimate of the total light, several small corrections are necessary: We account for light in the outskirts of each galaxy (§5.4.3), and light from faint galaxies below the detection threshold (§5.4.5). These corrections are on the order of 20% and 5% respectively. In §5.4.4 we convert the observed z_{850} flux to a rest-frame B-band flux. §5.4.6 describes the method for determining the center of a cluster. In §5.4.8 we sum the light and subtract light from non-cluster galaxies, creating a profile of cluster light as a function of radius. In §5.4.9 we repeat this calculation limiting ourselves to red-sequence and red-sequence early-type subsets of galaxies. Finally, in §5.4.10 we estimate cluster stellar masses based on the cluster luminosities and stellar mass-to-light ratios.

---

[1]Based on observations made with the NASA/ESA *Hubble Space Telescope*. The observations are associated with programs GO-9425, GO-9583 and GO-10189

Table 5.1. SEXTRACTOR parameters for galaxy detection and photometry

Parameter Name	Object Masking for Image Background	Object Detection	
		Cold Value	Hot Value
FILTER	Y	Y	Y
CLEAN	Y	Y	Y
CLEAN_PARAM	1.2	1.2	1.2
BACK_TYPE	AUTO	AUTO	AUTO
BACK_SIZE	120	5	4
BACK_FILTERSIZE	4	5	4
DETECT_MINAREA	5	50	5
DETECT_THRESH	1.65	3.0	1.65
ANALYSIS_THRESH	1.65	3.0	1.65
DEBLEND_NTHRESH	64	64	64
DEBLEND_MINCONT	0.05	0.007	0.05
PHOT_AUTOPARAMS	8.0, 3.3	5.0,0.0	5.0,0.0

5.4.1 Image Background Subtraction

Any residual image background will bias derived galaxy magnitudes. We use a custom background subtraction algorithm to take out any residual large-scale varying background. We start with stacked images produced by MUTIDRIZZLE. The individual images are already background subtracted prior to the MULTIDRIZZLE process, but we find that the stacked images have a small positive mean background.

Objects are detected with Source Extractor (SEXTRACTOR; Bertin & Arnouts 1996) using the standard one-pass, single-image mode. SEXTRACTOR is allowed to determine its own spatially-varying image background, solely for the purposes of object detection and object geometry. The relevant detection parameters are given in Table 5.1. A mask is then created based on the SEXTRACTOR catalog – all pixels inside an object's MAG_AUTO aperture are masked. In particular, note that PHOT_AUTOPARAMS is set to [8.0, 3.3]. This means that each object is masked out to 8 times its Kron radius. (See §5.4.3 below for a more detailed discussion of MAG_AUTO and Kron radius.) The radius used for masking objects is a trade-off between ensuring that all galaxy light is masked and having any pixels left for background determination. With these settings, typically between half and two thirds of the pixels in the image are masked (Fig. 5.4). The background is then determined in 50×50 pixel boxes (all pixels in each box are assigned the same background). At the location of each box, we take all unmasked pixels in a 500×500 pixel box. If there are not "enough" unmasked pixels in this box to determine a reliable background, we expand the box until there are enough. When there are enough, we take the mean of the unmasked pixels as the background for all pixels in the 50×50 pixel box.

In Fig. 5.4 (right column) one can see that the images typically have a positive flux background. For reference, summed over a 10 (20) pixel radius aperture a flux of 0.0005 counts s^{-1} pixel^{-1} is equivalent to a flux of 0.157 (0.628) counts s^{-1}, or a $z_{850} = 26.87$
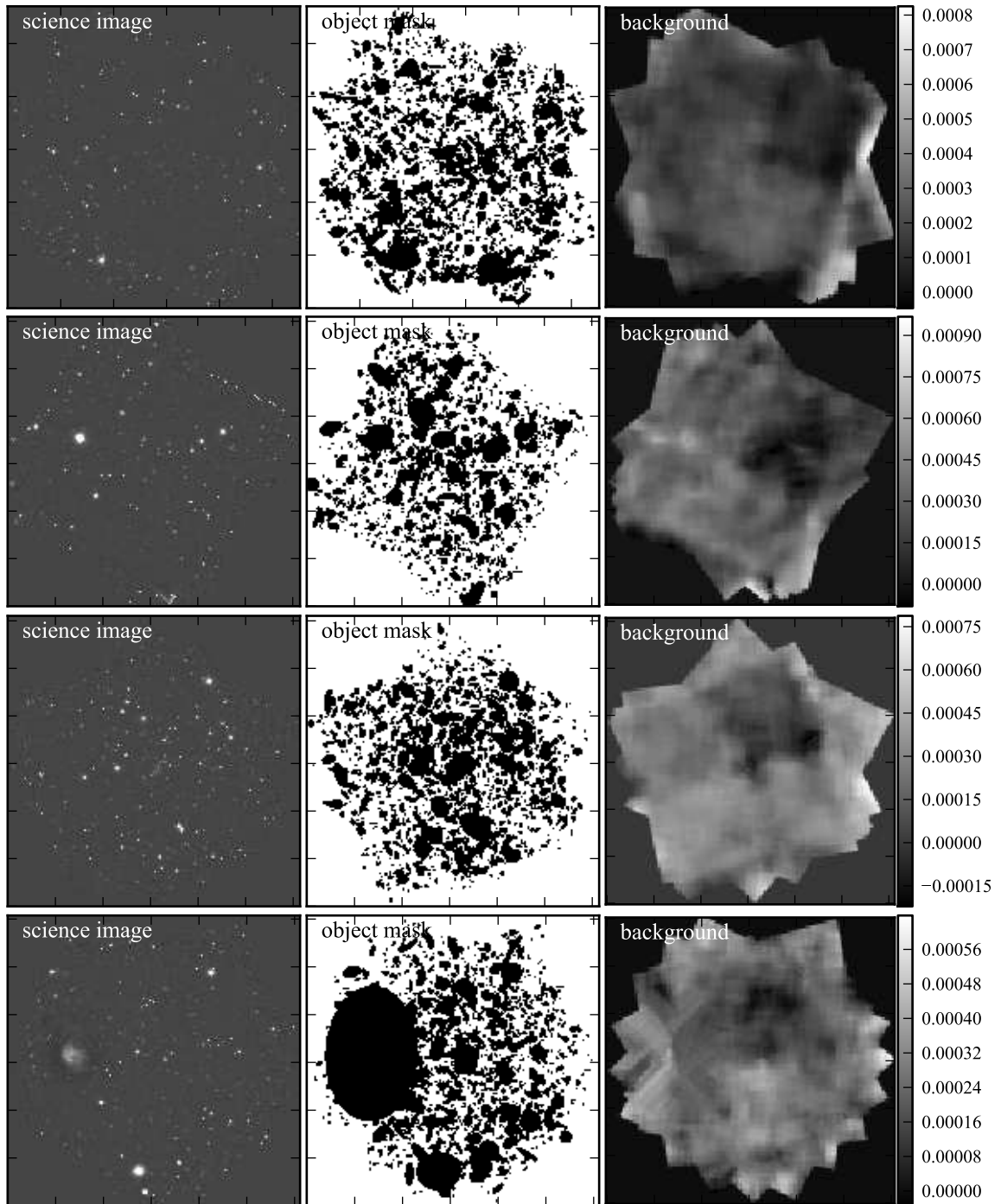
Figure 5.4. Examples of background determination for the z_{850} image of clusters A, B, C and E (descending by row). The columns are the science image (left), object mask (center), and derived image background (right). The scale is counts s^{-1} pixel^{-1} in the background image.

(25.37). The other feature that stands out is a quadrant effect. For clusters A, B and C, one quadrant of the image has a background that is clearly lower than the other quadrants. The effect is less obvious in clusters where the component images had a wider range of orientations (like cluster E).

5.4.2 Galaxy Detection and Photometry

For galaxy detection and photometry we use the stacked i_{775} and z_{850} band images of each cluster, which have total exposure times in the range $1060 - 4450$ seconds and $5440 - 16{,}935$ seconds, respectively.

Detection

Galaxy catalogs are created using the two-pass "Cold/Hot" method of running SEx-TRACTOR first developed by Rix et al. (2004) and adapted to this survey in Meyers et al. (2011). In the Cold/Hot method, SEXTRACTOR is first run in dual-image mode using the z_{850} image for detection. The detection thresholds are generally set fairly high (Table 5.1) in order to detect only the brighter galaxies. The "segmentation map", which represents which pixels belong to a galaxy, is saved. SEXTRACTOR is then run again (also in dual-image mode using the z_{850} image for detection) but with more lenient detection parameters, in order to find the fainter galaxies. This second catalog is then cleaned by throwing out galaxies that fall on pixels belonging to galaxies in the first catalog. The cleaned second catalog is then combined with the first catalog. We remove stars from the catalog based on the CLASS_STAR and FLUX_RADIUS parameters from the z_{850} image.

For consistency with Meyers et al. (2011), objects are detected using the stacked z_{850} images prior to background subtraction. However, photometry for both z_{850} and z_{775} is done on the background subtracted images. Thus, for the photometry image in dual-image mode, the SEXTRACTOR parameters BACK_TYPE=MANUAL and BACK_VALUE=0.0 are used.

Photometry

It is notoriously difficult to determine accurate total fluxes for extended sources. MAG-AUTO is generally thought to be SEXTRACTOR's most reliable estimator of total flux, but can still be wrong by a large amount depending on the galaxy. MAG_AUTO gives the total magnitude of an object inside a flexible elliptical aperture, with *no aperture correction*. The size of the elliptical aperture is based on the Kron radius. Although it varies from the original definition, for the purposes of SEXTRACTOR Bertin & Arnouts (1996) define the Kron radius as

$$R_1 = \frac{\Sigma R I(R)}{\Sigma I(R)} \tag{5.7}$$

over the two-dimensional aperture. The elliptical aperture used has a semi-minor axis length KR_1 where the user can chose the Kron factor K. Theoretically, an aperture with, for example, $K = 2$ will enclose approximately 90% of the light of a galaxy with a Sérsic (1968) profile, nearly independent of its Sérsic index of the galaxy (Graham & Driver 2005).

On real images with noise, things are more complicated. Because the outskirts of the galaxy are in the noise, SEXTRACTOR will only assign pixels in the inner part of a galaxy to each galaxy, and only these pixels will be counted in determining R_1. As a result, R_1 is underestimated. The amount by which it is underestimated depends on the Sérsic index of the galaxy and its surface brightness with respect to the background noise. As a result, the fraction of light that an actual MAG_AUTO aperture encloses depends on the all above factors. In order to use MAG_AUTO magnitudes as an accurate estimate of total light, we must find the aperture correction empirically for our data. We do this using the Monte Carlo simulation described below.

In order to make the aperture correction as small as possible, we use a relatively large Kron factor of 5.0 in our MAG_AUTO photometry. MAG_AUTO is only used to determine z_{850} magnitudes; $i_{775} - z_{850}$ colors are determined using PSF matching and a smaller aperture in Meyers et al. (2011).

5.4.3   Galaxy Detection Completeness and Magnitude Bias

To count all the flux in all cluster galaxies, we must make two corrections: (1) add the galaxy light outside of the MAG_AUTO aperture, and (2) add the luminosity of all cluster galaxies below the detection threshold of our galaxy catalog. We use a Monte Carlo simulation of galaxies placed on the real survey data to determine both the detection efficiency as a function of galaxy magnitude, and the fraction of galaxy light inside the MAG_AUTO aperture.

Galaxy Monte Carlo Simulation

Each simulated galaxy has an elliptical Sérsic profile given by

$$r = \sqrt{x^2 + (y/q)^2} \tag{5.8}$$

$$\Sigma(r) = \Sigma_e e^{-\kappa[(r/r_e)^{1/n}-1]} \tag{5.9}$$

where κ is coupled to n such that half the total flux is always within r_e. For $n \gtrsim 2$, $\kappa \approx 2n - 0.331$; at low n, $\kappa(n)$ flattens out toward 0, and is obtained by interpolation. Here we use the approximation $\kappa(n) = 1.7233n^{1.0902}$ for $0 < n < 2$ and $\kappa = 2n - 0.331$ for $n > 2$. The total flux is given by

$$F_{\text{tot}} = 2\pi r_e^2 \Sigma_e e^{\kappa} n \kappa^{-2n} \Gamma(2n) q \tag{5.10}$$
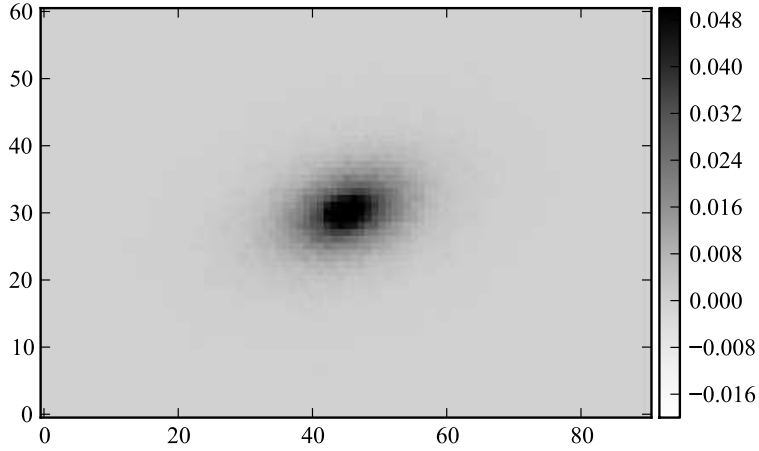
Figure 5.5. Example of a simulated galaxy with Sérsic index $n = 1$, ellipticity $q = 0.6$, magnitude $z_{850} = 22.5$, and effective radius $r_e = 9$ pixels. Poisson noise is included but background noise has not been added.
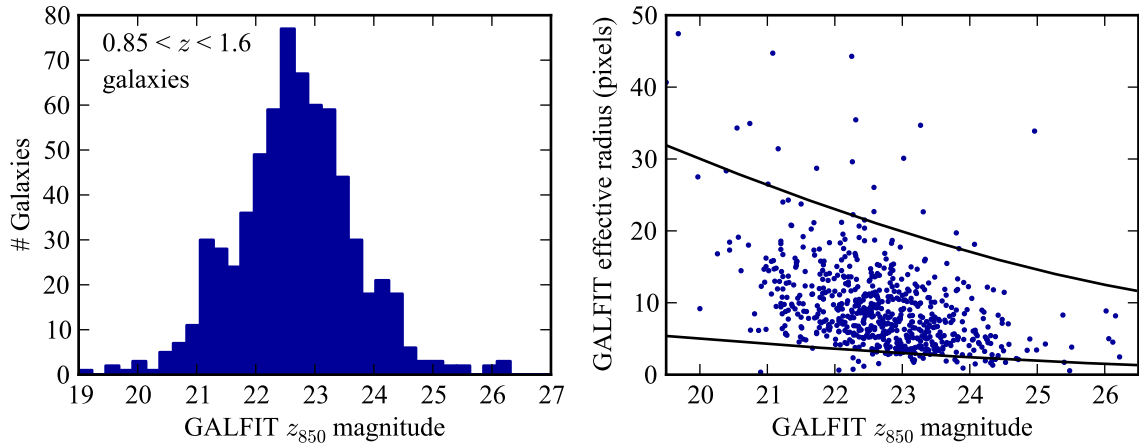
Figure 5.6. *Left panel:* The distribution of GALFIT z_{850} magnitudes for the 672 galaxies with spectroscopic redshifts $0.85 < z < 1.6$. *Right panel:* The GALFIT effective radius r_e as a function of magnitude for the same galaxies. The black lines show the range of effective radius used in the Monte Carlo. Given a simulated galaxy magnitude, an effective radius is randomly selected from a flat distribution between the lower and upper black lines.

where $\Gamma(2n)$ is the gamma function. The simulated galaxy is convolved with a (very rough) 3×3 PSF and Poisson noise is added. Each galaxy is simulated out to a radius of $5r_e$. An example of a simulated galaxy is shown in Figure 5.5.

The Sérsic index n is simply selected from a flat distribution ranging from $n = 0.7$ to $n = 4.5$, and the minor to major axis ratio q selected from a flat distribution ranging from $q = 0.3$ to $q = 1$. The distribution of galaxy angular sizes r_e will also affect the results. For guidance on the size of the galaxies of concern (namely, those at $z \gtrsim 0.9$) we turned to the 672 galaxies in the survey with spectroscopic redshifts in the range $0.85 < z < 1.6$. These 672 galaxies were all fit with GALFIT (Peng et al. 2002), which fits a value for r_e. Figure 5.6 (left panel) shows the distribution of r_e and total magnitude for these galaxies. Based on

Figure 5.7. The distribution of image depths (in effective exposure time) at the location of simulated galaxies. *Top panel:* A total of 15,000 simulated galaxies were placed on cluster images. *Bottom panel:* A 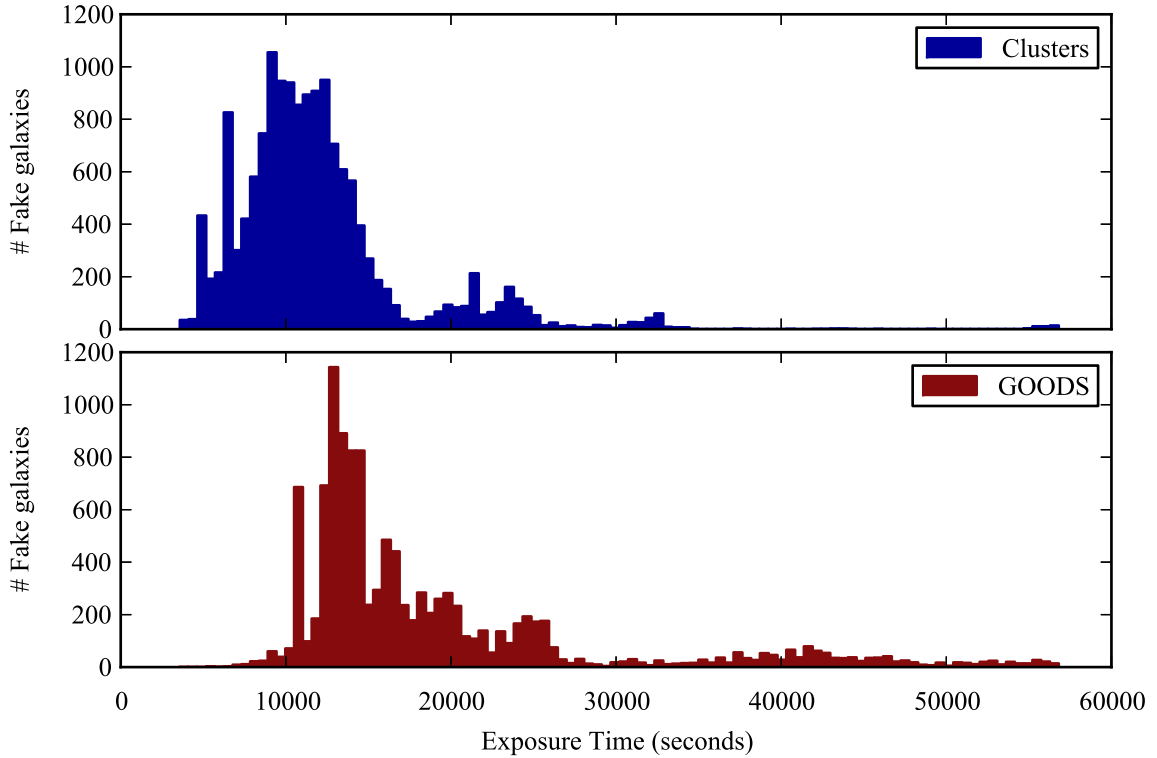total of 12,000 simulated galaxies were placed on GOODS images. 304 galaxies were placed on the HUDF which has an effective exposure time of approximately 350,000 seconds, and are thus not shown.

this distribution (and considering that dimmer galaxies and those with larger effective radii are selected against), we chose a range of effective radius that depends on the magnitude, shown in Fig. 5.6, left panel, between the two black lines. Given a magnitude, a galaxy's effective radius is chosen from a uniform distribution of r_e in the range shown.

To avoid overcrowding the images, only 200 galaxies are placed on each image. Galaxies are only placed on the same regions of the images used in the cluster luminosity analysis. For the GOODS fields, this is selected circular regions with radii 1.4 arcminutes. For the cluster fields, only regions with effective exposure time above a certain threshold are used. This effectively eliminates the outskirts of each field, leaving a region with mostly uniform depth for each cluster. The distribution of effective exposure times at the location of the simulated galaxies is shown in Fig. 5.7 for all galaxies placed on cluster fields (top panel) and all galaxies placed on GOODS fields (bottom panel). Additionally, we enforce a minimum separation of 10 pixels between the center of a simulated galaxy and the center of any existing galaxy (and a minimum separation of 100 pixels from the center of any existing galaxy brighter than $z_{850} \sim 21$). This ensures that the simulated galaxies will not
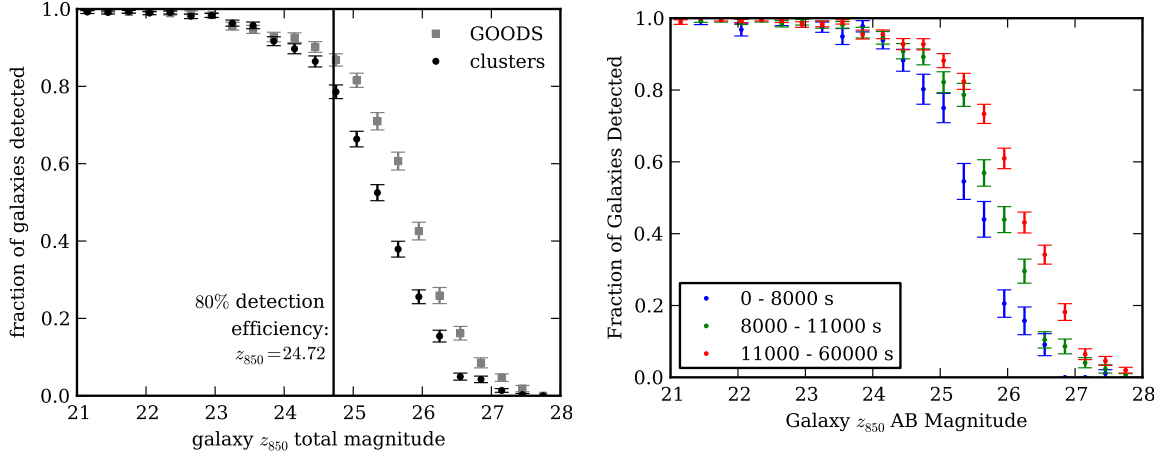
Figure 5.8. *Left panel:* Percentage of simulated galaxies recovered by SEXTRACTOR as a function of total galaxy z_{850} magnitude for simulated galaxies placed on cluster fields (black circles) and GOODS fields (grey squares). The detection efficiency drops to 80% at $z_{850} = 24.72$ for cluster fields (vertical line). We discard all galaxies dimmer than this value. *Right panel:* The variation in detection efficiency with exposure time, for cluster fields only. There are 2654, 4877, and 7469 galaxies in the three bins in order of increasing image depth. The corresponding 80% recovery magnitudes are 24.76, 25.33, and 25.48 (AB). The differences in detection efficiency are small, particularly above the $z_{850} = 24.72$ (Vega) = 25.26 (AB) magnitude cutoff.

be confused with existing galaxies and the output catalog will be cleanly comparable with the input catalog. A total of 15,000 and 12,000 galaxies were simulated on cluster fields and GOODS fields respectively.

Images with simulated galaxies added are then run through the background-subtraction and catalog-extraction pipelines. The resulting catalog for each image is then compared to the input galaxies. The closest detected galaxy within 5 pixels of a simulated galaxy is matched to the simulated galaxy. If no galaxy is detected within 5 pixels of a simulated galaxy, the galaxy is counted as not having been found by SEXTRACTOR.

Galaxy Detection Efficiency

The detection efficiency as a function of galaxy magnitude is shown in Figure 5.8. For the average of all cluster fields, the detection efficiency drops to 80% at $z_{850} = 24.72$. We use this magnitude as a cutoff in our selection, discarding all galaxies dimmer than this magnitude. We later correct total cluster luminosities for the uncounted light from these galaxies by using an assumed cluster luminosity function. In reality, the detection efficiency varies slightly from field to field (and even within a field) due to exposure time variations (Fig. 5.8, right panel, shows the variation in detection efficiency with exposure time for cluster fields). However, to first order the variation is accounted for by using the average efficiency in all fields. In addition, the total luminosity of $z_{850} > 24.72$ cluster galaxies is small (as shown below), so slight changes in the cutoff will have a negligible effect on the total luminosity.

MAG_AUTO Aperture Correction

The fraction of galaxy light falling inside the MAG_AUTO aperture will depend on several parameters of the galaxy, including the galaxy magnitude, and Sérsic index n. To see the dependence on magnitude and n, in Figure 5.9 we split the simulated galaxies into bins in magnitude and n. For the galaxies in each bin, we plot the distribution of the difference between the true total magnitude and the MAG_AUTO magnitude. A Gaussian fit, and its μ and σ parameters, are shown for reference. As expected, the distributions are wider for fainter magnitudes (descending rows in the figure) due to increasing photometric error. The distributions have somewhat non-Gaussian tails, particularly on the negative side. On the negative side, this is most likely due to collisions with other galaxies, where flux from a nearby galaxy falls in the aperture. Also as expected, the offset grows larger with both increasing n and increasing magnitude. As n or magnitude increases, the outskirts of the galaxy are increasingly buried in noise, causing SEXTRACTOR to underestimate the Kron radius, leading to a smaller MAG_AUTO aperture. For each distribution, ΔM is the magnitude correction one would need to make to each galaxy in order for the *total* output flux to match the *total* input flux. Aperture corrections are based on ΔM in each bin, and thus take into account the non-Gaussian tails in the distributions.

We derive a relation between ΔM and the galaxy brightness (Fig. 5.10, black circles), summing over all n. We find that the relation is well-fit by a second-order polynomial (Fig. 5.10, thick black line), given by

$$\Delta M = 0.238 + 0.081(M_{MAG\_AUTO} - 23) + 0.009(M_{MAG\_AUTO} - 23)^2. \qquad (5.11)$$

We use this to correct the magnitude of each detected galaxy. Note that the correction is not extrapolated beyond the fitted range shown.

Because we cannot reliably determine r_e or the Sérsic index n for each galaxy, we rely on the simulated distribution of r_e and n to accurately represent the true distributions. (The black circles in Fig. 5.10 include all simulated galaxies.) We have based our distribution of r_e on actual galaxies, but n is less well-known. To estimate the effect of varying the n distribution, we show ΔM for subsets of the simulated galaxies, divided by Sérsic index (Fig. 5.10, grey points and lines). If, instead of the flat $1 < n < 4$ distribution used, all galaxies had $1 < n < 2$, the aperture correction would be lower by approximately 0.10 magnitudes. If instead all galaxies had $3 < n < 4$, the correction would be higher by approximately 0.07 magnitudes. We use 0.07 mag as the systematic uncertainty in the aperture correction. (All systematic uncertainties are summarized in §5.5.2 and Table 5.5.)
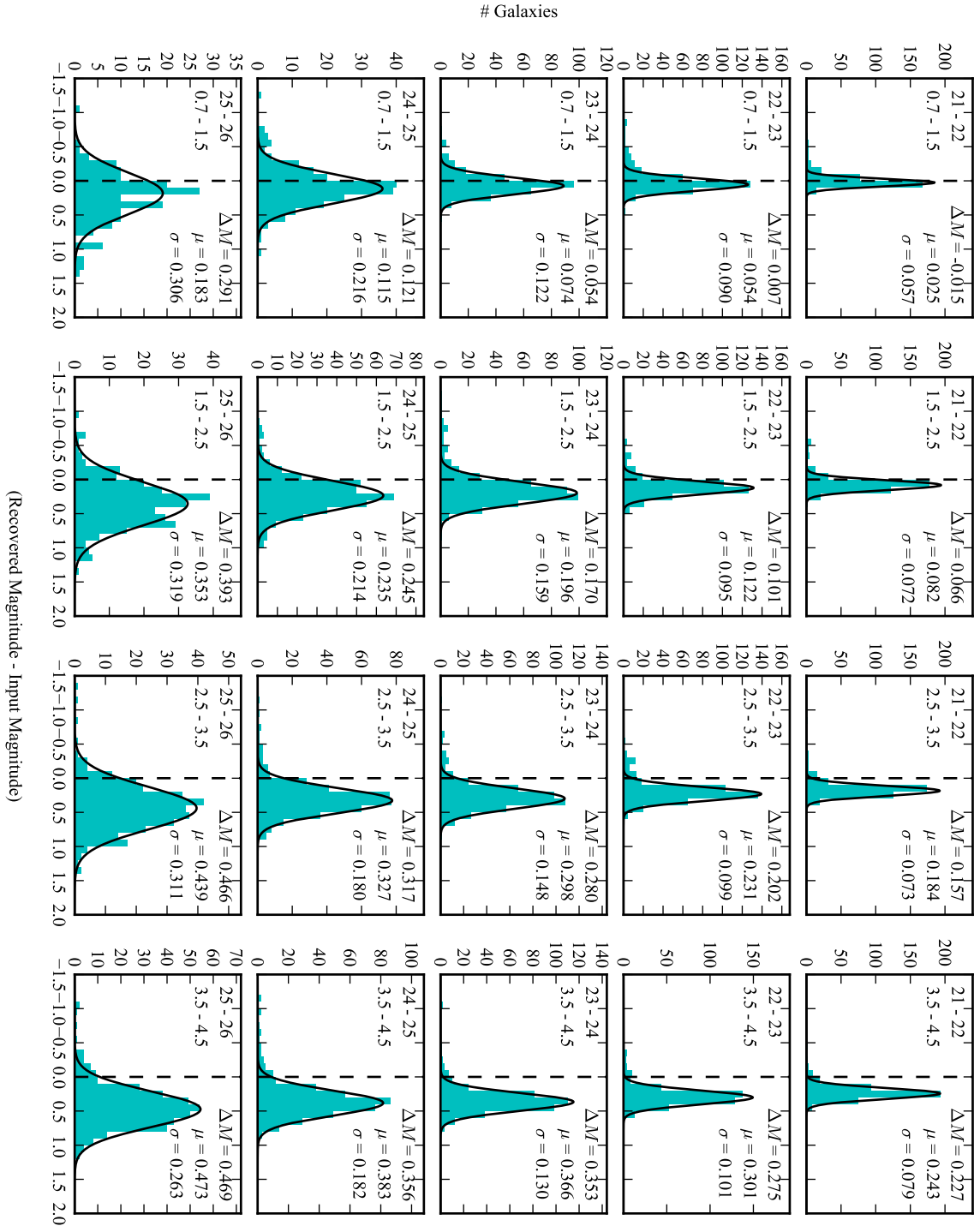
Figure 5.9. The distribution of aperture corrections as a function of magnitude and Sérsic index n. The range of magnitudes and Sérsic indices included in each panel is given in the upper left of the panel. ΔM is the magnitude correction derived from ratio of the total flux extracted to the total flux input. μ and σ describe the Gaussian fit to each distribution.
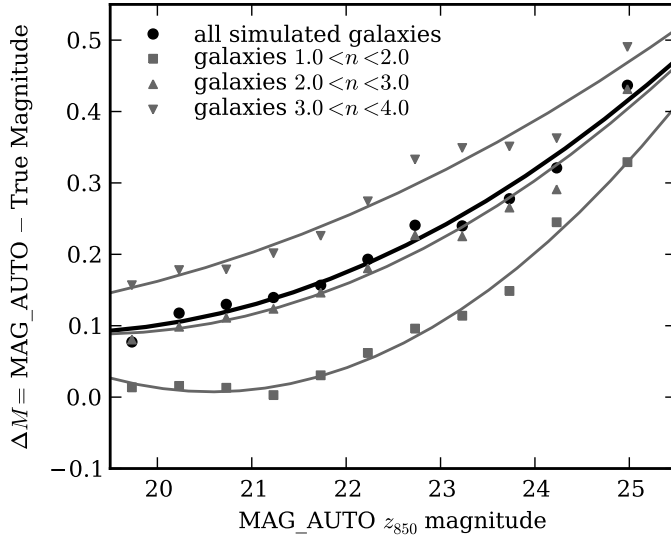
Figure 5.10. Galaxy MAG_AUTO aperture correction as a function of galaxy magnitude. The black circles show the average correction for the full distribution of galaxies simulated, including all Sérsic indices n. The black line is a fit to these points and is the relation we use. Note that it is not extrapolated beyond the range shown. To illustrate the effect of n on the aperture correction, we plot the aperture correction for subsets of galaxies with different Sérsic indices (Grey squares and triangles). Galaxies with larger Sérsic indices have a larger aperture correction.

5.4.4 K-Corrections

We use a K-correction based on the BC03 stellar population spectral models to convert the observed z_{850} magnitude to a rest-frame B magnitude for each cluster. The BC03 models consist of galaxy spectra for an instantaneous starburst ("simple stellar population", or SSP) with various initial metallicities ($0.0001 < Z < 0.1$) and ages ($1 \times 10^5 - 2 \times 10^{10}$ yr). BC03 contains models for several different stellar evolution prescriptions, and two initial mass functions (IMF). We use the recommended Padova 1994 stellar evolution prescription and Chabrier IMF. Figure 5.11 shows examples of BC03 spectra for metallicity $Z = 0.02$ at a range of ages. Also shown are the rest-frame U and B bands, as well as the observed i_{775} and z_{850} bands at the minimum (0.91) and maximum (1.50) redshift of clusters in the sample. The z_{850} filter is a good match to rest-frame B band across much of the redshift range of the clusters. It is the best match at $z \approx 1.07$ and shifts progressively bluer than B at higher redshifts, approximately matching U at the high-redshift end of the sample.

Rather than using a single K-correction for all the light in each cluster, we apply a K-correction to each galaxy magnitude based on its $i_{775} - z_{850}$ color. For each cluster's redshift, we determine the relation between K-correction (M_B (rest) $-z_{850}$) and $i_{775} - z_{850}$ color, using BC03 spectra with initial metallicities in the range $0.004 < Z < 0.05$ and ages in the range $1 \times 10^8 - 5 \times 10^9$ yr. This relation is shown for four example cluster redshifts in Figure 5.12 (left panels). The colored lines in each panel represent BC03 spectra with constant metallicity and age increasing from $1 \times 10^8 - 5 \times 10^9$ yr. For most cluster redshifts in our sample, all of the spectra over this wide range fall along the same line in K-correction versus color, meaning that the color determines the K-correction, regardless of the metallicity or age assumed. At $z = 1.07$, where the best match between z_{850} and rest-frame B is obtained, the K-correction is nearly independent of color or model,
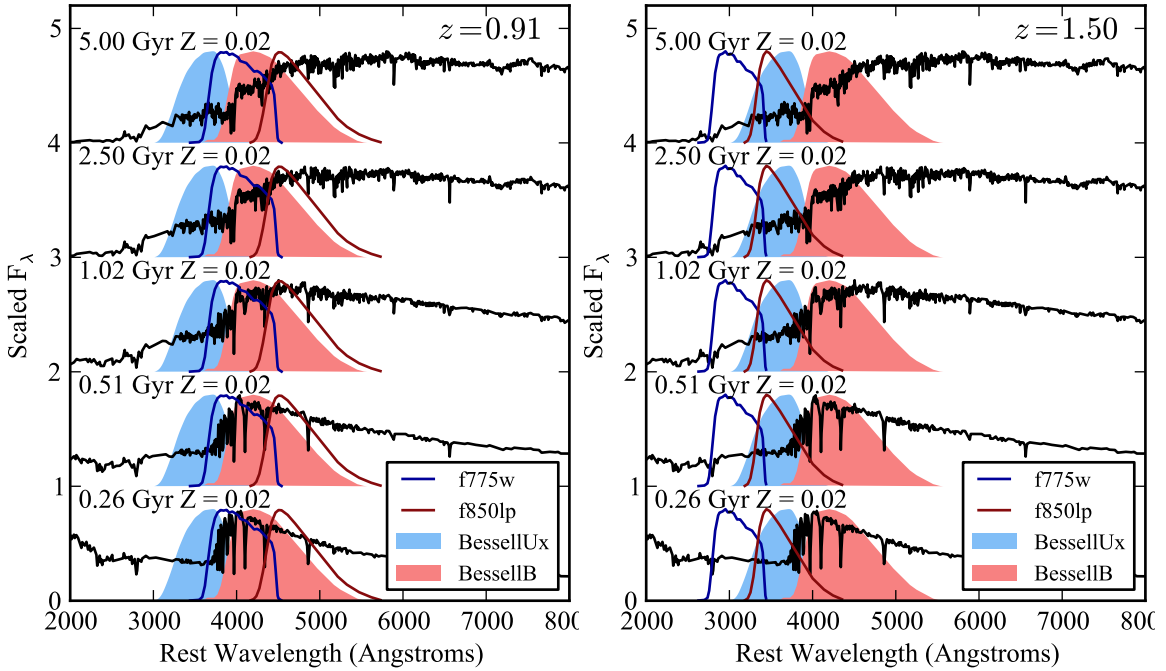
Figure 5.11. Examples of BC03 spectra for a single initial metallicity ($Z = 0.02$) and a range of ages. The left and right panels are identical, except that the *left panel* shows the observed filters at $z = 0.91$ and the *right panel* shows them at $z = 1.50$ (the approximate range of cluster redshifts).

as one would expect. In the redshift range $1.15 \lesssim z \lesssim 1.4$, the curves are multi-valued for a range of observed colors, and are the most dispersed at $z \approx 1.26$ (shown in Figure 5.12). To select a K-correction given an observed galaxy color, we average the K-correction for all models with similar colors, arriving at the black line shown in each panel.

The dispersion of the models about the best-fit line is < 0.03 mag at redshifts $\lesssim 1.1$ and $\gtrsim 1.4$, and reaches its largest value of 0.09 mag at $z = 1.26$. We calculate the K-correction for each galaxy using this best-fit relation, effectively assuming that every galaxy is at the cluster redshift. This results in an incorrect luminosity for non-cluster member galaxies, but this is accounted for by performing the same K-correction on the galaxies in the GOODS fields prior to subtracting their luminosity.
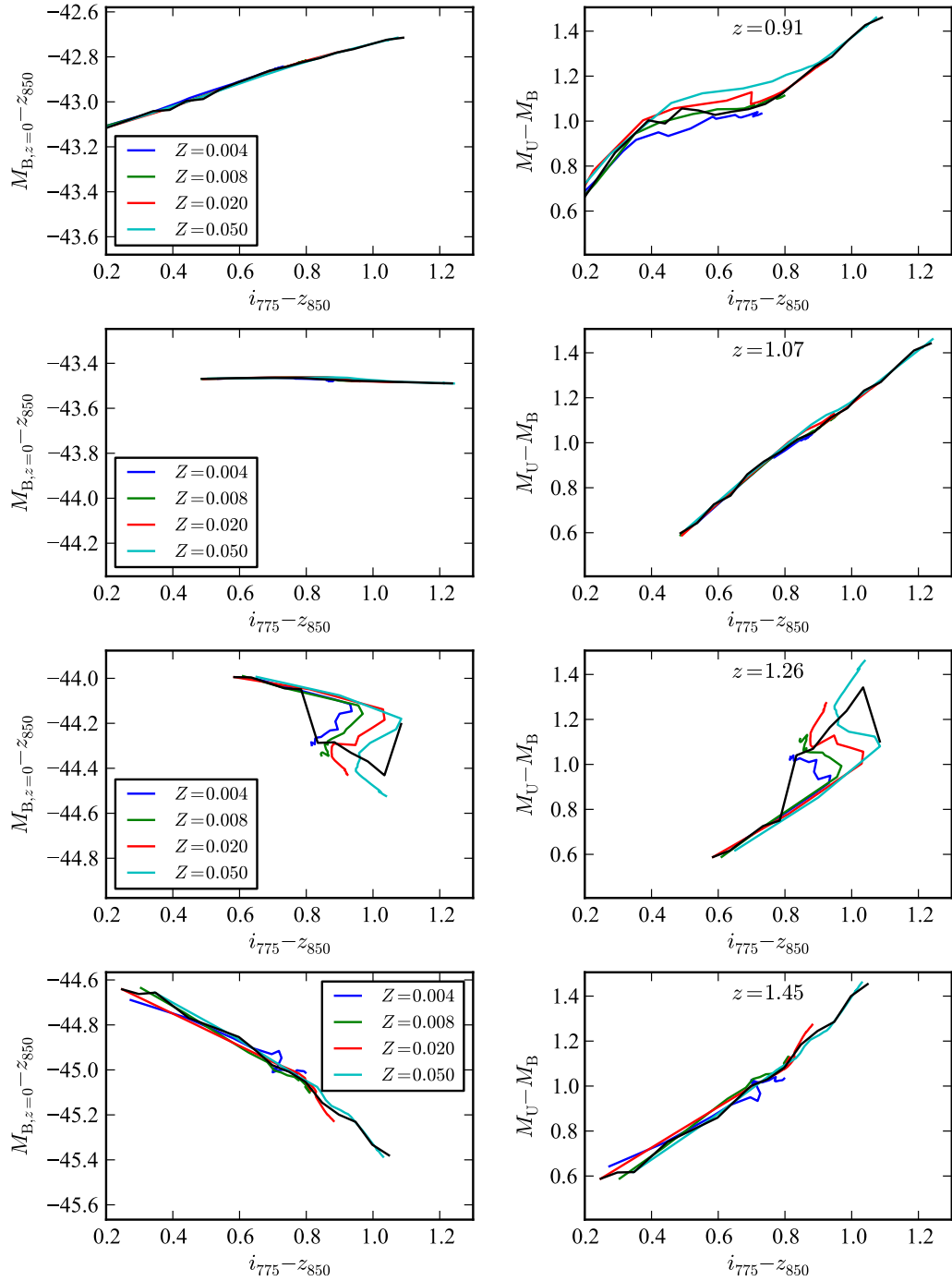
Figure 5.12. K-correction fits, based on BC03 spectra. The colored lines in each panel represent BC03 spectra with constant initial metallicity and age increasing from $1 \times 10^8 - 5 \times 10^9$ yr. The black line is the relation used in this analysis. The *left panels* show the K-correction as a function of observed galaxy color and the *right panels* show the rest-frame $U - B$ color as a function of observed color.

5.4.5   Luminosity Function Correction

We estimate the total luminosity of all galaxies below the detection limit of $z_{850} = 24.72$ using a Schechter (1976) luminosity function, which gives the number of galaxies in the luminosity interval $[L, L + dL]$ in a given sample,

$$\Phi(L)dL = \Phi^*(L/L^*)^\alpha e^{-L/L^*} d(L/L^*). \tag{5.12}$$

Φ^* is a normalization, L^* is a characteristic galaxy luminosity, and α is a unit-less constant. The ratio of total to observed luminosity is then

$$C = \frac{\int_0^\infty L\Phi(L)dL}{\int_{L_{lim}}^\infty L\Phi(L)dL}, \tag{5.13}$$

and we multiply each observed cluster luminosity by C to get the total luminosity.

We assume values for L^* and α determined in other studies and use our data to perform a rough consistency check. For α, studies have shown that the value does not evolve much from low redshift, at least for redder galaxies. Analyzing only red galaxies in 28 clusters spanning $0 < z < 1.3$, Andreon (2008) find $\alpha = -0.91 \pm 0.06$ (rest-frame V-band) with no discernible trend in redshift (see also Andreon 2006b,c). From five intermediate-redshift clusters ($0.54 < z < 0.9$), Crawford et al. (2009) find a somewhat flatter faint-end slope $\alpha \sim -0.6$ (rest-frame B-band) for the red-sequence luminosity function. Looking at the full luminosity function, Goto et al. (2005) find $\alpha = -0.82 \pm 0.10$ in one cluster at $z = 0.83$ (rest-frame B-band), compared to $\alpha = -1.00 \pm 0.06$ in 204 low-redshift clusters (rest-frame g-band) (Goto et al. 2002). In redder bands, Strazzullo et al. (2006) find $\alpha \sim -1$ for three clusters at redshifts $1.11 < z < 1.27$ (in approximately rest-frame z band). Summarizing, most studies find a value consistent with $\alpha \sim -0.9$, and we assume this value in computing C.

Values for M^* are also reported in most of the above-mentioned studies. Studies of red galaxies find that the variation of M^* with redshift is consistent with passive evolution, with M^* decreasing towards higher redshifts (Andreon 2006c; Crawford et al. 2009). Crawford et al. (2009) find $M_B^* = -21.1$ and $M_B^* \sim -21.3$ (with errors of approximately a half magnitude) for two clusters at redshifts 0.75 and 0.83. K-correcting from the observed [3.6]-band, Andreon (2006c) find $M_B^* \sim -21.7$ at $z \sim 1.1$, with approximately 0.5 magnitudes of evolution between $z = 0.3$ and $z = 1.1$. At lower redshift (considering all galaxies) Goto et al. (2002) find $M_B^* \sim -21.6$, compared to $M_B^* \sim -21.0$ for one cluster at $z = 0.83$ (Goto et al. 2005). On the basis of these measurements, we assume a value of $M_B^* = -21.7$.

We have checked our assumed M_B^* and α for consistency with our data. With the set of spectroscopically-confirmed cluster galaxies from our clusters at $z < 1.2$, we confirmed that the bright end of the luminosity function is consistent with $M_B^* = -21.7$, and strongly inconsistent with values outside the range $M_B^* = -21.7 \pm 0.5$. We also determined the luminosity function using a statistical subtraction of the "background" luminosity function
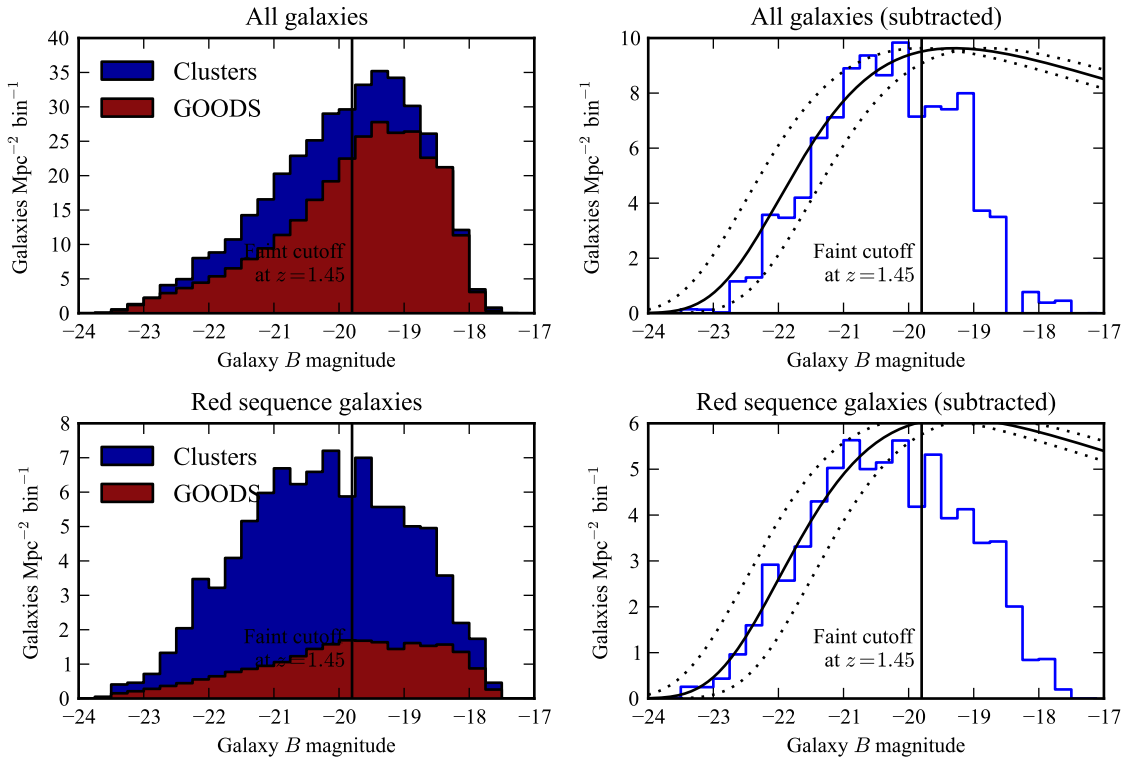
Figure 5.13. The luminosity function of cluster galaxies (*top panels*) and red-sequence-only galaxies (*bottom panels*). The *left panels* show the luminosity function in cluster fields and GOODS fields, showing the clear overdensity in the cluster fields relative to GOODS. The *right panels* show the distribution after subtracting the GOODS distribution. The black solid line shows the luminosity function we assume here ($M_B^* = -21.7$, $\alpha = -0.9$) with dotted lines showing the range used to asses the systematic uncertainty ($M_B^* = -21.7 \pm 0.5$). These distributions are only reliable to the left of the vertical solid line, which represents the detection limit in the highest-redshift cluster.

from the GOODS fields (Fig. 5.13), finding excellent agreement with the assumed M_B^* and α values over the range $-24 < M_B < -19.8$. ($M_B = -19.8$ corresponds to the detection limit in the highest-redshift clusters.)

For each cluster, we calculate C in the observer frame, converting $M_B^* = -21.7$ to the observed z_{850} band, using the cluster redshift and a K-correction based on a passive galaxy template. In Table 5.2 we report the value z_{850}^* and the resulting correction C for each cluster. The correction is less than 5% for the majority of clusters, rising to a maximum of 14% for the highest-redshift cluster. Because the correction is so small, varying the assumed values of M_B^* and α does not have a large effect on the total luminosity. Varying M_B^* by ± 0.5 mag (a larger range than that allowed by our data) changes the average correction by only $^{+4}_{-2}\%$. Varying α by ± 0.2 changes the average correction by $^{+5}_{-2}\%$. We conservatively take $^{+10}_{-3}\%$ (the full range when varying both concurrently) as the systematic uncertainty in luminosity from the faint-end correction (summarized in §5.5.2).

Table 5.2. Bright cutoff magnitudes and luminosity function parameters

ID	z	Cutoff from	z_{850}^{bright}	z_{850}^*	C
A	1.46	Max cD	21.09	22.80	1.143
B	1.12	cD	20.11	21.38	1.033
C	0.97	cD	19.87	20.79	1.018
D	1.02	BCG	20.13	20.95	1.021
E	1.03	cD	19.40	20.99	1.022
F	1.11	Max cD	19.63	21.34	1.031
G	1.26	BCG	20.34	22.04	1.064
H	1.24	BCG	20.33	21.95	1.058
I	1.34	Max cD	20.66	22.37	1.092
J	1.37	Max cD	20.77	22.50	1.104
K	1.41	Max cD	20.92	22.65	1.122
L	1.37	Max cD	20.77	22.50	1.104
M	0.90	Max cD	18.69	20.53	1.014
N	1.03	BCG	20.22	20.99	1.022
P	1.1	Max cD	19.58	21.29	1.030
Q	0.95	cD	20.01	20.66	1.015
R	1.22	Max cD	20.15	21.86	1.054
S	1.07	Max cD	19.44	21.16	1.026
T	0.97	Max cD	19.00	20.75	1.017
U	1.04	Max cD	19.31	21.04	1.022
V	0.90	cD	18.89	20.49	1.013
W	1.26	Max cD	20.33	22.04	1.064
X	1.10	Max cD	19.58	21.34	1.031
Y	1.24	cD	20.29	21.90	1.056
Z	1.39	cD	20.85	22.58	1.112

Note. — "Cutoff from" refers to how z_{850}^{bright} is determined. "cD": magnitude of visually central dominant galaxy. "BCG": magnitude of visually classified brightest cluster elliptical (but not central) galaxy. "Max cD": Cluster does not have obvious cD galaxy or clear BCG. In this case, z_{850}^{bright} is K-corrected from $M_B = -23.42$, the absolute magnitude of the brightest cD galaxy in the entire sample.

5.4.6 Determining Cluster Centers

The 25 clusters are heterogeneous in the spatial distribution of their member galaxies. Some clusters have very obvious cores with tens of red elliptical galaxies, while in others no central overdensity is obvious to the eye. For these later clusters, the exact "center" of the cluster is nearly impossible to define from the ACS imaging data. Because the luminosity analysis is not very dependent on having an accurate center, we use a hybrid method to arrive at the cluster positions listed in Table 2.1. For those clusters having a clear central-dominant (cD) galaxy, the position of the cD galaxy is used. Cluster Y has two close cD-like galaxies; the position given is that of the Southwest galaxy, which is slightly brighter and looks more centrally located with respect to other red elliptical galaxies. For the 18 clusters lacking a cD galaxy we first attempt to find a central overdensity

of red-sequence galaxies by choosing the position that maximizes the total luminosity of red sequence galaxies within 0.1 Mpc (where a red-sequence galaxy is one that has a color within 0.15 magnitudes of the cluster's red sequence and an ellipticity less than 0.5). We then averaged the position of the red sequence galaxies contained in that aperture (weighting by galaxy luminosity) to get a slightly more refined (and unique) position. This position is then evaluated by eye with respect to red elliptical galaxies outside the 0.1 Mpc circle. If the position represents a clear overdensity and seems consistent with galaxies outside the circle, we use this position. This is done for clusters F (16 red-sequence galaxies within 0.1 Mpc), G (11), I (8), N (14), R (18), T (19), W (16) and X (22). For clusters A (16), J (8), M (8) and S (7), the algorithm gives a reasonable result, but the overdensity seems offset from the larger distribution of galaxies and we chose a (nearby) position by eye. For clusters H, K, L, O, P, U, the algorithm either fails due to the presence of bright (lower redshift) red-sequence interlopers in the field, or because there is no clear overdensity of galaxies. For these clusters the center chose by eye is less reliable.

5.4.7 "Background" Luminosity

For each cluster we sum the K-corrected B-band luminosity of all galaxies brighter than the detection limit $z_{850} = 24.72$. To reduce noise, we discard galaxies that are clearly too bright to be cluster members. In clusters with a central dominant (cD) galaxy or dominant (but not central) brightest cluster galaxy(BCG), the bright cutoff magnitude is set to the magnitude of the cD galaxy or BCG. In clusters lacking a clearly dominant galaxy, we conservatively set the cutoff based on the absolute magnitude of the most luminous cD galaxy in any cluster, $M_B = -23.42$ (from cluster XMMU J2235.3−2557). The bright cutoff magnitude in the observer frame, $z_{850}^{\mathrm{bright}}$, is listed for each cluster in Table 5.2. Because the bright cutoff is chosen so conservatively, we expect that no cluster galaxies are discarded. The effect of being overly conservative is only to add noise, and this is captured in the statistical uncertainty described below.

For each cluster we apply the same selection criteria and K-corrections to the GOODS fields to determine the "background" specific to that cluster. The GOODS fields consist of a North field centered at approximately $\alpha = 12^{\mathrm{h}}36^{\mathrm{m}}$, $\delta = +62°14'$ and a South field centered at approximately $\alpha = 3^{\mathrm{h}}32^{\mathrm{m}}$, $\delta = -27°48'$. Each field has been imaged with ACS over an area of 15 ACS tiles, or $\sim$170 arcmin^2. I chose these fields because they have ACS z_{850} imaging to a depth similar to, or deeper than, the cluster fields, over a relatively wide area. Also, having two widely separated fields (North and South) helps minimize bias from galaxy density fluctuations.

We select 30 non-connected circular regions (15 in each of GOODS North and South) of radius $1'.4$, similar to the size of the cluster fields. ($1'.4$ corresponds to 0.654, 0.697, and 0.711 Mpc at $z = 0.9$, 1.2 and 1.5, respectively.) The distribution of luminosity densities in these 30 regions is shown for four example clusters in Figure 5.14. Because the same 30 regions are used for each cluster, the resulting distributions are quite similar, though not identical because of the different selections and K-corrections used. The average lu-
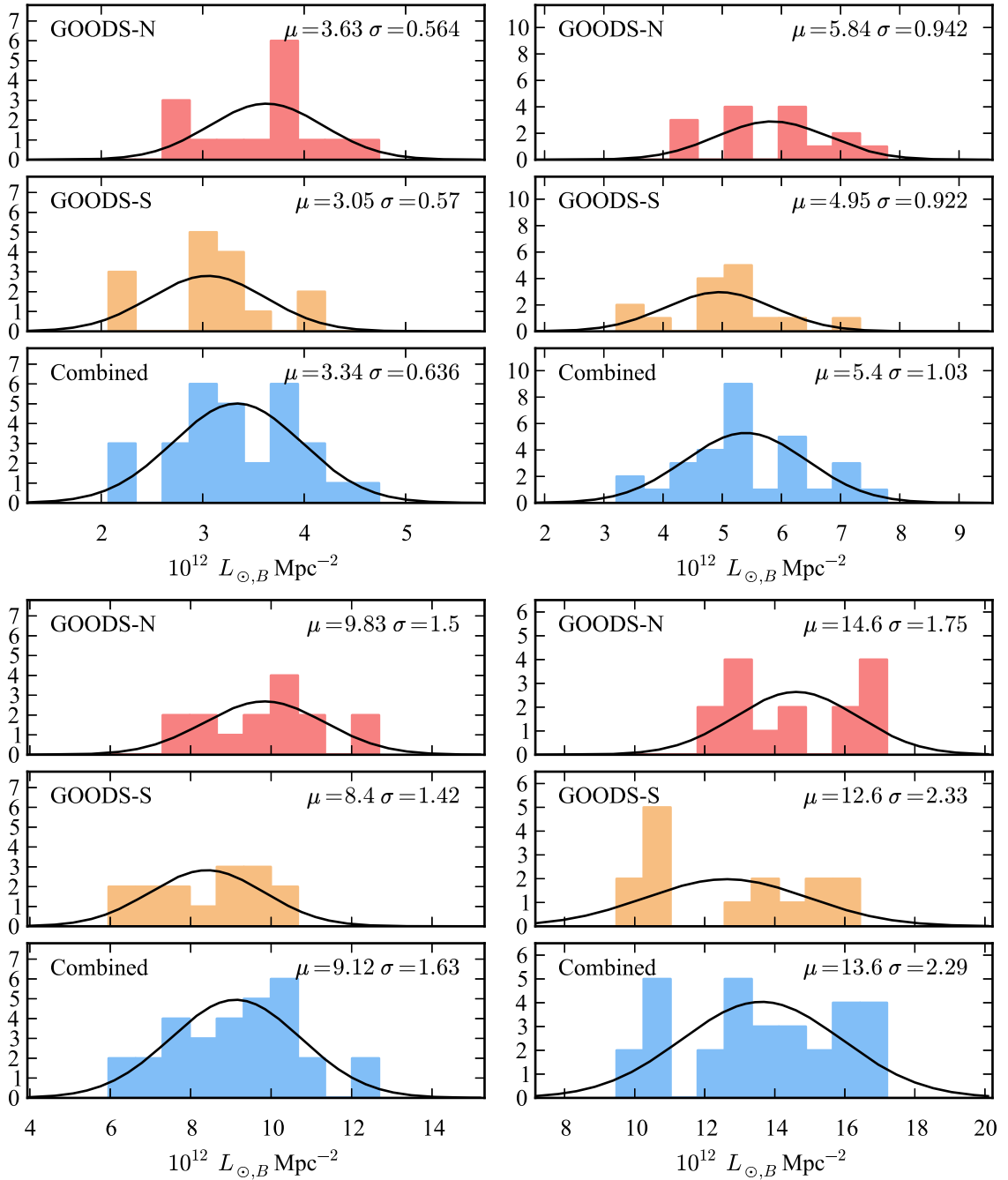
Figure 5.14. Distribution of luminosity density in GOODS fields, with galaxy selection and K-corrections applied for cluster V ($z = 0.91$, *upper left*), cluster S ($z = 1.07$, *upper right*), cluster G ($z = 1.26$, *lower left*), and cluster A ($z = 1.45$, *lower right*).

minosity density of these fields is taken as the "background" luminosity for the cluster, and the standard deviation (typically $15 - 20$ % of the average) is taken as the error in this background luminosity due to variations between fields.

We have implicitly assumed that the GOODS average accurately represents the cosmic average. GOODS incorporates only two widely separated fields. As a result, the average luminosity density may differ from the cosmic average due to variations in large scale structure. As a rough estimate of the cosmic variance, we compare the two GOODS fields. The average luminosity density of the GOODS-North regions is consistently higher than that of the GOODS-South regions by $15 - 20\%$ (Fig. 5.14). This means that the "standard deviation" of these two samples of large scale structure is $\sim 8\%$. We checked this using the cosmic variance calculator made available by Trenti & Stiavelli (2008)[2]. The expected cosmic variance in galaxy number counts in the redshift window $0.7 < z < 1.7$ for one GOODS field is approximately $\sim 6\%$, in good agreement with our naïve estimate. Conservatively, we take 8% as the cosmic variance for one GOODS field. For the *average* of the North and South fields, this implies a cosmic variance of $8\%/\sqrt{2} \sim 6\%$.

One might be additionally concerned that the "background" in the cluster fields is biased higher than the cosmic average because clusters form in regions of large-scale over-densities. However, each cluster field is a "pencil-beam" galaxy survey, so the vast majority of non-cluster galaxies will not be associated with the high-density region in which each cluster formed.

5.4.8 Cluster Luminosity Profiles

Ideally one would measure a two-dimensional luminosity density, $L(x, y)$, for each cluster, as in Equation (5.2). However, the large background makes this difficult. For our purpose (which is to account for variations in control time with radius), it is sufficient to assume the clusters have a circularly symmetric luminosity distribution, $L(r)$. For each cluster, we sum the total luminosity in annuli of width 0.1 Mpc. For nearly all clusters there is a clear overdensity relative to the background out to $r \sim 0.3$ Mpc (Fig. 5.15). Beyond 0.3 Mpc, the luminosity measurement is dominated by background noise for most clusters. This might appear to be a problem; we wish to characterize the cluster luminosities out to $r \gtrsim 0.7$ Mpc, the area over which we searched for SNe. In fact, it is only necessary to accurately measure the *average* luminosity profile over the full area (the denominator of Eq. 5.1 is the sum of the cluster luminosities, weighted by control time). Averaging all 25 clusters, there is a significant measurement of the luminosity profile out to > 0.5 Mpc (Fig. 5.18, left panels), and the average cluster luminosity within $r < 0.6$ Mpc has an error of 12% (statistical only) and $\sim 20\%$ (statistical + cosmic variance), below the Poisson error in the number of SNe detected.

Beyond $r < 0.6$ Mpc, the control time is generally small (that is, there are few observations covering the outskirts of the clusters) and the cluster luminosity density is low,

---

[2]http://casa.colorado.edu/~trenti/CosmicVariance.html
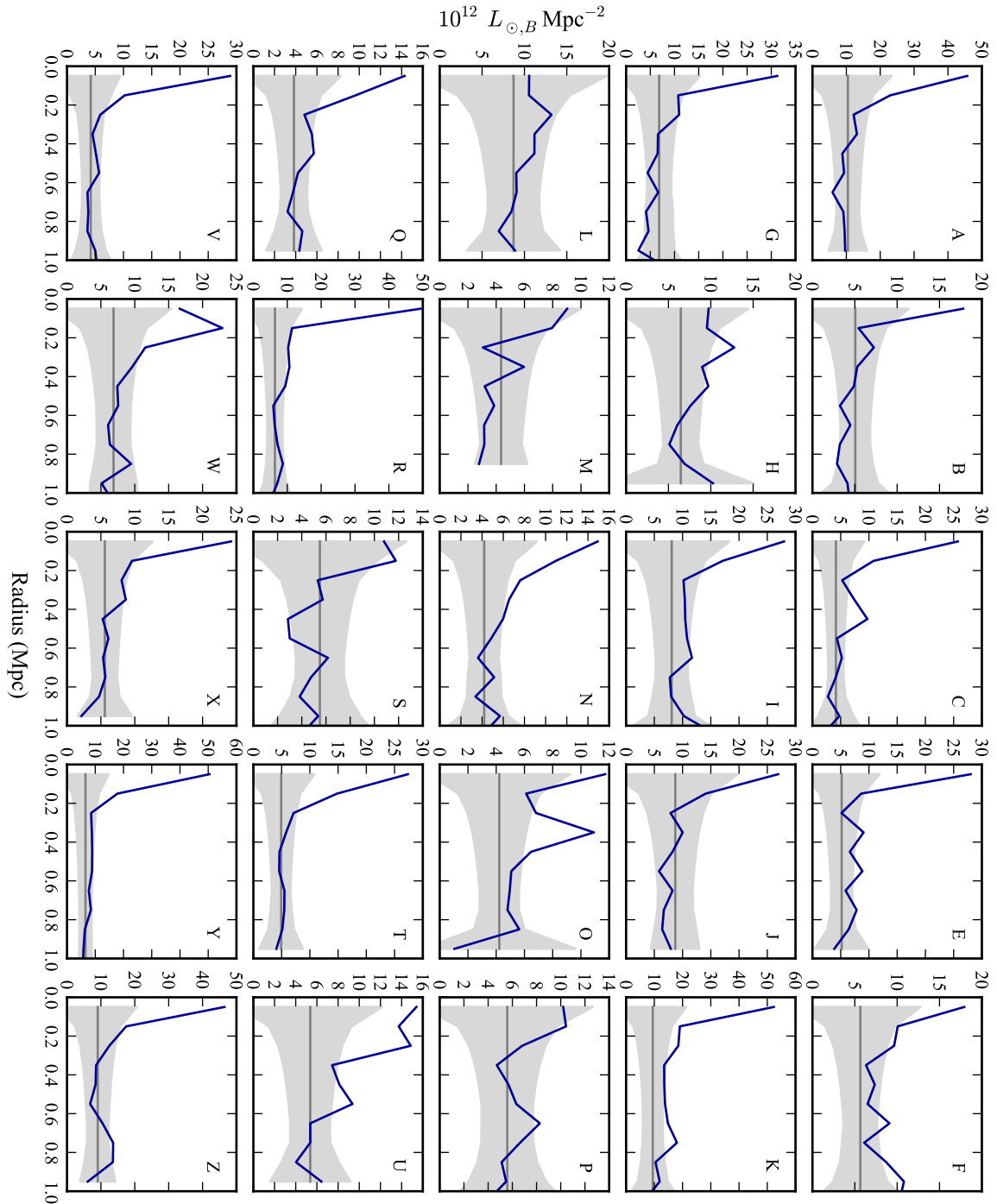
Figure 5.15. Luminosity profiles of all 25 clusters. The grey line and shaded region represents the estimated background luminosity density and uncertainty on the background at each radius. The background uncertainty decreases with radius because larger annuli sample more area. At large radii, the uncertainty increases again because only some parts of the outer annuli (on the deepest part of the image) are used in computing the luminosity.

Figure 5.16. Same as Figure 5.15, but for galaxies on the red sequence only.

Figure 5.17. Same as Figure 5.15, but for *elliptical* galaxies on the red sequence only.

Figure 5.18. Average luminosity profile of the 25 clusters. *Top row:* Average luminosity density in the cluster fields in annuli of width 0.1 Mpc extending out from th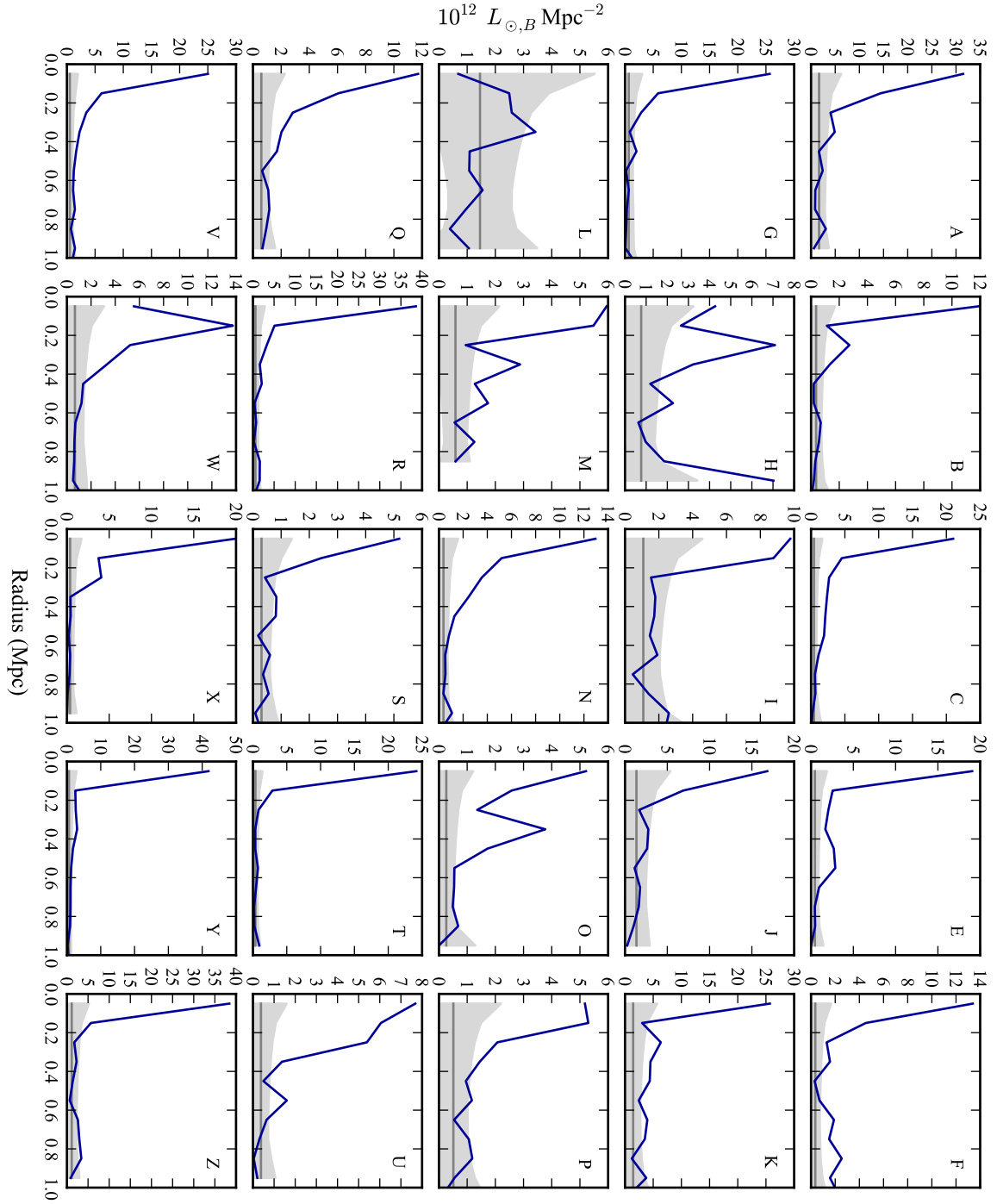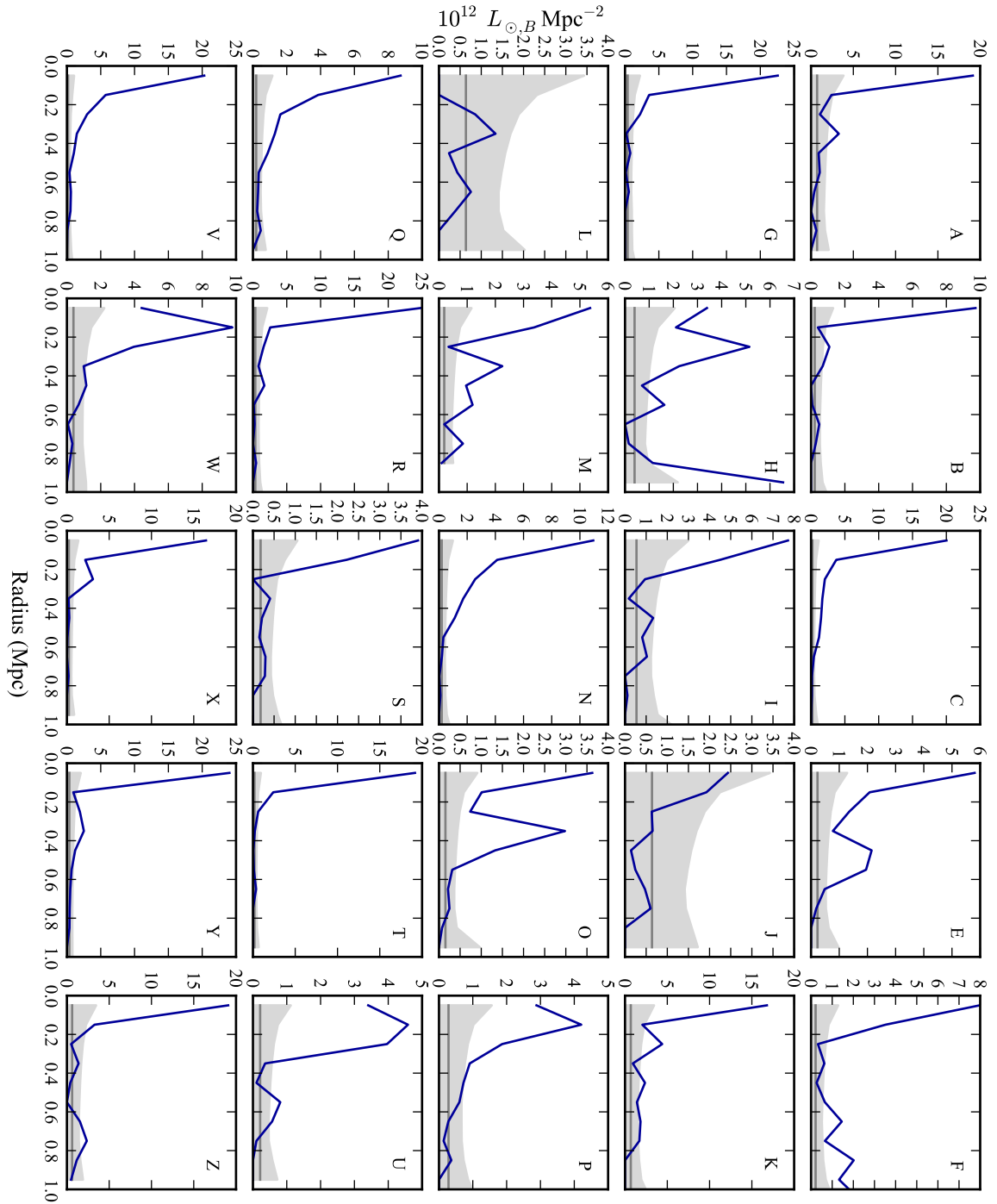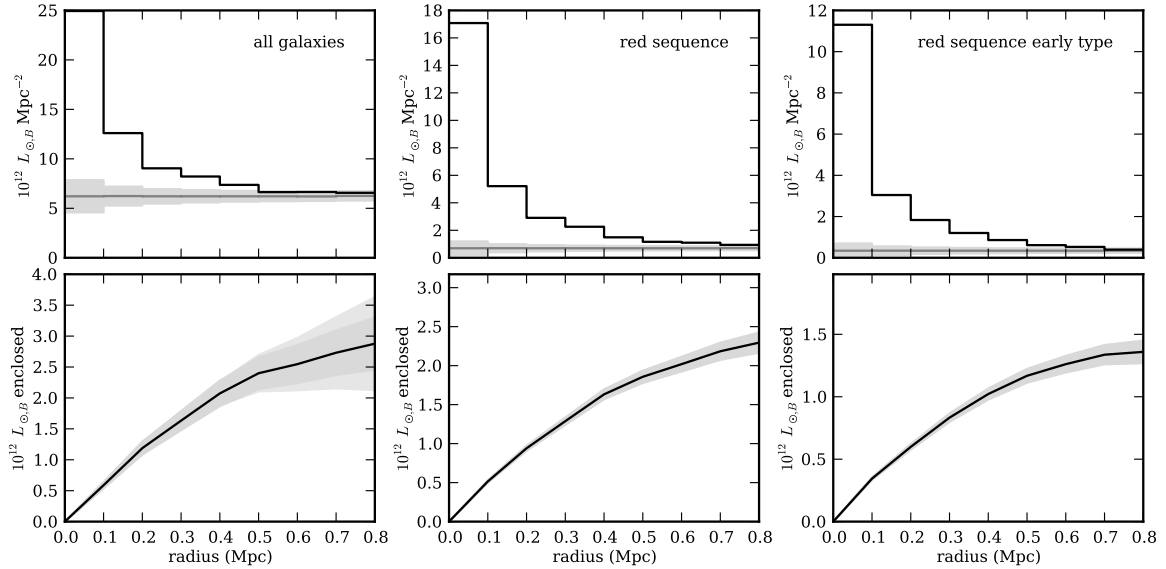e cluster center. The grey line and shaded region show the estimated "background" luminosity in each annulus and the error on that background, respectively. The darker grey region is the statistical-only error, while the light grey is the statistical + cosmic variance error, added in quadrature. *Bottom row:* The total enclosed luminosity as a function of radius, derived by subtracting the background from the total luminosity density in each bin in the top row plot. The *left plots* include galaxies of all colors and morphologies, while the *center plots* include only galaxies with $i_{775} - z_{850}$ colors within ± 0.2 mag of the red sequence in their respective clusters. The *right plots* include only galaxies that satisfy the color requirement and also have $z_{850} < 24$ and are morphologically early type. By excluding bluer galaxies (center and right plots) the background (and error) is reduced dramatically.

meaning that these regions will not contribute greatly to the rate measurement. Still, we include these regions in our rate calculation, using the entirely reasonable prior that the luminosity density is decreasing with radius past $r < 0.6$ Mpc. How rapidly the luminosity density decreases will not have a significant impact on the result, but as a convenient analytic description we fit a β-model of the form

$$L(r) = \frac{\Sigma_0}{(1 + (r/r_{\mathrm{core}})^2)^\beta} \qquad (5.14)$$

over the range $r < 0.6$ Mpc and apply this function at $r > 0.6$ Mpc. The data are well-fit by this model, with best-fit parameters $r_{\mathrm{core}} = 0.074$ Mpc and $\beta = 0.91$. Varying this model luminosity by $\Delta\Sigma_0 = \pm 20\%$ (easily enclosing the allowed range of $L(r)$) only changes our results by $\pm 4\%$. This and other systematic uncertainties are summarized in Table 5.5.

5.4.9 Galaxy Subsets

In addition to measuring the total luminosity of all galaxies in the clusters, we also measure the total luminosity of only red-sequence galaxies and the total luminosity of only

Table 5.3. Average cluster luminosities within $r < 0.6$ Mpc

Subset	N	$\bar{z}$	All galaxies ($10^{12} L_{\odot,B}$)	RS galaxies ($10^{12} L_{\odot,B}$)	RSE galaxies ($10^{12} L_{\odot,B}$)
X-ray	9	1.20	$2.86 \pm 0.54 \pm 0.45$	$2.42 \pm 0.16 \pm 0.05$	$1.47 \pm 0.12 \pm 0.02$
IR-Spitzer	7	1.30	$2.85 \pm 0.70 \pm 0.52$	$1.83 \pm 0.24 \pm 0.07$	$0.96 \pm 0.16 \pm 0.03$
Optical	9	1.00	$1.99 \pm 0.37 \pm 0.32$	$1.75 \pm 0.08 \pm 0.03$	$1.29 \pm 0.06 \pm 0.01$
$z < 1.2$	14	1.02	$2.14 \pm 0.31 \pm 0.33$	$1.79 \pm 0.07 \pm 0.03$	$1.28 \pm 0.05 \pm 0.01$
$z > 1.2$	11	1.32	$3.06 \pm 0.58 \pm 0.54$	$2.31 \pm 0.19 \pm 0.07$	$1.23 \pm 0.14 \pm 0.04$
All	25	1.15	$2.54 \pm 0.31 \pm 0.42$	$2.02 \pm 0.09 \pm 0.05$	$1.26 \pm 0.07 \pm 0.02$

Note. — "RS": galaxies within ± 0.2 mag of the cluster red sequence. "RSE": galaxies fulfilling the "RS" requirement, and also $z_{850} < 24$, and morphologically early-type. The first and second confidence intervals are the statistical error and cosmic variance error, respectively. These luminosities do not include the faint-galaxy correction C.

red-sequence, morphologically early-type galaxies. These measurements enable us to compute the cluster SN Ia rate specifically in these galaxy subsets. For the red-sequence-only measurement we follow the same procedure as above, but eliminate from the analysis all galaxies with $i_{775} - z_{850}$ colors more than 0.2 mag from their respective cluster red sequences (galaxy colors and cluster red sequences are determined as in Meyers et al. 2011). For the red-sequence early-type measurement, we make the same requirement in color, and additionally use the quantitative morphology requirements of Meyers et al. (2011). That analysis uses two parameters, asymmetry and Gini coefficient, to automatically divide galaxies into early- and late-type subsets. Here we require the asymmetry to be < 0.10 and the Gini coefficient to be > 0.40. We also require the galaxies to be $z_{850} < 24$ as the asymmetry and Gini coefficient are somewhat less reliable at fainter magnitudes.

The luminosity profiles for these two subsets are shown in the center and right columns of Figure 5.18. The profiles are broadly consistent with the profile of the full cluster luminosity (left column), but the "subset" profiles are much better measured. This is because by excluding bluer galaxies, we have eliminated much of the background while still retaining the majority of cluster galaxies. The red-sequence subset contains 77% of the luminosity of the full cluster within 0.6 Mpc (Table 5.3). The red-sequence early-type subset has 62% of the light contained in the red-sequence subset. However, keep in mind that in the early-type subset we have excluded $z_{850} > 24$ galaxies, whereas they are included in the red-sequence subset: In fact 68% of $z_{850} > 24$ red-sequence galaxies pass the "early-type" morphology requirements.

Note that our definition of "red-sequence" here is a relatively simple one. It is sufficient to select a subsample of "more red" galaxies for the purpose of looking for a dependence of the SN rate with galaxy color within the cluster. However, for measuring the red fraction in clusters (e.g., the Butcher-Oemler effect Butcher & Oemler 1978, 1984), defining red-sequences with a constant color width for all redshifts is not ideal (Andreon 2006a). The

luminosity content of the subsets are reported above only to give the relative size of each sample.

5.4.10 Stellar Mass-to-Light Ratio

To compare SN rates in clusters of different ages, rate measurements must be normalized by stellar mass rather than stellar luminosity because luminosity changes as stars age. To convert our luminosity measurements to mass measurements we use a mass-to-light (M/L) ratio based on a stellar evolution model. There are several available models in the literature. The choice of stellar tracks, metallicity, star formation history, and in particular the assumed IMF, will all affect the derived M/L ratio to some extent. For the purpose of measuring the change in rate with redshift, it is important to use a *consistent* model and assumptions for determining the M/L ratio for all rate measurements. That is, we are most concerned that the model accurately captures the evolution of stellar luminosity over the redshift range of interest ($0 < z < 1.46$), and less concerned about the overall normalization of the M/L ratio. To that end, for our main result we will use a model and assumptions that match as closely as possible those used for the M/L ratio in low-redshift cluster rate measurements. As we also give results normalized by luminosity, those wishing to use a different M/L ratio can easily do so. Finally, note that the *initial* stellar mass formed is the quantity of interest for normalizing rate measurements. However, as most rate measurements and M/L ratios have been reported in terms of current mass, we give our results in these units and simply note the difference between current and initial mass for the purpose of comparing rate measurements. Thus, in the following paragraphs M refers to current stellar mass.

M/L ratio in low-redshift cluster rate measurements

The lower-redshift cluster rate studies of Sharon et al. (2007), Sharon et al. (2010), and by extension, Dilday et al. (2010b) have used the relations between M/L ratio and galaxy color derived by Bell et al. (2003, hereafter Bell03). For example, Sharon et al. (2007) use the relation $\log_{10}(M/L_z) = -0.052 + 0.923(r - i)$ and Sharon et al. (2010) use $\log_{10}(M/L_g) = -0.499 + 1.519(g - r)$, where M, L_z and L_g are in solar units. In order to use a consistent model, it is important to recognize how these relations were derived. Bell03 fit a grid of PÉGASE2 (Fioc & Rocca-Volmerange 1997) synthetic galaxy spectral energy distributions (SEDs) to actual $ugrizK$ photometry of low-redshift galaxies. The grid covers a range of metallicities and star formation histories. The star formation histories have exponentially-decreasing or -increasing star formation rates, and assume that star formation commenced at $z = 4$. For each galaxy, the M/L ratio is that of the best-fit synthetic galaxy SED, consistently evolved to $z = 0$. Bell03 use a "diet" Salpeter (1955) IMF (following Bell & de Jong 2001). This IMF is defined as having the same colors and luminosity as a Salpeter IMF, but with a total mass 30% lower. The difference in mass is attributed to a smaller number of faint low-mass stars relative to a Salpeter IMF. These stars
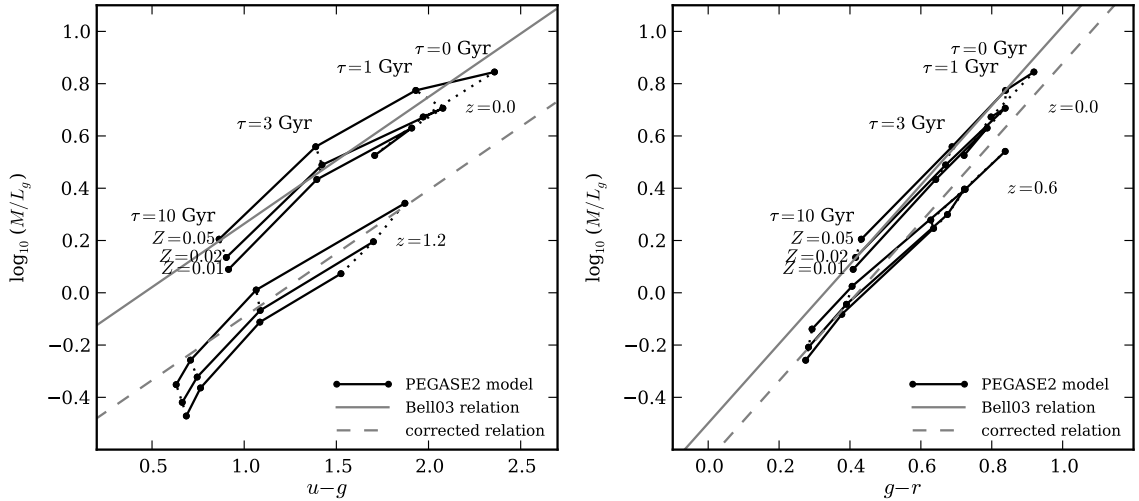
Figure 5.19. Evolution of M/L ratio versus color with redshift. *Left panel:* M/L ratio as a function of $u-g$ color at $z=0$ and at $z=1.2$ (typical redshift in this study). The grid of points show PÉGASE2 models with exponentially-decreasing star formation rates with e-folding times τ and metallicities Z. For each model, star formation begins at $z=4$. Models with constant metallicity are connected by solid black lines and models with identical star formation histories are connected by dotted lines. For example, models with $\tau=0$, corresponding to a simple stellar population, are the rightmost points (corresponding to $Z=0.01$, 0.02, 0.05) connected by dotted lines. As the models are evolved back in time from an observed redshift of $z=0$ to an observed redshift of $z=1.2$, the M/L ratio decreases and moves away from the Bell03 relation (solid grey line). The dashed grey line shows the relation used in this study for $z=1.2$. At $z=1.2$ the offset from the Bell03 relation is -0.36 dex, or a factor of 0.43. *Right panel:* Same as left panel, but for $g-r$ color and for an observed redshift of $z=0.6$, the typical redshift in the rate study of Sharon et al. (2010). The offset here is only -0.14 dex, or a factor of 0.72.

do not contribute significantly to the luminosity of the Salpeter IMF. The diet Salpeter IMF results in M/L ratios 30% lower at a given color than a normal Salpeter IMF. Note that because Bell03 simply take the M/L ratio from the best-fit synthetic SED of each galaxy, the Bell03 relations will generally fall within the grid of M/L versus color covered by the synthetic galaxy SEDs.

M/L **ratio at** $0.9 < z < 1.46$

Ideally, for consistency with Sharon et al. (2007), Sharon et al. (2010) and Dilday et al. (2010b), we would simply use the Bell03 relation for $u - g$ color, which most closely matches our observed color: $\log_{10}(M/L_g) = -0.221 + 0.485(u-g)$. However, the Bell03 relations are based on $ugrizK$ photometry of low-redshift galaxies, corrected for evolution to $z=0$. As such, they are specific to $z=0$ and not directly applicable at high redshift. A stellar population passively evolving from age a few Gyr (at $z\sim1$) to >10 Gyr (at $z=0$) will dim significantly while only growing slightly redder (see, e.g. BC03), in a manner that does not follow the Bell03 relations. To estimate the effect of evolution from their
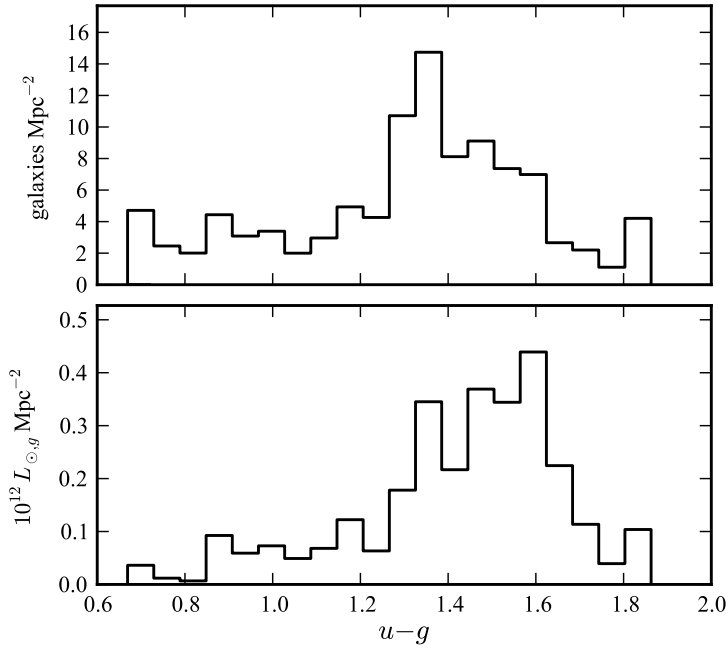
Figure 5.20. Stacked distribution of galaxy rest-frame colors for all 25 clusters. The background (based on the GOODS fields) has been statistically subtracted. Only galaxies within 0.5 Mpc of cluster centers have been included in order to limit variance from the background. The *top panel* shows galaxy density in each color bin, while in the *bottom panel* the distribution is weighted by galaxy luminosity.

$z = 0$ relation to higher redshift, we make a similar grid of PÉGASE2-generated SEDs with the same formation redshift, metallicities, IMF, and star formation histories. As expected, when evaluated at $z = 0$, the M/L ratios of this grid are consistent with the Bell03 relation (Fig. 5.19, left panel, upper grid of black points). Evaluating the SEDs at higher redshifts, we find that the M/L ratios are well fit by a relation with the same slope, but smaller normalization. For example, at $z = 1.2$, the best-fit offset from the $z = 0$ relation is -0.36 dex (Fig. 5.19, left panel, dashed line). At the extremes of the redshift range of interest, the best fit offset is -0.26 dex ($z = 0.9$) and -0.44 dex ($z = 1.46$). We therefore use a M/L ratio of

$$\log_{10}(M/L_g) = \begin{cases} -0.48 + 0.485(u - g), & z = 0.9 \\ -0.66 + 0.485(u - g), & z = 1.46 \end{cases} \tag{5.15}$$

and linearly interpolate for intermediate redshifts. Another way to view Equation (5.15) is that, independently of the relation at $z = 0$, we have fit a linear relation to the PÉGASE2 SEDs at the redshift of each cluster, assuming a slope consistent with Bell03.

Using Equation (5.15) we calculate mass on a galaxy-by-galaxy basis: we K-correct the observed i_{775} and z_{850} magnitude to rest-frame SDSS u and g magnitudes using the method discussed in §5.4.4, and obtain the M/L ratio from the $u - g$ color. In all, 66% of the clusters' luminosity is from galaxies with color in the range $1.3 < u - g < 1.7$, 27% of the luminosity is distributed roughly equally between galaxies in the range $0.6 < u - g < 1.3$, and the remainder is in redder galaxies with $u - g > 1.7$ (Fig. 5.20). Thus, while there is a clear presence of bluer cluster galaxies, the majority of the clusters luminosity is confined to a narrow range in color. This narrow color range means that changes in the assumed

slope of Equation (5.15) will not have a large effect on the resulting total mass.

The cumulative M/L ratio (the ratio of the total mass of all 25 clusters to the total luminosity of all 25 clusters) is $M/L_g = 1.25$ (see Table 5.4, "denom"). For red-sequence galaxies only, the ratio is higher ($M/L_g = 1.38$) due to the exclusion of bluer galaxies with a lower inferred M/L ratio.

M/L **ratio uncertainty**

As noted above, we are primarily concerned with the accuracy of the evolution in the stellar mass and luminosity over the range $0 < z < 1.46$, rather than the accuracy of the absolute M/L ratio. As a cross-check of the M/L ratio evolution, we have compared the above results (using PÉGASE2) to the results obtained with the BC03 SEDs. We use the standard Padova 1994 evolution and the same star formation histories as above. In terms of evolution offset from $z = 0$ to $z \sim 1.2$, we find results consistent within 0.03 dex.

This consistent evolution in BC03 and PÉGASE2 is encouraging. However, to be much more conservative in our estimate of the uncertainty in the M/L ratio evolution, we take the scatter of the models around the best-fit line as our uncertainty. In Figure 5.19, in the color range of interest, the scatter is approximately ± 0.08 dex (20%) at both low and high redshift. We use this as the systematic uncertainty in the M/L ratio for the purpose of comparing SN rates at low and high redshift in §5.6.3 and §5.6.4. The uncertainty in the absolute M/L ratio is much greater, due mainly to the uncertainty in the true IMF.

5.5   Results and Systematic Uncertainty

Here we present our results for the full cluster rate and for two galaxy subsets (§5.5.1) and summarize contributions to the uncertainty (§5.5.2) in each. In §5.5.3 we show that the rate result in the subsets are not sensitive to the specific parameters used to select the subset.

5.5.1   Results

The results are presented in Table 5.4. We derive a rate in the full cluster, in red-sequence galaxies only, and in red-sequence early-type galaxies only. Each subset includes a different number of SNe: We have discovered 8 ± 1 cluster SNe, where the quoted uncertainty is due to classification uncertainty (including uncertainty in both SN type and cluster membership). Limiting the sample to only SNe discovered in galaxies included in the red-sequence subset excludes SN SCP06F12 and SN SCP06C1, leaving 6.5 ± 0.5 cluster SNe Ia. The uncertainty here comes from the uncertainty in the cluster membership and type of SN SCP06E12, which we count 0.5 ± 0.5 cluster SNe Ia. Further limiting the sample to only SNe discovered in galaxies included in the red-sequence early-type subset, SN SCP06E12 is eliminated as its host galaxy is dimmer than the $z_{850} = 24$ cutoff used

Table 5.4. Results: cluster SN Ia rate

Environment	Unit	$\bar{z}$	$N_{\text{SN Ia}}$	Denom	Rate	(stat)	(sys)
Full cluster	SNuB	1.14	8.0 ± 1.0	15.87	0.50	$+0.23$ -0.19	$+0.10$ -0.09
Full cluster	SNug	...	...	15.96	0.50	$+0.23$ -0.19	$+0.10$ -0.09
Full cluster	SNuM	...	...	22.41	0.36	$+0.16$ -0.13	$+0.07$ -0.07
Red-sequence	SNuB	1.13	6.5 ± 0.5	11.95	0.54	$+0.25$ -0.19	$+0.07$ -0.07
Red-sequence	SNug	...	...	12.20	0.53	$+0.24$ -0.19	$+0.07$ -0.07
Red-sequence	SNuM	...	...	17.61	0.37	$+0.17$ -0.13	$+0.05$ -0.05
Red-sequence early-type	SNuB	1.10	6.0 ± 0.0	7.29	0.82	$+0.39$ -0.30	$+0.09$ -0.08
Red-sequence early-type	SNug	...	...	7.59	0.79	$+0.38$ -0.29	$+0.09$ -0.08
Red-sequence early-type	SNuM	...	...	11.77	0.51	$+0.24$ -0.19	$+0.06$ -0.05

Note. — "Denom" is the denominator of equation (5.1) and has units of $10^{12} L_{\odot,B}$ years, $10^{12} L_{\odot,g}$ years and $10^{12} M_{\odot}$ years for rate units of SNuB, SNug and SNuM respectively.

for this subset leaving 6 SNe Ia with negligible classification error. The number of SNe Ia discovered in each subset, including classification error, is summarized in Table 5.4 under $N_{\text{SN Ia}}$.

We normalize the rate in three different ways: by B-band luminosity, by g-band luminosity, and by stellar mass. For each cluster, we use the visibility time map $T(x,y)$ (e.g., Fig. 5.3) and the measured luminosity (or mass) profile to carry out the integral in equation (5.2) giving the time-luminosity searched. The sum of these values for all 25 clusters is the denominator of equation (5.1), the total time-luminosity searched in all clusters. This is shown in Table 5.4 under "Denom" for each sample. The rate is simply $N_{\text{SN Ia}}$ divided by "denom," as in equation (5.1). The contributions to the statistical and systematic errors are summarized in Table 5.5.

The weighted-average redshift, $\bar{z}$, for each subsample is given by

$$\bar{z} = \frac{\sum_i z_i \int_{x,y} T_i(x,y) L_i(x,y)}{\sum_i \int_{x,y} T_i(x,y) L_i(x,y)}, \tag{5.16}$$

where z_i, L_i and T_i are the redshift, luminosity and effective visibility time of the i-th cluster, respectively. The weighted-average redshift is slightly smaller for the red-sequence and red-sequence early-type galaxy subsets. This is because in the higher-redshift clusters, a smaller fraction of galaxies meet the subset requirements (see $z < 1.2$ versus $z > 1.2$ average cluster luminosity in Table 5.3).

5.5.2 Summary of Systematic Uncertainties

Throughout the paper, we have highlighted and addressed possible sources of systematic uncertainty. Here we summarize these sources. In Table 5.5 we show the relative contribution of each to the total systematic error, and compare to sources of statistical error.

Table 5.5. Sources of uncertainty in cluster SN Ia rate

Source of error	Full cluster (%)	Red-sequence (%)	Red-sequence early-type (%)
Statistical			
Poisson	$^{+40}_{-32}$	$^{+45}_{-35}$	$^{+47}_{-36}$
Luminosity (stat)	± 12	± 6	± 6
Luminosity (cosmic var.)	± 16	± 4	± 3
Total statistical	$^{+45}_{-38}$	$^{+46}_{-35}$	$^{+48}_{-37}$
Systematic			
SN type classification	± 13	± 8	$\ldots$
Control time: varying M_B	$^{+8}_{-6}$	$^{+8}_{-6}$	$^{+8}_{-6}$
Control time: dust distribution	$^{+10}_{-2}$	$\ldots$	$\ldots$
Luminosity: MAG_AUTO corr.	± 7	± 7	± 7
Luminosity: K-correction	± 3	± 3	± 3
Luminosity: Faint galaxy corr.	$^{+4}_{-9}$	$\ldots$	$\ldots$
Luminosity: $r > 0.6(0.8)$ Mpc	± 4	± 1	± 1
Total systematic	$^{+20}_{-19}$	$^{+14}_{-12}$	$^{+11}_{-10}$
Total statistical + systematic	$^{+49}_{-42}$	$^{+48}_{-37}$	$^{+49}_{-38}$

(1) *SN type classification:* The uncertainty in the number of SNe observed in each galaxy subset was addressed in §5.5.1. The fractional error in the rate is simply the fractional error in the number observed.

(2) *Control time: Varying M_B:* In our control time simulations, we assumed a distribution of SN Ia light curve shapes and absolute magnitudes. To first order, the impact of these assumptions on the control time is captured by varying the assumed SN Ia absolute magnitude (§5.3.3). Variations of ± 0.2 mag resulted in a rate change of $^{+8}_{-6}\%$

(3) *Control time: dust distribution:* In §5.3.3 we assessed the impact of varying amounts of dust extinction on the control time. Assuming an unrealistically large amount of dust-affected SNe decreased the control time by 9% (increasing the SN rate by 10%), while decreasing the amount of dust-affected SNe increased the control time by 2% (decreasing the SN rate by 2%). We do not apply this systematic error to the red-sequence or red-sequence early-type subsets, as we have independent evidence that the amount of dust is limited in these environments.

(4) *MAG_AUTO correction:* In computing the total z_{850} luminosity of each galaxy, we made a correction to the MAG_AUTO magnitude ranging from $\sim 10\%$ at $z_{850} = 20$ to $\sim 30\%$ at $z_{850} = 25$. Varying the range of n used in the simulation by ± 1 affects the correction by $\pm 7\%$.

(5) *K-correction:* In §5.4.4, we noted that the scatter of BC03 templates about the best-fit K-correction is typically less than 0.03 mag. We use this value as the systematic error

on the K-correction.

(6) *Faint galaxy correction:* The average correction C reported in Table 5.2 is 1.054. Varying M_B^* by $\pm$ 0.5 magnitudes results in an average correction of 1.032 and 1.092 for -0.5 and $+0.5$ magnitudes, respectively. Varying α by ± 0.2 results in an average correction of 1.027 and 1.098 for $\alpha = -0.7$ and -1.1, respectively. Concurrently varying M_B^* and α within the same ranges results in a minimum average correction of 1.015 ($M_B^* = -22.2$, $\alpha = -0.7$) and a maximum average correction of 1.154 ($M_B^* = -21.2$, $\alpha = -1.1$). Conservatively, we assign $^{+4\%}_{-9\%}$ as the systematic error on the rate associated with this correction. This error is not applied to the red-sequence or red-sequence early-type subsets because these subsets do not include light from galaxies below the detection threshold.

(7) *Luminosity at large radii:* In §5.4.8 we assumed a model for the cluster luminosity profile at $r > 0.6$ Mpc (0.8 Mpc for red-sequence and red-sequence early-type subsets). Varying the model luminosity by $\pm 20\%$ resulted in a $\pm 4\%$ change in the full cluster rate. The change is much smaller ($\pm 1\%$) for the red galaxy subsets because the model is only used at $r > 0.8$ Mpc.

(8) M/L *ratio:* In §5.4.10 we used a M/L ratio to translate stellar luminosity to stellar mass. Rather than estimating the absolute uncertainty in the M/L ratio (which is strongly dependent on assumptions), we estimated the uncertainty in the *evolution* of the M/L ratio from low to high redshift. This is the relevant uncertainty for comparing rates at different redshifts in order to derive the SN Ia delay time distribution. We defer discussion of this uncertainty to §5.6.4 where we discuss uncertainties in the DTD.

5.5.3 Effect of Varying Subset Requirements

In selecting our red-sequence and red-sequence early-type galaxy subsamples, we required red-sequence galaxies to be within ± 0.2 mag of the color of their cluster red sequence. For early-type galaxies, we required the asymmetry parameter to be < 0.1 and the Gini coefficient to be > 0.40. It is interesting to test the sensitivity of the results to variations in the requirements. In Figures 5.21 and 5.22 we vary the requirements and observe the effect on the rates. As requirements are made more strict (for example, narrowing the red sequence) the total mass of the sample decreases. At the same time, SNe fall out of the sample when their host galaxies are cut. The Poisson error increases as the number of included SNe shrinks.

There is not a strong dependence of the SN Ia rate with galaxy color residual from the red sequence (Fig. 5.21). Even in cluster galaxies that lie in a tight range around the red-sequence (± 0.08 mag), we find a SN Ia rate consistent with the full cluster rate. Similarly, there is no significant rate trend with the purity of the early-type sample (Fig. 5.22). We happened to pick morphology requirements that yield a slightly higher rate than other choices, but such variations are expected with small-number statistics and are accounted for by the Poisson uncertainty in the result (Tables 5.4 and 5.5). Even in the most-selective subset ($\Delta = -0.04$), the rate is consistent with the full cluster rate.
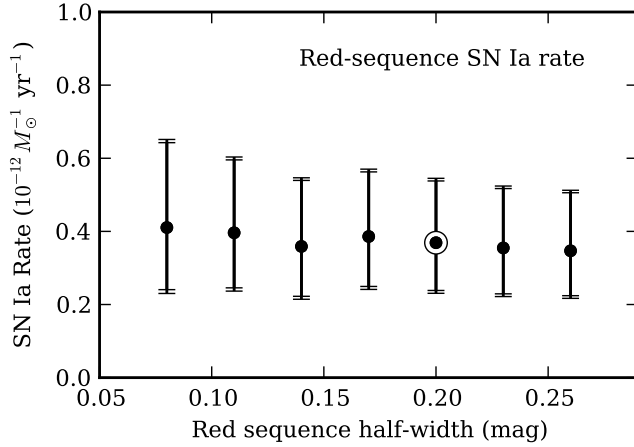
Figure 5.21. The effect of varying the width of the red sequence on the red-sequence-only rate. The nominal red-sequence rate result corresponds to a half-width of 0.20 mag. The inner and outer error bars represent the statistical and total uncertainty, respectively.
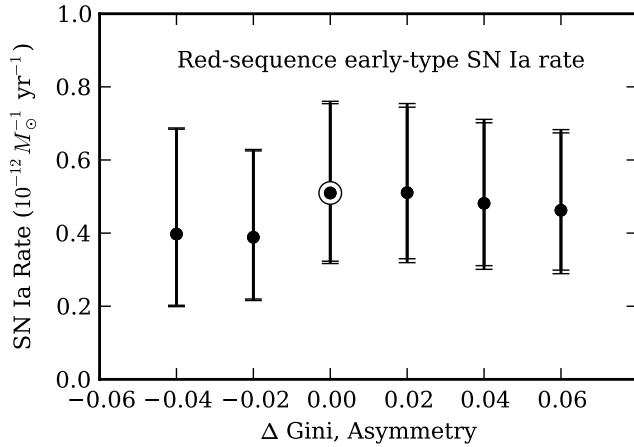

Figure 5.22. The effect of varying the morphology parameter requirements. Negative Δ values correspond to a more strict selection and a higher-purity early-type galaxy sample. The requirements are asymmetry $< 0.1 + \Delta$ and Gini coefficient $> 0.40 - \Delta$. The nominal red-sequence early-type rate corresponds to $\Delta = 0$. The red-sequence half-width is fixed at 0.2 mag. The inner and outer error bars represent the statistical and total uncertainty, respectively.

5.6 Discussion

5.6.1 Host-less Cluster SNe Ia

As reported in Dawson et al. (2009), we have discovered one potential host-less cluster SN Ia among the 8 ± 1 cluster SNe Ia. SN SCP06C1 is projected near two possible host galaxies: A $z_{850} = 21.6$ spiral galaxy $1''.1$ West of the SN, and a significantly fainter $z_{850} = 24.6$ galaxy $0''.45$ (~ 3.5 kpc at the cluster redshift) Northeast of the SN (See Fig. 5.23).

The galaxy-subtracted SN spectrum clearly shows a SN Ia at redshift $z = 0.98$ near maximum light, consistent with the light curve fit. The redshift of $z = 0.98 \pm 0.01$ is consistent with the cluster redshift of 0.974. The bright spiral galaxy is actually in the background of the cluster, at $z = 1.091$. Strong [OII] emission is visible in the spectrum, along with Ca H & K and Hδ absorption. Unfortunately, the small separation between the main galaxy and the smaller galaxy to the Northeast means that the spectrum of the smaller galaxy is dominated by light from the larger galaxy, making it impossible to assess
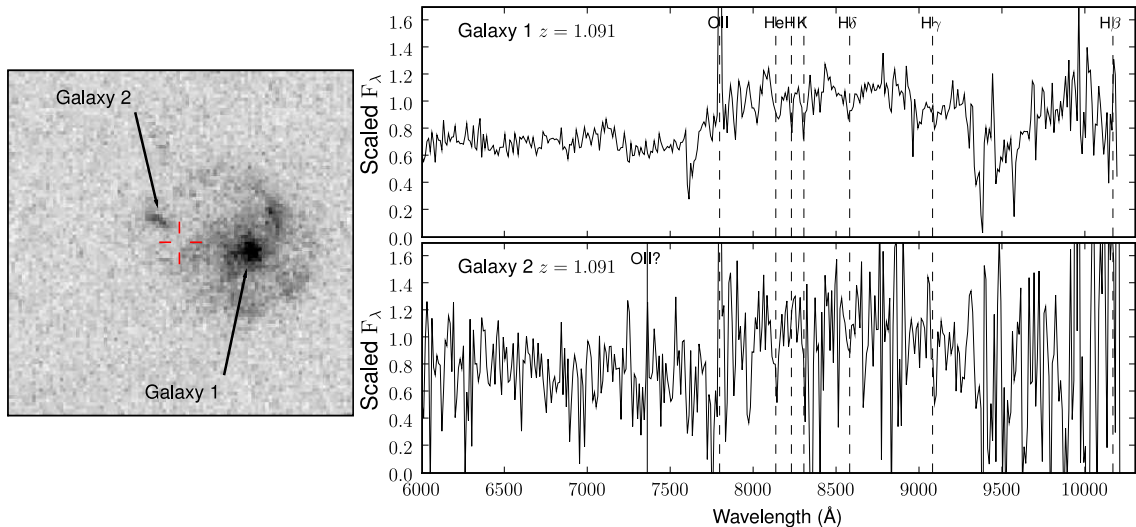
Figure 5.23. The environment of SN SCP06C1, a possible intra-cluster SN Ia. The red marks show the position of the SN, which has a spectroscopic redshift of $z = 0.98$, consistent with the cluster redshift. The large nearby galaxy ("Galaxy 1") is at $z = 1.091$, behind the cluster. The spectrum of the small nearby galaxy ("Galaxy 2") is dominated by light from the larger galaxy – the separation between the two galaxies is only $1''.5$. If Galaxy 2 were located at the cluster redshift, [OII] would be located at the position indicated by "OII?"

a redshift. It is thus possible that the small galaxy is at the cluster redshift and is the actual host of the SN. Alternatively, the small galaxy might be at the same redshift as the larger galaxy and physically associated with it (either as a satellite galaxy or as part of the spiral structure of the galaxy). It is interesting to note that the SN is only $20''$ (160 kpc) projected radius from the center of the cluster, perhaps giving more weight to the hypothesis that it is associated with a diffuse intracluster stellar component.

Not being able to confirm or reject this SN as host-less, we have an upper limit of one host-less SN out of a total of 8 ± 1. Discovering one host-less SNe Ia out of seven total would imply an intrinsic host-less SN Ia fraction of $14\%^{+18\%}_{-7\%}$ (binomial 68% confidence intervals), and a 95% upper limit of $< 47\%$. This is broadly consistent with host-less SN Ia constraints at intermediate redshifts (Sharon et al. 2010) and at low redshift (Gal-Yam et al. 2003; Sand et al. 2011). At low redshift it has been possible to confirm the host-less nature of some SNe using deeper follow-up imaging, leading to better constraints. The upper limit of $< 47\%$ is also consistent with direct measurements of intracluster light at low redshift, but does not strongly constrain evolution. A sample twice the size or larger, with deeper follow-up to confirm host-less SNe Ia would begin to place interesting constraints on hypotheses for the formation of the intracluster stellar component from $z > 1$ to today.

5.6.2 Comparison to Other Cluster Rate Measurements

Cluster SN Ia rates have been reported at lower redshifts by several groups. In nearby ($z \lesssim 0.2$) clusters, measurements include those of Sharon et al. (2007) at $z \sim 0.14$, Mannucci et al. (2008) at $z \sim 0.02$, and Dilday et al. (2010b) at $z \sim 0.09$ and $z \sim 0.22$. At intermediate redshifts, Sharon et al. (2010) recently reported the rate in $0.5 < z < 0.9$ clusters (median $z \sim 0.6$). At higher redshifts, Gal-Yam et al. (2002) placed the first constraints on the $z \gtrsim 0.8$ cluster rate using a sample of three clusters at $z = 0.83$, 0.89 and $z = 1.27$. However, their SN sample included only one firm SN Ia at $z = 0.83$. The resulting rate has correspondingly large uncertainties and essentially places only an upper limit on the $z > 0.9$ cluster rate. Our result is thus a large step forward in the measurement of the SN rate in the highest-redshift clusters.

In Figure 5.24 we compare our full cluster rate to the lower-redshift rate measurements that have been normalized by stellar mass, permitting a comparison across redshifts. Here we have made an adjustment to the value reported by Sharon et al. (2010). Sharon et al. used the mass-to-light ratio of Bell03 for the SDSS g and r bands, but did not apply a correction for evolution between $z \sim 0.6$ and $z = 0$. Using the method described in §5.4.10 we find that a -0.14 dex offset should be applied to the mass to account for evolution from $z = 0.6$ to $z = 0$ (Fig. 5.19, right panel). We therefore adjust the reported rate of Sharon et al. upward by 0.14 dex (38%). The rate compilation of Maoz et al. (2010) reflects this adjustment. Whereas the adjusted Sharon et al. rate shows an indication that the cluster rate is increasing with redshift, for the first time we find an increasing rate with high significance ($> 2\sigma$).

We point out that the popular "$A + B$" model (Scannapieco & Bildsten 2005) is insufficient for describing the change in cluster rate with redshift. In the $A + B$ model the SN rate is the sum of a term proportional to the total stellar mass and a term proportional to the recent star formation rate: $\mathcal{R}_{\mathrm{SN\ Ia}} = AM_* + B\dot{M}_*$. This simple model is convenient for predicting the SN rate in environments with varying amounts of recent star formation as it accounts for the increased SN Ia rate at short delay times. (In fact, we use this model in Meyers et al. 2011, to derive limits on the expected ratio of SNe Ia to SNe CC in early-type galaxies.) However, the model lacks theoretical motivation and breaks down in other situations. For example, Greggio et al. (2008) note that it cannot adequately describe the observed contribution from SNe with intermediate delay times (e.g., Totani et al. 2008). This point is reinforced by the observation of a changing cluster rate with redshift: In clusters, the A component is dominant at all redshifts observed. As M_* is not changing significantly with redshift, the rate would be expected to remain constant under this model. Instead, we require a DTD model wherein the rate decreases at large delay times (as it does in most theoretically motivated models).
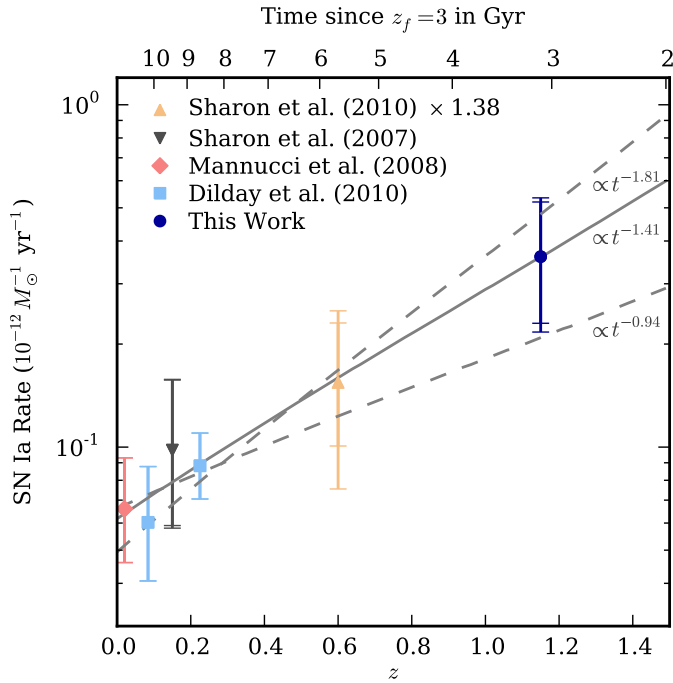
Figure 5.24. Cluster rate measurements (all galaxy types) from this work and the literature. The rate of **Sharon** et al. (2010) shown has been adjusted upward by 38% from the reported rate (see text). The top axis shows the time elapsed since an assumed cluster formation redshift of $z_f = 3$. The solid grey line represents the SN Ia rate for the best-fit power-law DTD: $\mathcal{R}_{\mathrm{SN\ Ia}}(t) = \Psi(t)/m(t)$, where $\Psi(t) \propto t^s$. The dotted grey lines show the range of 1σ error on s.

5.6.3   The Cluster SN Ia Delay Time Distribution

The cluster rates constrain the SN Ia delay time distribution, $\Psi(t)$, over the range of delay times from a few Gyr to ~ 10 Gyr. To illustrate the cluster rate constraints, we parameterize the DTD with a power law in time: $\Psi(t) \propto t^s$. A power law is not only a convenient parameterization in the face of limited data, but is a theoretically motivated function for the DD scenario, where the late-time ($t \gtrsim 1$ Gyr) DTD shape is set by the distribution of WD separation after the second CE phase and the merger timescale due to gravitational radiation (Greggio 2005).

We make the approximation that all clusters formed in a single burst of star formation at $z_f = 3$ and that the age of the stellar population therefore corresponds to the elapsed time from z_f to the cluster redshift (Fig. 5.24, top axis). While clearly a simplification, a single star-formation burst captures the idea that the timescale over which star formation occurred in cluster early-type galaxies is short compared to the time since star formation ceased. The assumed burst redshift $z_f = 3$ is consistent with measurements of cluster early-type galaxies showing that star formation was mostly completed by this redshift (e.g., Gobat et al. 2008). Below, we show that the derived DTD is relatively insensitive to the redshift assumed.

The DTD is normalized by *initial* stellar mass, whereas the cluster rate measurements (including ours, for consistency) have been normalized by *current* stellar mass. The DTD, $\Psi(t)$, is therefore related to the cluster rate by $\Psi(t) = m(t)\mathcal{R}_{\mathrm{SN\ Ia}}(t)$ where $m(t)$ is the fraction of stellar mass remaining at time t after the star formation burst. The specific

choice of $m(t)$ does not have a significant impact on the derived DTD: regardless of the model or IMF assumed, the stellar mass declines by only $\sim 10\%$ over the age range of interest, ~ 3 to 11 Gyr. For consistency with Maoz et al. (2010), we use the remaining stellar mass fraction tabulated by BC03, $m_{\mathrm{BC03}}(t)$, but corrected to $m(t) = 1 - (1 - m_{\mathrm{BC03}}(t))/0.7$ to effectively convert from the Salpeter IMF used in BC03 to a "diet" Salpeter IMF. This correction has only a very small effect on the result (see below).

We find a best-fit value of

$$s = -1.41^{+0.47}_{-0.40}, \tag{5.17}$$

using the statistical+systematic error (added in quadrature) reported for each rate measurement. In Figure 5.24, the solid grey line shows the best-fit cluster rate for this value: $\mathcal{R}_{\mathrm{SN\ Ia}}(t) = \Psi(t)/m(t)$, where $\Psi(t) \propto t^{-1.41}$. Note that the χ^2 of the best-fit model is surprisingly small: 0.40 for 4 degrees of freedom. The *a priori* probability of finding a χ^2 smaller than 0.40 is less than 2%. This is difficult to understand given that the measurement errors are generally dominated by Poisson noise in the number of SNe observed and are thus unlikely to be overestimated.

The best-fit value is consistent with measurements of the late-time DTD in the field (Totani et al. 2008). Most predictions for the SD scenario show a steeper late-time DTD (Greggio 2005; Ruiter et al. 2009; Mennekens et al. 2010) with an effective value for s ranging from $s \sim -1.6$ (Greggio 2005) to $s < -3$ (Mennekens et al. 2010), depending on the details of the scenario and binary evolution. However, some groups have found that the SD scenario could be consistent with a less-steep DTD ($s \sim -1$) given the right combination of main sequence and red giant secondaries (Hachisu et al. 2008). In the DD scenario, the predicted shape of the DTD depends on the distribution of binary separations after the common envelope phase of the WDs, a difficult distribution to predict. However, a slope of $s = -1.4$ (and a range of similar values) would not be surprising in the DD scenario.

5.6.4   Additional DTD Systematic Uncertainties

Variations in the assumed cluster star formation, initial mass normalization and mass-to-light ratio evolution have a small affect on s compared to the measurement error.

(1) *Age of clusters' stellar populations:* Above, we assumed a single burst of star formation at $z_f = 3$. Moving this single burst to $z_f = 4$ results in $s = -1.55$. A more recent burst, $z_f = 2.5$, results in $s = -1.30$. Maoz et al. (2010) give a treatment of variations from the single-burst approximation, also finding that the affect on s is small.

Our rate measurements in red and early-type galaxies provide a good consistency check that recent star formation does not significantly contribute to the SN Ia rate: if it did, we would observe a higher rate in the full cluster than in these subsamples. Surprisingly, we observe the opposite trend (although the significance is low). The red-sequence early-type subsample includes 53% of the stellar mass of the full cluster sample, and 6 SNe Ia. The remaining 47% of the full cluster sample (which includes bluer galaxies and late-type red-

sequence galaxies) accounts for only 2 ± 1 SNe Ia. At low redshift, Mannucci et al. (2008) found a similar trend between E/S0 galaxies and S0a/b galaxies within 0.5 Mpc of cluster centers, though also at $< 1\sigma$ significance.

(2) *Remaining stellar mass:* Whereas the DTD is normalized by initial stellar mass and cluster rate measurements have been normalized by current stellar mass, we have assumed a remaining stellar mass fraction $m(t)$ to convert from current to initial stellar mass. Although different models and IMFs can yield significantly different $m(t)$, we are only concerned here with the change in $m(t)$ between ~ 3 Gyr and at ~ 11 Gyr. (The absolute value of $m(t)$ affects only the normalization of $\Psi(t)$, with which we are not concerned.) Fortunately, the evolution in $m(t)$ in this age range is small and consistent between models, and so the effect on s is small. For example, using $m_{\mathrm{BC03}}(t)$ (assuming a Salpeter IMF) rather than correcting to a diet Salpeter IMF (as we have done) only changes the best-fit value from $s = -1.41$ to $s = -1.38$.

If in §5.4.10 we had used a M/L ratio directly normalized by initial mass, rather than normalizing by current mass and later converting to initial mass, the results would be very similar. (We have not done this for consistency with other rate measurements.) In the PÉGASE2 models in Figure 5.19 (left panel) evaluated at $z = 1.2$, the ratio of current to formed stellar mass varies slightly across the models, but is fully contained in the range 0.66 ± 0.03. The same models evaluated at $z = 0$ have a ratio of 0.59 ± 0.03. This is consistent with the $\sim 10\%$ evolution in $m(t)$ over this range as tabulated by BC03.

(3) M/L *ratio evolution:* While the overall normalization of the M/L ratio will only affect the normalization of $\Psi(t)$ and not s, the evolution of the M/L ratio will affect s. In §5.4.10 we assigned a liberal 20% systematic uncertainty to the evolution of the M/L ratio over the redshift range of interest. To estimate the effect of this systematic uncertainty, we adjust our rate measurement by 20% and that of Sharon et al. (2010) by 10% and refit s. The resulting change in s for positive and negative shifts is -0.15 and $+0.18$ respectively, less than half of the nominal error in s.

CHAPTER 6

Field Rate

6.1 Calculation Overview

We calculate the SN Ia rate in redshift bins using what has become a standard method in rate calculations: The number of SNe Ia per unit time per comoving volume is estimated in the redshift bin $z_1 < z < z_2$ by

$$\mathcal{R}(z_1 < z < z_2) = \frac{N_{\text{SN Ia}}(z_1 < z < z_2)}{\int_{z_1}^{z_2} T(z)\frac{1}{1+z}\frac{\Theta}{4\pi}\frac{dV}{dz}(z)dz} \tag{6.1}$$

where $N_{\text{SN Ia}}(z_1 < z < z_2)$ is the number of SNe Ia discovered between redshifts z_1 and z_2, and the denominator is the total effective time-volume for which the survey is sensitive to SNe Ia in the redshift range $z_1 < z < z_2$. $T(z)$ is the *effective visibility time* (also known as the "control time") and is calculated by integrating the probability of detecting a SN Ia as a function of time over the active time of the survey. $T(z)$ depends on the dates and depths of observations, as well as the specific requirements for selecting SNe. The factor of $1/(1+z)$ converts from observer-frame time to rest-frame time at redshift z. The last two terms in the denominator represent the volume comoving element between z and $z + dz$ observed in the survey. $\frac{dV}{dz}(z)$ is the comoving volume of a spherical shell of width dz. Θ is the solid angle observed in the survey, in units of steradians. ($\Theta/4\pi$ is the fraction of the spherical shell we have observed.) Finally, the average redshift of the bin, weighted by the volume effectively observed, is given by

$$\bar{z} = \frac{\int_{z_1}^{z_2} zT(z)\frac{1}{1+z}\frac{dV}{dz}(z)dz}{\int_{z_1}^{z_2} T(z)\frac{1}{1+z}\frac{dV}{dz}(z)dz}. \tag{6.2}$$

6.2 Field SN Candidates

For $N_{\text{SN Ia}}$ we use the SN selection from Chapter 4 (the non-cluster-members in Table 4.2) with two additional selections not used in the cluster rate analysis:

(1) First, we eliminate candidates that could only be consistent with a SN Ia if it peaked prior to 10 rest-frame days before the first observation. We found that lower-redshift ($z \lesssim 0.9$) SNe were detectable even when peaking well before the first observation, but that such SNe were extremely difficult to type as they were observed only far into the light curve decline. We found it most "fair" to eliminate such candidates entirely. We include the same selection in our efficiency simulations below. This selection affects candidates SCP06L21 and SCP05N10. This was not an issue for the cluster rate analysis because SNe of interest (at $z \geq 0.9$) are not detectable very far after peak.

(2) Second, we exclude regions within $20''$ of cluster centers, in order to avoid the most strongly lensed areas in the volume behind the clusters. This region is only $\sim 3\%$ of the observed field of each cluster. Note that we were careful to choose this radius before looking at the radii of any of the candidates, in order to avoid biasing ourselves by adjusting the radius to conveniently exclude or include candidates. Two candidates were excluded as a result: SNe SCP06B3 ($16.8''$ from the cluster center) and SCP06M50 ($19.4''$ from the cluster center). As it happens, these candidates are unlikely to be SNe Ia. SN SCP06B3 is a "probable" SN CC, while SN SCP06M50 is possibly not a SN at all and may be hosted by a cluster member galaxy, making its position near the cluster center unsurprising. The exclusion of this region is taken into account in our simulations (§6.3). The effect of lensing on the remaining portions of the fields are discussed in §6.4.2.

The systematic uncertainties associated with the determination of SN type and redshift for the remaining candidates are addressed in §6.4.1.

6.3 Effective Visibility Time

As in the cluster rate analysis, we use a control time that depends on position, as observation dates and depths vary within each observed field. That is, in equation (6.1) we make the substitution

$$T(z)\Theta \Rightarrow \int_{x,y} T(x,y,z) dx dy. \tag{6.3}$$

$T(x, y, z)$ is calculated by simulating SN Ia light curves at different positions, redshifts and times during the survey, and determining the probability that each simulated SN would be detected and counted in our SN sample. We pass each simulated SN through the same automated selections used to select the 60 candidates in our initial sample. Additionally, we discard simulated SNe peaking prior to 10 rest-frame days before the first observation, as discussed in the previous section.

We characterize the diversity of SN Ia light curves as a two-parameter family (stretch s and color c) with an additional intrinsic dispersion in luminosity. The absolute magnitude of each simulated SN is set to

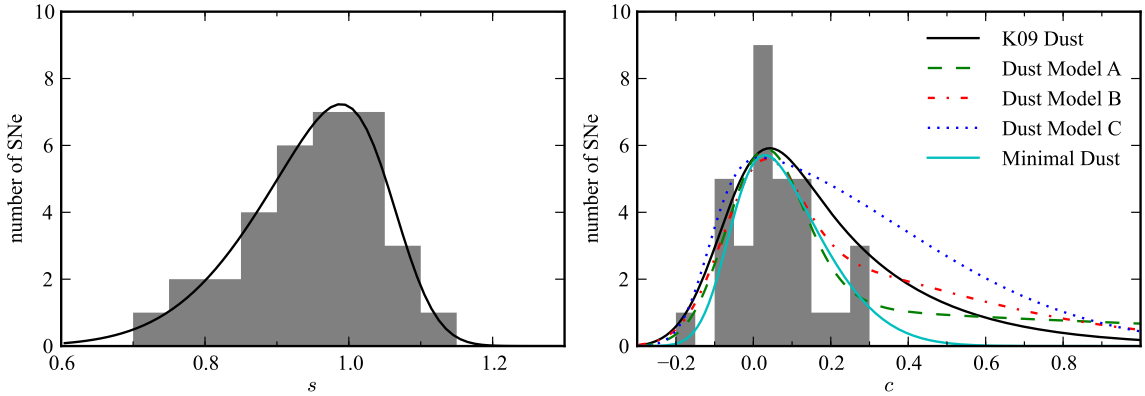$$M_B = -19.31 - \alpha(s - 1) + \beta c + I \tag{6.4}$$

Figure 6.1. *Left panel:* Stretch distribution used for simulated SNe (solid black line) and the stretch distribution of first-year SNLS $z < 0.6$ SNe (grey histogram) from Astier et al. (2006). *Right panel:* Color distribution used for simulated SNe (solid black line), based on the K09 distribution of host-galaxy extinction. The grey histogram shows the color distribution of the first-year SNLS $z < 0.6$ SNe. The other four lines show alternative color distributions used to assess the possible systematic error due to different distributions of host galaxy dust extinction (see §6.4.3).

where -19.31 is the magnitude of an $s = 1$, $c = 0$ SN Ia in our assumed cosmology (Astier et al. 2006), $\alpha = 1.24$, $\beta = 2.28$ (Kowalski et al. 2008), and I is an added "intrinsic dispersion", randomly drawn from a Gaussian distribution centered at zero with $\sigma = 0.15$ mag. To calculate the flux of each simulated SN in the observed z_{850} and i_{775} filters, we use the Hsiao et al. (2007) spectral time series template.

The main difference from the cluster rate analysis is that we use distributions for stretch and color that are representative of SNe in the field rather than specifically in clusters. The assumed stretch distribution (Fig. 6.1, left panel, solid line) is based on the observed stretch distribution from the first-year sample from the Supernova Legacy Survey (SNLS; Astier et al. 2006), cut at $z < 0.6$ to limit Malmquist bias (Fig. 6.1, left panel, histogram). In selecting a simulated color distribution we consider not only the observed SN color distribution, but also the expected distribution of host galaxy extinction. We assume that host galaxy extinction is distributed as $P(A_V) \propto \exp(-A_V/0.33)$, the best-fit value for host-galaxy SN extinction in the SDSS-II SN Survey (K09). A_V is related to c via $A_V = R_V \times E(B - V) \approx (\beta - 1) \times c$. We therefore assume a distribution of SN color $P(c) \propto \exp(-(\beta - 1)c/0.33)$ due to host galaxy extinction. The observed c distribution is a convolution of an intrinsic distribution of SN color (assumed to be Gaussian) and this color induced by host galaxy dust. The Gaussian parameters of the intrinsic distribution are chosen to match the observed SNLS c distribution (Fig. 6.1, right panel, histogram). The resulting convolved distribution is shown in Figure 6.1 (right panel, black line). In §6.4.3 we assess the systematic uncertainty associated with host galaxy dust by using alternate distributions of c (other curves in the panel).

$T(x, y, z)$ is calculated in bins of 100×100 pixels ($5'' \times 5''$ in position. We simulate
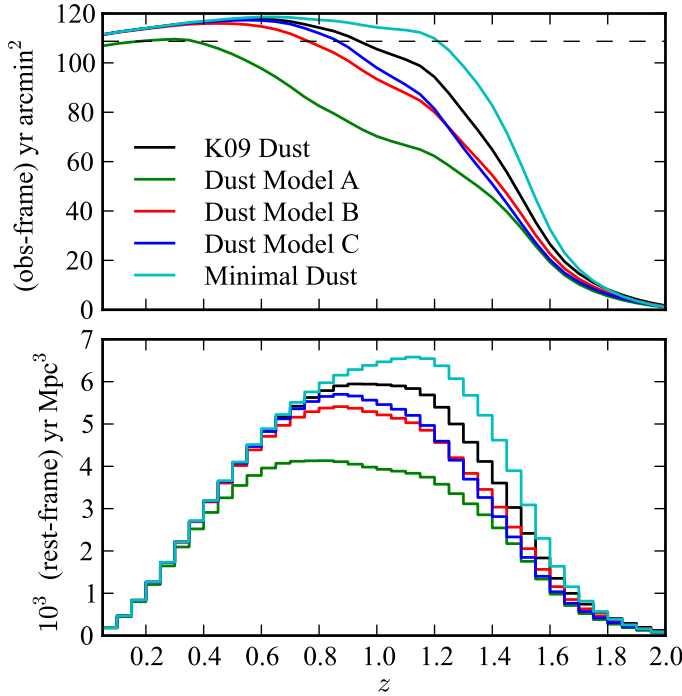
Figure 6.2. *Top panel:* The observer-frame effective visibility time multiplied by observed area, as a function of supernova redshift. The horizontal dotted line shows the area of the ACS field multiplied by the time spanned by the observations in each cluster. *Bottom panel:* The rest-frame volume-time searched in each redshift bin of $\Delta z = 0.05$. In each panel, the black line shows our main result for the effective visibility time, based on simulations using the K09 dust distribution. The green, red, blue and cyan lines show the results for alternative dust distributions.

50 SN light curves with random parameters and random position (within the bin) and take the average effective visibility time of the 50 SNe ($\sim$80,000 SNe per field). Summing over all areas observed in all 25 fields yields $T(z)$. In doing so we exclude regions within $20''$ of cluster centers, as discussed in the previous section. We calculate $T(z)$ at intervals of $\Delta z = 0.05$ in redshift.

6.4 Results

Figure 6.2 (top panel, black line) shows the observer-frame effective visibility time times area ($T(z)\Theta$ from Eq. 6.1) as a function of SN redshift. For reference, the horizontal dotted line shows an approximate calculation of this value, multiplying the area of the ACS field (11.65 arcmin^2) by the time difference between 10 days before the first observation and 10 days after the last observation. In reality the area actually observed is slightly more complicated and SNe are detected over a slightly larger time range. From $z = 0$, the effective visibility time actually increases slightly out to $z \sim 0.5$ as SN light curves are time-dilated and are thus visible for longer. Afterwards, we begin to miss SNe that peak during the observations. In the lower panel of Figure 6.2, we convert to the rest-frame time-volume observed in each redshift bin of $\Delta z = 0.05$ (Fig. 6.2, lower panel) using the assumed cosmology. The denominator of Equation (6.1) is obtained by summing over the redshift bin of interest. Table 6.1 shows the results, in bins of $\Delta z = 0.4$ and also in bins of $\Delta z = 0.5$. We now discuss the systematic uncertainties associated with lensing, SN type

Table 6.1. Results: field SN Ia rate

Redshift bin	$\bar{z}$	$N_{\rm SN\ Ia}$	Denom	Rate	(stat)	(sys)
$0.2 < z \le 0.6$	0.442	$0.00^{+0.00}_{-0.00}$	2.332	0.00	$^{+0.50}_{-0.00}$	$^{+0.00}_{-0.00}$
$0.6 < z \le 1.0$	0.807	$5.25^{+0.25}_{-1.25}$	4.464	1.18	$^{+0.60}_{-0.45}$	$^{+0.11}_{-0.28}$
$1.0 < z \le 1.4$	1.187	$5.63^{+0.63}_{-0.63}$	4.243	1.33	$^{+0.65}_{-0.49}$	$^{+0.30}_{-0.26}$
$1.4 < z \le 1.8$	1.535	$1.12^{+0.12}_{-1.12}$	1.453	0.77	$^{+1.07}_{-0.54}$	$^{+0.34}_{-0.77}$
$0.0 < z \le 0.5$	0.357	$0.00^{+0.00}_{-0.00}$	1.624	0.00	$^{+0.71}_{-0.00}$	$^{+0.00}_{-0.00}$
$0.5 < z \le 1.0$	0.766	$5.25^{+0.25}_{-1.25}$	5.321	0.99	$^{+0.51}_{-0.38}$	$^{+0.08}_{-0.24}$
$1.0 < z \le 1.5$	1.222	$6.75^{+0.75}_{-1.75}$	4.906	1.38	$^{+0.61}_{-0.47}$	$^{+0.33}_{-0.43}$
$1.5 < z \le 2.0$	1.639	$0.00^{+0.00}_{-0.00}$	0.890	0.00	$^{+1.30}_{-0.00}$	$^{+0.00}_{-0.00}$

Note. — "Denom" is the denominator of equation 6.1 (total rest frame time-volume searched in this bin) and has units 10^4 yr Mpc^3. The rate is given in units 10^{-4} yr^{-1} Mpc^{-3}. $N_{\rm SN\ Ia}$ is the observed number of SNe in the bin, with the uncertainty due to type determination. The non-integer number of SNe in each bin is attributable to the two candidates without spectroscopic redshifts. These candidates are assigned redshift ranges that are spread over multiple bins.

determination, host-galaxy dust, and variations in SN properties.

6.4.1 Type Determination

Only four of our SN candidates have spectroscopically confirmed types – for the remaining candidates there is some uncertainty in type. It is difficult to precisely quantify the uncertainty in our heterogeneous typing method, mainly because the information used to type each SN varies widely. In practice however, the uncertainty is quite small. Consider the candidates designated as SN Ia: all three SNe Ia at $z < 0.9$ are spectroscopically confirmed. At $z \gtrsim 0.9$, any SN bright enough to be detected is overwhelmingly likely to be Type Ia due to the faintness of core-collapse SNe relative to SNe Ia (see, e.g., Dahlen et al. 2004; Li et al. 2011, Meyers et al., submitted). Furthermore, while "probable" candidates are not as certain as "secure" candidates, this is still a fairly high-confidence type determination: A "probable" SN Ia means that a SN Ia light curve template has a χ^2 P-value that is 10^3 times larger than any SN CC value. A Bayesian analysis would therefore yield a type uncertainty close to zero for such candidates, regardless of the prior used.

The "plausible" candidates are perhaps the only candidates with significant type uncertainty. We quantify this uncertainty in a manner similar to Dahlen et al. (2008): The lower limit on the number of SNe Ia discovered is given by assuming that all "plausible" SNe Ia are in fact SNe CC, and the upper limit is given by assuming that all "plausible" SNe CC are in fact SNe Ia. These limits are shown as uncertainties in $N_{\rm SN\ Ia}$ in Table 6.1 and those uncertainties are included in the systematic error.

For the two candidates without spectroscopic host redshifts, we assign a redshift range

consistent with the SN light curve and/or host galaxy photometry, as follows: For SCP06E12, we use the range $0.8 < z < 1.2$. As there is uncertainty about both the type and cluster membership, we count SCP06E12 as 0.5 ± 0.5 field SNe Ia. The situation is similar for SCP06N32: the light curve is consistent with an SN Ibc at $z \sim 0.9$, but also with an SN Ia at $z \sim 1.3$. We therefore assign a redshift range of $1.1 < z < 1.5$ and count it as 0.5 ± 0.5 field SNe Ia. Finally, note that the spectroscopic host galaxy redshift of $z = 1.44$ for SCP06X26 is tentative because it is based on a single (low signal-to-noise) emission line. This redshift uncertainty contributed to the low-confidence "plausible" in the type and the typing systematic error encompasses the possibility that SCP06X26 is not an SN Ia at this redshift. This makes the rate for the highest redshift bin $1.4 < z < 1.8$ an upper limit only. However, note that the light curve of SCP06X26 is completely consistent with a typical $z = 1.44$ SN Ia.

6.4.2 Lensing Due to Clusters

The presence of a massive galaxy cluster in each of the 25 observed fields presents a complication for measuring the volumetric field rate. A cluster will preferentially magnify sources behind it (increasing the discovery efficiency of SNe), and will also shrink the source plane area Θ behind the cluster (decreasing the number of SNe discovered) (e.g., Goobar et al. 2009). Fortunately the effect on the calculated rates in this survey is small, for two reasons. First, the high redshifts of the clusters means that the volume of interest in the cluster backgrounds is close to the clusters and therefore not lensed very efficiently. Second, the two effects (magnification and source plane area shrinkage) are opposing in terms of number of SNe discovered. Furthermore, we have already excluded from the analysis the central $20''$ of each field, where lensing effects are the largest.

We have calculated the magnitude of each lensing effect on the remaining outer regions using a simple lensing model: We assume each cluster has a mass of $M_{200} = 4 \times 10^{14}\ M_\odot$ (the approximate average mass in our sample, as reported by Jee et al., in preparation) and an NFW mass profile. We distribute clusters according to their redshifts and calculate the lensing effect on the 25 annular regions $20'' < r < 100''$ around the clusters. The distribution of magnification in these regions as a function of source redshift is shown in Figure 6.3. The magnification is quite small: even at a source redshift of $z = 1.8$, most of the area is magnified by less than 10%. As a rough estimate of the effect on the derived rates, we show the average magnification for each source redshift, and the effect such a magnification would have on the effective visibility time at this redshift. The effect is only a few percent at $z \lesssim 1.4$ but starts to increase steeply towards $z = 1.8$. In Figure 6.4 we show the decrease in the source area as a function of redshift, which translates directly into a decrease in the effective visibility time $\times$ area. The decrease is close to linear with redshift past $z = 1.2$, reaching $\sim 13\%$ at $z = 1.8$.

We conclude from these simulations that the two effects cancel to within a few percent of the total rate, over the redshift range of interest: At $z = 1.4$, magnification increases SN detectability by $\sim 3\%$ and source-area reduction decreases detectability by $\sim 6\%$. At
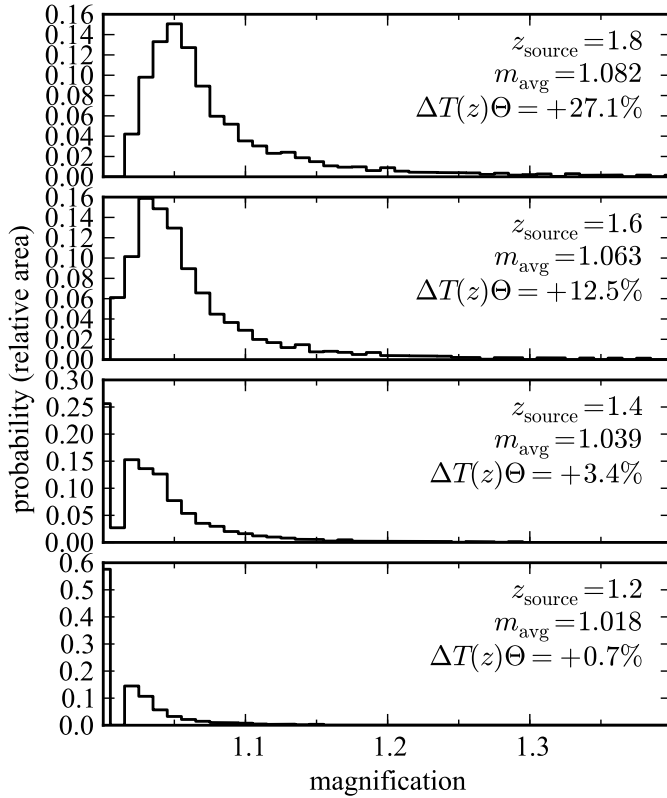
Figure 6.3. Lensing magnification distribution in our lensing simulation, as a function of source redshift. The distribution is taken from the regions at radius $20'' < r < 100''$ in each of 25 cluster fields (the approximate extent of the regions used in the rate analysis). For each source redshift, the average magnification m_{avg} is given. If all simulated SNe at this redshift were magnified by m_{avg}, the effective visibility time would increase by $\Delta T(z)\Theta$. At $z < 1.4$ lensing magnification has only a $\lesssim 3\%$ effect on the detectability of SNe.

$z = 1.6$, the increase is $\sim 12\%$, and the decrease is $\sim 10\%$. At $z = 1.8$ the increase overwhelms the decrease ($\sim 27\%$ versus $\sim 13\%$), but there will be very few SNe detected beyond $z \sim 1.6$ (see Fig. 6.2). Therefore, we have not made an adjustment for these effects. Furthermore, the size of each effect is much smaller than other sources of systematic error considered below. For example, the average magnification at $z = 1.8$ is only ~ 1.08 (-0.08 mag), whereas below we consider the effect of changing the luminosity of all SNe in our simulation by ± 0.2 magnitudes. As a result, we do not assign a specific systematic error to the lensing effects.

6.4.3 Dust Extinction

The degree to which SNe are affected by host galaxy dust extinction is perhaps the largest systematic uncertainty in SN Ia rate studies. To evaluate the effect on the derived rates, we consider four alternative extinction distributions. Three of these are comparable to distributions examined in Dahlen et al. (2008). The first, labeled "Model A," is used in their main result and is based on Hatano et al. (1998). We approximate this distribution as

$$P(A_V) = \frac{0.61}{2}e^{-A_V/2} + \frac{0.39}{0.07}e^{-A_V/0.07}. \tag{6.5}$$
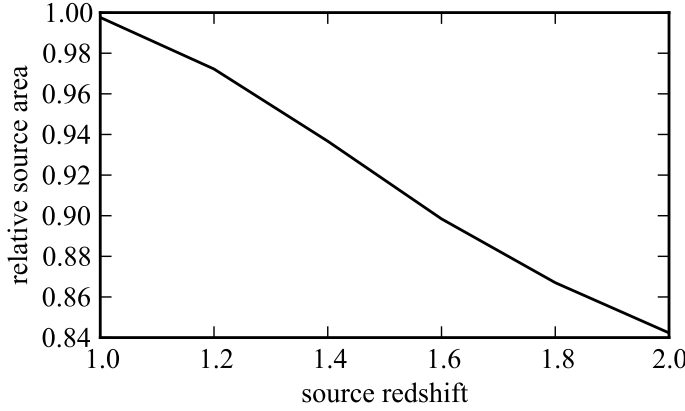
Figure 6.4. True source-plane area relative to the observed area in our lensing simulation, as a function of source redshift. The relative area is for regions at radius $20'' < r < 100''$ in each of the 25 cluster fields (the approximate extent of the regions used in the analysis).
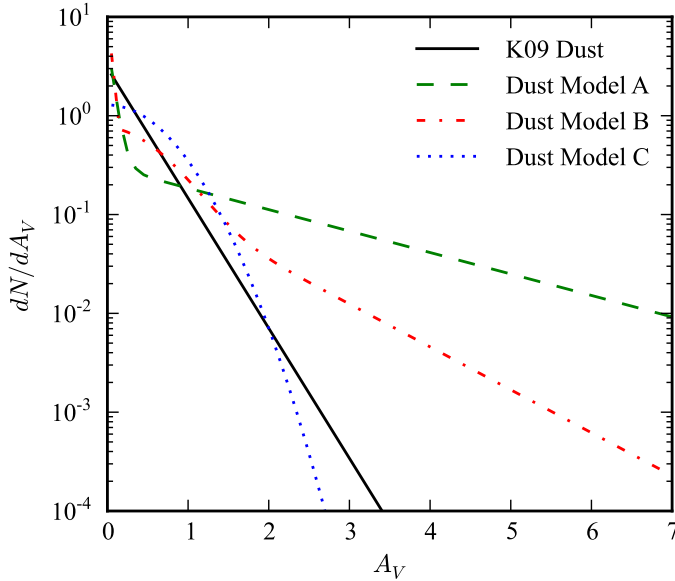

Figure 6.5. Host galaxy dust extinction distributions. The K09 distribution is used for our main result. Models A, B, and C are similar to the models of the same name examined in Dahlen et al. (2008) and are based on results from Hatano et al. (1998), Riello & Patat (2005) and Neill et al. (2006), respectively. These alternative distributions are used here to investigate possible systematic error due to host galaxy dust.

The second, labeled "Model B," is based on Riello & Patat (2005) and is approximated here by

$$P(A_V) = 0.35\delta(A_V) + \frac{0.40 \times 2}{0.6\sqrt{2\pi}}e^{-A_V^2/(2\times 0.6^2)} + 0.25e^{-A_V}. \tag{6.6}$$

The third, labeled "Model C," is based on Neill et al. (2006) and is given by

$$P(A_V) = \frac{2}{0.62\sqrt{2\pi}}e^{-A_V^2/(2\times 0.62^2)}. \tag{6.7}$$

These distributions are reproduced in Figure 6.5, and the corresponding distributions of SN color are shown in Figure 6.1 (right panel). In addition to these three distributions, we also consider a distribution with minimal dust, where we assume the SNLS $z < 0.6$ sample is complete and fit it with a skewed Gaussian distribution. The effective visibility time for
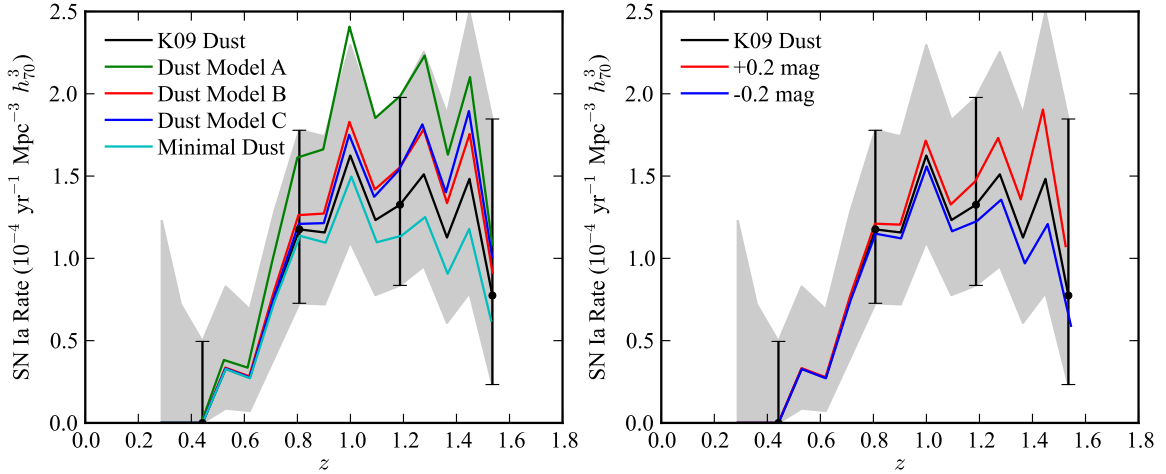
Figure 6.6. The volumetric SN Ia rate in four redshift bins (points with error bars) of width $\Delta z = 0.4$. The error bars represent the statistical-only error. The black line shows the rate calculated in a moving bin of width $\Delta z = 0.4$ (grey regions represent uncertainty). Note that the points with error bars are uncorrelated errors (using non-overlapping bins), while the uncertainty in the moving bin is correlated from point to point. *Left Panel*: The green, red, blue and cyan lines show the rate (with no uncertainty) assuming alternative SN color distributions. *Right Panel*: The red and blue lines show the rate assuming that all SNe are brighter or dimmer by ± 0.2 mag.

each dust model is shown in Figure 6.2 and the corresponding SN rate results are shown in Figure 6.6 (left panel).

Of all the models, Model A produces the most strikingly different results for the effective visibility time. Even in the lowest redshift bin ($0.2 < z < 0.6$) it implies that 10% of SNe are missed due to dust, relative to the K09 model. In the $0.6 < z < 1.0$ redshift bin, it yields effective visibility times lower by 27%, while Models B, C and the minimal dust model result in changes of only -7%, -3%, and $+3\%$ respectively. This is unsurprising: In dust model A, 26% of SNe have host galaxy extinctions $A_V > 2$ while this fraction is $< 4\%$ in model B and $< 1\%$ in models K09 and C. In the $1.0 < z < 1.4$ bin model A has the largest effect: -33% compared to the K09 model.

For the systematic error associated with the choice of dust model we take the minimal dust model as the extreme lower limit and model B/C as the upper limit, regarding model A as an outlying model. This systematic error is propagated and included in Table 6.1.

6.4.4 Other SN Properties

Other assumptions about SN properties (besides dust extinction) can affect the results. To first order, changing the assumed distributions of s or changing the assumed spectral time series will affect the detection efficiency by increasing or decreasing the luminosity of the simulated SN. To jointly capture these effects, we shift the absolute magnitude of

the simulated SNe Ia by $^{+0.2}_{-0.2}$ mag and recalculate the control times. To first order, this is equivalent to shifting the s distribution by $\Delta s = 0.2/\alpha \sim 0.16$ (or shifting the c distribution by $\Delta c = 0.2/\beta \sim 0.09$). The effect on the results is shown in Figure 6.6 (right panel) and this range of uncertainty is included in the systematic error in Table 6.1.

6.5 Discussion

6.5.1 Comparison to Other High-Redshift Measurements

In Figure 6.7 we compare our results to an assortment of other volumetric SN Ia rate measurements. (Most published measurements use the same cosmology used here; those that do not have been corrected to our assumed cosmology.) At $z \gtrsim 1$ the three existing measurements are Kuznetsova et al. (2008, hereafter Ku08), Dahlen et al. (2008, hereafter D08), and Graur et al. (2011, hereafter G11). D08 and G11 supplant earlier results from Dahlen et al. (2004) and Poznanski et al. (2007b), respectively. The Ku08 and D08 measurements are based on SN searches in the *HST* GOODS fields, with Ku08 being an independent analysis of a subset of the data used in D08. These SN searches used ACS to cover the GOODS fields with a 45 day cadence and triggered followup (imaging and spectroscopy) of SN candidates. The D08 analysis uses a SN typing method based on both spectroscopy and photometry (similar to the approach used here) while Ku08 use a photometric-only pseudo-Bayesian approach to typing. The G11 measurement is based on "single-detection" searches in the Subaru Deep Field. G11 also use a pseudo-Bayesian typing approach, but use a single detection with observations in three filters, rather than multiple detections with observation in (typically) two filters as in Ku08.

Our results in the three highest redshift bins are very similar to D08 and are consistent with G11 and Ku08 at the $\sim 1\sigma$ level. Even with limited statistics of only ~ 12 SNe Ia, they provide additional strong evidence that the SN rate is $\gtrsim 0.6 \times 10^{-4} \ h_{70}^3 \ \mathrm{yr}^{-1} \ \mathrm{Mpc}^{-3}$ at $z \sim 1$. With the data available from Figure 6.2 and the SN candidate list, the rates from this survey can be recomputed in any arbitrary bin and for a variety of assumptions about SN properties and host galaxy dust distributions. This will make it easy to combine these results with other measurements for increased statistical power.

6.5.2 Comparison of Host-Galaxy Dust Distributions

In light of the large systematic differences noted in §6.4.3 due to choice of host galaxy dust distribution, it is interesting to compare the distributions used in D08, Ku08 and G11.

For their main result, D08 use a distribution similar to model A used here, and also consider models similar to B and C. (Our models A, B and C are based on models with the same labels in D08.) If we had assumed model A, our derived rates in the two mid-
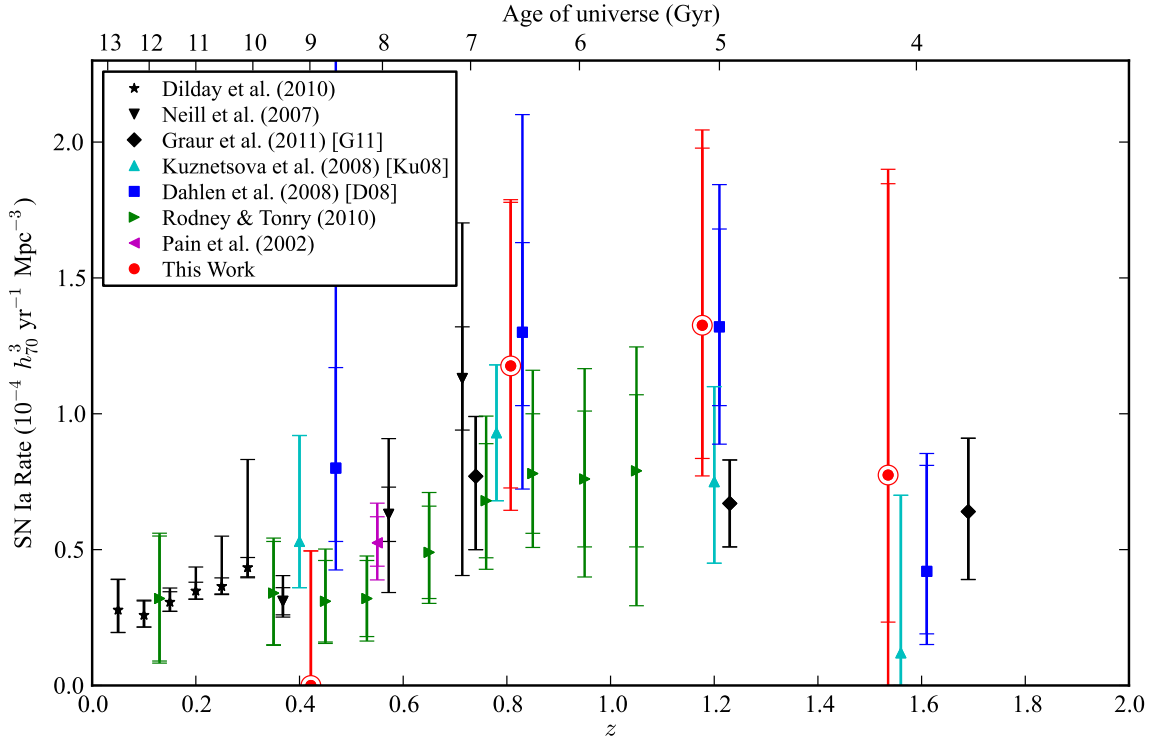
Figure 6.7. Volumetric SN Ia rates from the *HST* Cluster Supernova Survey (red points) compared to key rates from the literature. For measurements with two error bars, including ours, the inner and outer error bars represent the statistical (Poisson) and total (statistical + systematic) uncertainties, respectively. Measurements with a single error bar (Ku08 and G11) are Bayesian-based analyses where the error bar encompasses both statistical and typing uncertainties.

redshift bins would have been $\sim 30\%$ higher, implying rates larger than those found in D08. Interestingly, D08 do not find the large difference between model A and models B/C that we find here. They find that model B produces rates that are $\lesssim 10\%$ lower than model A (only $\sim 4\%$ in the highest redshift bin). Model C is found to have even less of an effect (and actually *increases* rates relative to model A in the highest bin). It is difficult to know whether this difference could be due to the different cadence (~ 23 days here versus ~ 45 days in GOODS), difference in details of the efficiency simulations, or some other cause.

Both Ku08 and G11 use distributions lacking the high-extinction tail of model A and are thus more similar to models B/C or K09. Ku08 use only two discrete values, $A_V = 0.0$ and 0.4 (but also consider the case $A_V = 1.0$ in assessing systematic uncertainty). G11 use the distribution of N06 (model C), but truncated at $A_V = 1$ (eliminating the highest-extinction $\sim 10\%$ of the distribution). In contrast, 40% of SNe have $A_V > 1$ in model A. This difference in assumptions might explain some differences in the results. In particular, it would explain why the D08 result is much higher than K08 despite the large overlap in

datasets. It would also partially explain why the D08 result is significantly higher than the G11 result in the $0.6 < z < 1.4$ redshift range.

CHAPTER 7

Conclusions

The central work in this thesis has been a calculation of SN Ia rates from the *HST* Cluster Supernova Survey. This required the systematic selection of SN candidates and determination of their types. As part of this selection and typing we have presented data on the unusual transient SCP06F6, most likely to be a new rare type of SN. Here, we highlight the unique aspects of the measurements themselves and draw conclusions about the cluster and field rate results.

7.1 Measurements

We have benefited from an unusually complete dataset (particularly for a cluster rate study). As a result, the measurements are quite robust. For the cluster rate measurement in particular, statistical and systematic uncertainties are on par with or better than measurement uncertainties at low redshift. We highlight several important and/or unique aspects of the measurements:

- The SN classification approach takes advantage of all relevant information. Thanks to the "rolling search" strategy of the survey and the nearly complete spectroscopic follow-up, most candidates have a full light curve and a host galaxy redshift, greatly reducing classification uncertainty.

- The position-dependent control time allows one to calculate a supernova rate given an arbitrary observing pattern and luminosity distribution.

- The control time calculation includes a full distribution of SN properties and the systematic uncertainty associated with the assumed distribution is carefully quantified. For the cluster rate, thanks to the depth of the observations, the detection efficiency approaches 100% during the period of the survey for most of the clusters, meaning that the systematic uncertainty is low.

- For the cluster rate, statistical uncertainties associated with the cluster luminosities, including both statistical variations and cosmic variance, are included in the total

uncertainty. Also, light in the outskirts of each galaxy (outside the SEXTRACTOR MAG_AUTO aperture) is accounted for. This is a significant component of the total cluster luminosity.

- Cluster SN Ia rate measurements are normalized consistently across redshifts using a redshift-dependent mass-to-light versus color relation.

7.2   Cluster Rate

For the first time, our result shows (at the $> 2\sigma$ level) that the cluster SN Ia rate is increasing with redshift. Simply by comparing the low- and high-redshift cluster rate measurements, the shape of the late-time SN Ia delay time distribution can be constrained. The power of the measurement for this purpose comes both from the high redshift and relatively low statistical and systematic uncertainties in the measurement. While we cannot conclusively rule out either the single degenerate or double degenerate class of progenitors via the delay time distribution, the binary evolution that could lead to each model are constrained. The DD scenario is consistent with the measurement under a wide range of plausible binary evolution parameters, while there is a stronger constraint on binary scenarios that could lead to an SD scenario. Finally, this measurement is unique in constraining the delay time distribution at delay times of a few Gyr. In future studies, it can be used in combination with other cluster rates and other delay time distribution measurements (e.g., Maoz et al. 2010) to place even tighter constraints on models for binary evolution and SN Ia progenitor scenarios.

7.3   Field Rate

We computed volumetric SN Ia rates based on $\sim$12 SNe Ia discovered in 189 *HST* orbits. This large *HST* dataset adds significant statistics to the existing *HST* rate measurements, previously based only on the GOODS fields. The availability of raw data from our efficiency simulations makes it simple to combine this dataset with current and future *HST* datasets, such as the in-progress CANDELS survey.

We find that the dominant systematic uncertainty in our result is the amount of host-galaxy dust assumed in our simulations. In fact, differences in these assumptions can explain a large amount of the discrepancy between different *HST* GOODS rate measurements and differences between *HST* and ground-based measurements. This illustrates the need to use caution in calculating and interpreting SN rate results, especially as statistical error decreases and systematic uncertainties become dominant.

7.4   Status and Future Work

The measurements presented in this thesis are just part of a greater transition toward an accurate measurement of the SN Ia delay time distribution. When the *HST* Cluster Supernova Survey was beginning five years ago, little was known about the shape of the DTD from observations. Since then, the situation has changed dramatically. Results using a wide variety of methods, including volumetric rates and cluster rates, have coalesced into a consistent picture of a DTD declining from a few hundred Myr to ∼10 Gyr, with a slope consistent with $\sim t^{-1}$. The cluster rate measurements presented here have been instrumental in mapping out the DTD in the longer delay time regions.

Still, we have only yet made the coarsest measurement of the SN Ia DTD: The data are good enough to fit a power-law slope and an amplitude, but not much more. There is much we can still learn from a more accurate measurement. Does the DTD truly follow a single power law over the full range of delay times? If so, is the slope really exactly t^{-1}? There is no reason to think the answer to either question is yes. By finding a more detailed behavior and/or a more precise power law slope, we can learn much more about not only the SN Ia progenitor scenario, but also details of binary evolution.

Going forward, there are still many gains to be made simply from increased statistics. Specifically for cluster rate measurements, Poisson statistics dominate the uncertainty in the measurement presented in this thesis (and as a result, the DTD constraints as well). Forthcoming results from the Multi-Epoch Nearby Cluster Survey (Sand et al. 2008, 2011) will increase statistics at $z \lesssim 0.15$ with 22 new cluster SN Ia discoveries. At $z \sim 0.5$, the *HST* CLASH survey[1] will provide on the order of $10 - 15$ new cluster SNe Ia. At the highest redshifts, another program similar to the *HST* Cluster Supernova Survey, or perhaps a ground-based dedicated cluster rate survey on a 10m class telescope, could enhance statistics in this crucial redshift regime.

In other DTD measurements, systematics are already playing a dominant role. For field rate measurements, Graur et al. (2011) notes that uncertainties in the cosmic SFH are already the dominant uncertainty in determining the DTD. In this thesis we have seen that uncertainty in the host galaxy dust distribution is also significant compared to the statistical uncertainty in rate measurements. In the future, deeper surveys can help limit this uncertainty by directly constraining the numbers of extincted SNe Ia. The in-progress *HST* CANDELS survey[2] will do this to some extent, discovering SNe Ia well past $z = 2$, but much more significant gains will be possible with a dedicated wide-field infrared survey telescope.

---

[1]http://www.stsci.edu/~postman/CLASH
[2]http://candels.ucolick.org

Bibliography

Abe, F., et al. 2004, Science, 305, 1264

Amanullah, R., et al. 2010, ApJ, 716, 712

Anderson, J. & King, I. R. 2006, PSFs, Photometry, and Astronomy for the ACS/WFC, Tech. rep.

Andreon, S. 2006a, in The Fabulous Destiny of Galaxies: Bridging Past and Present, ed. V. Le Brun, A. Mazure, S. Arnouts, & D. Burgarella, 463

Andreon, S. 2006b, MNRAS, 369, 969

—. 2006c, A&A, 448, 447

—. 2008, MNRAS, 386, 1045

Andreon, S., de Propris, R., Puddu, E., Giordano, L., & Quintana, H. 2008a, MNRAS, 383, 102

Andreon, S., Puddu, E., de Propris, R., & Cuillandre, J. 2008b, MNRAS, 385, 979

Andreon, S., Valtchanov, I., Jones, L. R., Altieri, B., Bremer, M., Willis, J., Pierre, M., & Quintana, H. 2005, MNRAS, 359, 1250

Appenzeller, I., et al. 1998, The Messenger, 94, 1

Astier, P., et al. 2006, A&A, 447, 31

Aubourg, É., Tojeiro, R., Jimenez, R., Heavens, A., Strauss, M. A., & Spergel, D. N. 2008, A&A, 492, 631

Bailey, S., et al. 2009, A&A, 500, L17

Barbary, K., et al. 2011, preprint (arXiv:1010.5786)

Barbary, K., et al. 2009, ApJ, 690, 1358

Belczynski, K., Bulik, T., & Ruiter, A. J. 2005, ApJ, 629, 915

Bell, E. F. & de Jong, R. S. 2001, ApJ, 550, 212

Bell, E. F., McIntosh, D. H., Katz, N., & Weinberg, M. D. 2003, ApJS, 149, 289

Bertin, E. & Arnouts, S. 1996, A&AS, 117, 393

Blondin, S. & Tonry, J. L. 2007, ApJ, 666, 1024

Bohringer, H., Mullis, C., Rosati, P., Lamer, G., Fassbender, R., Schwope, A., & Schuecker, P. 2005, The Messenger, 120, 33

Boyle, B. J. 1989, MNRAS, 240, 533

Brandt, T. D., Tojeiro, R., Aubourg, É., Heavens, A., Jimenez, R., & Strauss, M. A. 2010, AJ, 140, 804

Bremer, M. N., et al. 2006, MNRAS, 371, 1427

Brodwin, M., et al. 2006, ApJ, 651, 791

Brodwin, M., et al. 2011, ApJ, 732, 33

Bruzual, G. & Charlot, S. 2003, MNRAS, 344, 1000

Butcher, H. & Oemler, Jr., A. 1978, ApJ, 219, 18

—. 1984, ApJ, 285, 426

Cain, B., et al. 2008, ApJ, 679, 293

Calura, F., Matteucci, F., & Tozzi, P. 2007, MNRAS, 378, L11

Cappellaro, E., Evans, R., & Turatto, M. 1999, A&A, 351, 459

Cardelli, J. A., Clayton, G. C., & Mathis, J. S. 1989, ApJ, 345, 245

Chandrasekhar, S. 1931, ApJ, 74, 81

Chatzopoulos, E., Wheeler, J. C., & Vinko, J. 2009, ApJ, 704, 1251

Condon, J. J., Cotton, W. D., Greisen, E. W., Yin, Q. F., Perley, R. A., Taylor, G. B., & Broderick, J. J. 1998, AJ, 115, 1693

Conley, A., et al. 2008, ApJ, 681, 482

Crawford, S. M., Bershady, M. A., & Hoessel, J. G. 2009, ApJ, 690, 1158

Dahlen, T., Strolger, L.-G., & Riess, A. G. 2008, ApJ, 681, 462

Dahlen, T., et al. 2004, ApJ, 613, 189

Dallaporta, N. 1973, A&A, 29, 393

Dawson, K., et al. 2006, Central Bureau Electronic Telegrams, 546, 1

Dawson, K. S., et al. 2009, AJ, 138, 1271

Dilday, B., et al. 2010a, ApJ, 715, 1021

Dilday, B., et al. 2010b, ApJ, 713, 1026

Dong, S., et al. 2006, ApJ, 642, 842

Eisenhardt, P. R. M., et al. 2008, ApJ, 684, 905

Elias, J. H., Matthews, K., Neugebauer, G., & Persson, S. E. 1985, ApJ, 296, 379

Elston, R. J., et al. 2006, ApJ, 639, 816

Feldmeier, J. J., Ciardullo, R., & Jacoby, G. H. 1998, ApJ, 503, 109

Feldmeier, J. J., Ciardullo, R., Jacoby, G. H., & Durrell, P. R. 2004, ApJ, 615, 196

Ferguson, H. C., Tanvir, N. R., & von Hippel, T. 1998, Nature, 391, 461

Filippenko, A. V. 1997, ARA&A, 35, 309

Fioc, M. & Rocca-Volmerange, B. 1997, A&A, 326, 950

Fruchter, A. S. & Hook, R. N. 2002, PASP, 114, 144

Gal-Yam, A., Maoz, D., Guhathakurta, P., & Filippenko, A. V. 2003, AJ, 125, 1087

Gal-Yam, A., Maoz, D., & Sharon, K. 2002, MNRAS, 332, 37

Gänsicke, B. T., Levan, A. J., Marsh, T. R., & Wheatley, P. J. 2009, ApJ, 697, L129

Geier, S., Nesslinger, S., Heber, U., Przybilla, N., Napiwotzki, R., & Kudritzki, R.-P. 2007, A&A, 464, 299

Giavalisco, M., et al. 2004, ApJ, 600, L93

Gilbank, D. G., Yee, H. K. C., Ellingson, E., Hicks, A. K., Gladders, M. D., Barrientos, L. F., & Keeney, B. 2008, ApJ, 677, L89

Gilfanov, M. & Bogdán, Á. 2010, Nature, 463, 924

Gladders, M. D. & Yee, H. K. C. 2005, ApJS, 157, 1

Gobat, R., Rosati, P., Strazzullo, V., Rettura, A., Demarco, R., & Nonino, M. 2008, A&A, 488, 853

Gonzalez, A. H., Zabludoff, A. I., & Zaritsky, D. 2005, ApJ, 618, 195

Gonzalez, A. H., Zabludoff, A. I., Zaritsky, D., & Dalcanton, J. J. 2000, ApJ, 536, 561

González Hernández, J. I., Ruiz-Lapuente, P., Filippenko, A. V., Foley, R. J., Gal-Yam, A., & Simon, J. D. 2009, ApJ, 691, 1

Goobar, A., et al. 2009, A&A, 507, 71

Goto, T., et al. 2002, PASJ, 54, 515

Goto, T., et al. 2005, ApJ, 621, 188

Graham, A. W. & Driver, S. P. 2005, Publications of the Astronomical Society of Australia, 22, 118

Graur, O., et al. 2011, preprint (arXiv:1102.0005)

Greggio, L. 2005, A&A, 441, 1055

Greggio, L. & Renzini, A. 1983, A&A, 118, 217

Greggio, L., Renzini, A., & Daddi, E. 2008, MNRAS, 388, 829

Guy, J., et al. 2007, A&A, 466, 11

Guy, J., Astier, P., Nobili, S., Regnault, N., & Pain, R. 2005, A&A, 443, 781

Hachisu, I., Kato, M., & Nomoto, K. 2008, ApJ, 683, L127

Hakobyan, A. A., Petrosian, A. R., McLean, B., Kunth, D., Allen, R. J., Turatto, M., & Barbon, R. 2008, A&A, 488, 523

Hall, P. B. & Maxwell, A. J. 2008, ApJ, 678, 1292

Hamuy, M., Phillips, M. M., Suntzeff, N. B., Schommer, R. A., Maza, J., & Aviles, R. 1996, AJ, 112, 2398

Hamuy, M., Trager, S. C., Pinto, P. A., Phillips, M. M., Schommer, R. A., Ivanov, V., & Suntzeff, N. B. 2000, AJ, 120, 1479

Hatano, K., Branch, D., & Deaton, J. 1998, ApJ, 502, 177

Hicken, M., Wood-Vasey, W. M., Blondin, S., Challis, P., Jha, S., Kelly, P. L., Rest, A., & Kirshner, R. P. 2009, ApJ, 700, 1097

Hicks, A. K., et al. 2008, ApJ, 680, 1022

Hilton, M., et al. 2007, ApJ, 670, 1000

Hilton, M., et al. 2009, ApJ, 697, 436

Horiuchi, S. & Beacom, J. F. 2010, ApJ, 723, 329

Howell, D. A., et al. 2006, Nature, 443, 308

Howell, D. A., et al. 2005, ApJ, 634, 1190

Hsiao, E. Y., Conley, A., Howell, D. A., Sullivan, M., Pritchet, C. J., Carlberg, R. G., Nugent, P. E., & Phillips, M. M. 2007, ApJ, 663, 1187

Huang, X., et al. 2009, ApJ, 707, L12

Iben, Jr., I. & Tutukov, A. V. 1984, ApJS, 54, 335

Ihara, Y., Ozaki, J., Doi, M., Shigeyama, T., Kashikawa, N., Komiyama, K., & Hattori, T. 2007, PASJ, 59, 811

Jee, M. J., et al. 2009, ApJ, 704, 672

Jha, S., Riess, A. G., & Kirshner, R. P. 2007, ApJ, 659, 122

Kashikawa, N., et al. 2002, PASJ, 54, 819

Kenter, A., et al. 2005, ApJS, 161, 9

Kessler, R., et al. 2009, ApJS, 185, 32

Kobayashi, C. & Nomoto, K. 2009, ApJ, 707, 1466

Koekemoer, A. M., Fruchter, A. S., Hook, R. N., & Hack, W. 2002, in The 2002 HST Calibration Workshop : Hubble after the Installation of the ACS and the NICMOS Cooling System, ed. S. Arribas, A. Koekemoer, & B. Whitmore, 337

Kowalski, M., et al. 2008, ApJ, 686, 749

Krick, J. E., Bernstein, R. A., & Pimbblet, K. A. 2006, AJ, 131, 168

Kuznetsova, N., et al. 2008, ApJ, 673, 981

Kuznetsova, N. V. & Connolly, B. M. 2007, ApJ, 659, 530

Li, W., et al. 2011, MNRAS, 412, 1441

Lin, Y.-T. & Mohr, J. J. 2004, ApJ, 617, 879

Livio, M. 2001, in Supernovae and Gamma-Ray Bursts: the Greatest Explosions since the Big Bang, ed. M. Livio, N. Panagia, & K. Sahu, 334–355

Livio, M. & Riess, A. G. 2003, ApJ, 594, L93

Loewenstein, M. 2006, ApJ, 648, 230

Mannucci, F., Della Valle, M., & Panagia, N. 2006, MNRAS, 370, 773

Mannucci, F., Della Valle, M., Panagia, N., Cappellaro, E., Cresci, G., Maiolino, R., Petrosian, A., & Turatto, M. 2005, A&A, 433, 807

Mannucci, F., Maoz, D., Sharon, K., Botticella, M. T., Della Valle, M., Gal-Yam, A., & Panagia, N. 2008, MNRAS, 383, 1121

Maoz, D. & Gal-Yam, A. 2004, MNRAS, 347, 951

Maoz, D. & Mannucci, F. 2008, MNRAS, 388, 421

Maoz, D., Sharon, K., & Gal-Yam, A. 2010, ApJ, 722, 1879

Matteucci, F. & Greggio, L. 1986, A&A, 154, 279

Matteucci, F. & Recchi, S. 2001, ApJ, 558, 351

Melbourne, J., et al. 2007, AJ, 133, 2709

Mennekens, N., Vanbeveren, D., De Greve, J. P., & De Donder, E. 2010, A&A, 515, A89

Meyers, J., et al. 2011, ApJ, submitted

Mihos, J. C., Harding, P., Feldmeier, J., & Morrison, H. 2005, ApJ, 631, L41

Minkowski, R. 1941, PASP, 53, 224

Morokuma, T., et al. 2008, ApJ, 676, 163

Morokuma, T., et al. 2010, PASJ, 62, 19

Mullis, C. R., Rosati, P., Lamer, G., Böhringer, H., Schwope, A., Schuecker, P., & Fassbender, R. 2005, ApJ, 623, L85

Neill, J. D., et al. 2007, in American Institute of Physics Conference Series, Vol. 924, The Multicolored Landscape of Compact Objects and Their Explosive Origins, ed. T. di Salvo, G. L. Israel, L. Piersant, L. Burderi, G. Matt, A. Tornambe, & M. T. Menna, 421–424

Neill, J. D., et al. 2006, AJ, 132, 1126

Nelemans, G., Voss, R., Roelofs, G., & Bassa, C. 2008, MNRAS, 388, 487

Nomoto, K. 1982, ApJ, 253, 798

Nugent, P., Kim, A., & Perlmutter, S. 2002, PASP, 114, 803

Oke, J. B., et al. 1995, PASP, 107, 375

Paczynski, B. 1986, ApJ, 304, 1

Pain, R., et al. 2002, ApJ, 577, 120

Panagia, N. 1985, in Lecture Notes in Physics, Berlin Springer Verlag, Vol. 224, Supernovae as Distance Indicators, ed. N. Bartel, 14–33

Parthasarathy, M., Branch, D., Jeffery, D. J., & Baron, E. 2007, New Astronomy Review, 51, 524

Pastorello, A., et al. 2010, ApJ, 724, L16

Peng, C. Y., Ho, L. C., Impey, C. D., & Rix, H. 2002, AJ, 124, 266

Perlman, E. S., Horner, D. J., Jones, L. R., Scharf, C. A., Ebeling, H., Wegner, G., & Malkan, M. 2002, ApJS, 140, 265

Perlmutter, S., et al. 1999, ApJ, 517, 565

Perlmutter, S., et al. 1997, ApJ, 483, 565

Perlmutter, S., et al. 1995, ApJ, 440, L41

Phillips, M. M. 1993, ApJ, 413, L105

Postman, M., Lubin, L. M., Gunn, J. E., Oke, J. B., Hoessel, J. G., Schneider, D. P., & Christensen, J. A. 1996, AJ, 111, 615

Postman, M., Lubin, L. M., & Oke, J. B. 2001, AJ, 122, 1125

Poznanski, D., Maoz, D., & Gal-Yam, A. 2007a, AJ, 134, 1285

Poznanski, D., et al. 2007b, MNRAS, 382, 1169

Quimby, R. M., et al. 2009, preprint (arXiv:0910.0059)

Richardson, D., Branch, D., Casebeer, D., Millard, J., Thomas, R. C., & Baron, E. 2002, AJ, 123, 745

Riello, M. & Patat, F. 2005, MNRAS, 362, 671

Riess, A. G., et al. 1998, AJ, 116, 1009

Ripoche, P., et al. 2011, ApJ, submitted

Rix, H., et al. 2004, ApJS, 152, 163

Rodney, S. A. & Tonry, J. L. 2010, ApJ, 723, 47

Roelofs, G., Bassa, C., Voss, R., & Nelemans, G. 2008, MNRAS, 391, 290

Rosati, P., Stanford, S. A., Eisenhardt, P. R., Elston, R., Spinrad, H., Stern, D., & Dey, A. 1999, AJ, 118, 76

Rosati, P., et al. 2004, AJ, 127, 230

Rosati, P., et al. 2009, A&A, 508, 583

Ruiter, A. J., Belczynski, K., & Fryer, C. 2009, ApJ, 699, 2026

Ruiz-Lapuente, P., Burkert, A., & Canal, R. 1995, ApJ, 447, L69

Ruiz-Lapuente, P. & Canal, R. 1998, ApJ, 497, L57

Ruiz-Lapuente, P., et al. 2004, Nature, 431, 1069

Sahlén, M., et al. 2009, MNRAS, 397, 577

Salpeter, E. E. 1955, ApJ, 121, 161

Sánchez-Blázquez, P., Gorgas, J., Cardiel, N., & González, J. J. 2006, A&A, 457, 809

Sand, D. J., et al. 2011, ApJ, 729, 142

Sand, D. J., Zaritsky, D., Herbert-Fort, S., Sivanandam, S., & Clowe, D. 2008, AJ, 135, 1917

Santos, J. S., et al. 2009, A&A, 501, 49

Sarkar, D., Amblard, A., Cooray, A., & Holz, D. E. 2008, ApJ, 684, L13

Scalzo, R. A., et al. 2010, ApJ, 713, 1073

Scannapieco, C., Tissera, P. B., White, S. D. M., & Springel, V. 2006, MNRAS, 371, 1125

Scannapieco, E. & Bildsten, L. 2005, ApJ, 629, L85

Schawinski, K. 2009, MNRAS, 397, 717

Schechter, P. 1976, ApJ, 203, 297

Sérsic, J. L. 1968, Atlas de galaxias australes, ed. Sérsic, J. L.

Sharon, K., et al. 2010, ApJ, 718, 876

Sharon, K., Gal-Yam, A., Maoz, D., Filippenko, A. V., & Guhathakurta, P. 2007, ApJ, 660, 1165

Sirianni, M., et al. 2005, PASP, 117, 1049

Sivanandam, S., Zabludoff, A. I., Zaritsky, D., Gonzalez, A. H., & Kelson, D. D. 2009, ApJ, 691, 1787

Soker, N., Frankowski, A., & Kashi, A. 2010, New A, 15, 189

Stanford, S. A., et al. 2005, ApJ, 634, L129

Stanford, S. A., Eisenhardt, P. R., & Dickinson, M. 1998, ApJ, 492, 461

Stanford, S. A., Holden, B., Rosati, P., Eisenhardt, P. R., Stern, D., Squires, G., & Spinrad, H. 2002, AJ, 123, 619

Stanford, S. A., et al. 2006, ApJ, 646, L13

Strazzullo, V., et al. 2010, A&A, 524, A17

Strazzullo, V., et al. 2006, A&A, 450, 909

Strolger, L.-G., et al. 2004, ApJ, 613, 200

Sullivan, M., et al. 2006, ApJ, 648, 868

Suzuki, N., et al. 2011, ApJ, submitted

Thielemann, F., Nomoto, K., & Hashimoto, M. 1996, ApJ, 460, 408

Thomas, D., Maraston, C., Bender, R., & Mendes de Oliveira, C. 2005, ApJ, 621, 673

Tornambe, A. 1989, MNRAS, 239, 771

Tornambe, A. & Matteucci, F. 1986, MNRAS, 223, 69

Totani, T., Morokuma, T., Oda, T., Doi, M., & Yasuda, N. 2008, PASJ, 60, 1327

Trenti, M. & Stiavelli, M. 2008, ApJ, 676, 767

Tsujimoto, T., Nomoto, K., Yoshii, Y., Hashimoto, M., Yanagida, S., & Thielemann, F. 1995, MNRAS, 277, 945

Tutukov, A. V. & Yungelson, L. R. 1994, MNRAS, 268, 871

Uomoto, A. & Kirshner, R. P. 1985, A&A, 149, L7

van den Bergh, S. 1990, PASP, 102, 1318

van Dokkum, P. G., Franx, M., Kelson, D. D., & Illingworth, G. D. 2001, ApJ, 553, L39

van Kerkwijk, M. H., Chang, P., & Justham, S. 2010, ApJ, 722, L157

Webbink, R. F. 1984, ApJ, 277, 355

Wheeler, J. C. & Levreault, R. 1985, ApJ, 294, L17

Whelan, J. & Iben, I. J. 1973, ApJ, 186, 1007

Yee, H. K. C., Gladders, M. D., Gilbank, D. G., Majumdar, S., Hoekstra, H., & Ellingson, E. 2007, in Astronomical Society of the Pacific Conference Series, Vol. 379, Cosmic Frontiers, ed. N. Metcalfe & T. Shanks, 103

Yungelson, L. R. 2005, in Astrophysics and Space Science Library, Vol. 332, White dwarfs: cosmological and galactic probes, ed. E. M. Sion, S. Vennes, & H. L. Shipman, 163–173

Yungelson, L. R. & Livio, M. 2000, ApJ, 528, 108

Zibetti, S., White, S. D. M., Schneider, D. P., & Brinkmann, J. 2005, MNRAS, 358, 949